California AHMCT Program
University of California at Davis
California Department of Transportation

MOBILE ROBOTIC SYSTEM FOR HIGHWAY MAINTENANCE AND CONSTRUCTION *

Jae H. Chung
David T. Eveland
John F. Gardner
James M. Stiles
Steven A. Velinsky, Principal Investigator

AHMCT Research Report
UCD-ARR-99-06-30-04

Final Report of Contracts
IA 65X875 T.O. 96-10 & 99-10

June 30, 1999

* This report has been prepared in cooperation with the State of California, Business and Transportation Agency, Department of Transportation and is based on work supported by Contract Numbers IA 65X875 T.O. 96-10 & 99-10 through the Advanced Highway Maintenance and Construction Technology Research Center at the University of California at Davis.

ABSTRACT

This report discusses the detailed mechanical design of an Autonomous Redundant Mobile Manipulator with Advanced Control Scheme (ARMMACS). This autonomous vehicle is a scaled mobile manipulator developed to validate software and conceptual mobile manipulator designs. Furthermore, this report discusses kinematics and dynamic modeling of mobile manipulators as well as coordination control of a human\manipulator system.

First, product design specifications are presented and the overall robot conceptual design is developed. Various design concepts or components are also discussed for each major vehicle subsystem, concluding in the selection of the most promising concepts or components. Then, the detailed design of each subsystem is presented with engineering reasoning. Experimentation used to compare vehicle performance to design specifications and to measure vehicle parameters is presented. Then, the overall design is evaluated and suggestions for improvement are given.

A systematic, unified kinematic analysis of wheeled mobile manipulators is presented. Furthermore, the effect of manipulator placement of the overall manipulability of the system is investigated. Then, the dynamic modeling of mobile manipulators is discussed and the coupling forces between the manipulator and platform are analyzed. Lastly, two new types of coordinated control schemes are presented. These designs are based on the potential for using mobile manipulators to assist in human directed tasks.

EXECUTIVE SUMMARY

A Mobile Manipulator is a robotic manipulator mobilized to function in a large workspace. Often MMs implement conventional robotic manipulator arms that typically mount to a fixed support and perform carefully planned tasks within a limited workspace. Mobilizing the manipulator almost always results in kinematic redundancy increasing the dexterous manipulation of the end effector. This enables the manipulator to perform a broader range of tasks. Consequently, interest in applying mobile manipulators to industrial, space, and public service applications grows annually.

Unfortunately, increasing mobility also substantially increases the system's complexity. First, an entire additional machine, the mobile platform, is added to the robot. Second, coordinating the control of a manipulator and platform is a complex problem. In general, the major control issues involve the coordination strategy of the mobile manipulator as a means of resolving kinematic redundancy, and the dynamic interaction of the mobile platform and the manipulator. Additionally, some common platform propulsion mechanisms (e.g. conventional wheels) constrain the platform non-holonomically, complicating dynamic modeling.

This report discusses the detailed mechanical design of an Autonomous Redundant Mobile Manipulator with Advanced Control Scheme (ARMMACS). This autonomous vehicle is a scaled mobile manipulator developed to validate software and conceptual mobile manipulator designs. Furthermore, this report discusses kinematics and dynamic modeling of mobile manipulators as well as coordination control of a human\manipulator system.

First, product design specifications are presented and the overall robot conceptual design is developed. Various design concepts or components are also discussed for each major vehicle

subsystem, concluding in the selection of the most promising concepts or components. Then, the detailed design of each subsystem is presented with engineering reasoning. Experimentation used to compare vehicle performance to design specifications and to measure vehicle parameters is presented. Then, the overall design is evaluated and suggestions for improvement are given.

A systematic, unified kinematic analysis for manipulator arms mounted to mobile platforms is presented. The differential kinematics for the composite system is used, along with an extended definition of manipulability, to generate a design tool for this class of systems. An example is presented in which a 3 DOF anthropomorphic manipulator is mounted on a platform powered by two independent drive wheels. Scaled manipulability ellipses are used to visualize the effect of manipulator mounting position on the overall mobility of the system. Given information about the intended tasks of the mobile manipulator, conclusions may be drawn as to the most appropriate mounting site. For the tasks which motivated this research, automated highway construction and maintenance, it is concluded that the manipulator base should be near the axles of the drive wheels and far from the centerline of the platform.

The dynamic modeling of a mobile manipulator is discussed. The equations of motion of a mobile manipulator system are developed using a Newton-Euler formulation. This model incorporates a complex tire model which accounts for tire slip and is thus applicable to high speed and high load applications. The model is then systematically exercised to examine the dynamic interaction effects between the mobile platform and the robot manipulator, to illustrate the effects of wheel slip on system performance, and to help understand the efficacy of kinematically coupled models.

A human/manipulator coordination is a new and attractive use of robot manipulators where two coordinated manipulators are necessary but lacking intelligent capability to perform given tasks. Two new types of coordination control schemes called operator manipulator coordination control (OMCC) developed. One is based on impedance control and the other explicit force control. Therefore, implicit in the human assisted scheme is force feedback and control. In these schemes, H-infinity optimal controllers are integrated with classical impedance control or explicit force control to improve and robustify the closed-loop performance that can be degraded due to the disturbances applied by a human operator. Simulation study shows excellent force regulation and tracking performance of the developed controllers.

TABLE OF CONTENTS

LIST OF FIGURES

LIST OF TABLES

DISCLAIMER/DISCLOSURE

"The research reported herein was performed as part of the Advanced Highway Maintenance and Construction Technology Program (AHMCT), within the Department of Mechanical and Aeronautical Engineering at the University of California, Davis and the New Technology and Research Program at the California Department of Transportation. It is evolutionary and voluntary. It is a cooperative venture of local, state and federal governments and universities."

"The contents of this report reflect the views of the author(s) who is (are) responsible for the facts and the accuracy of the data presented herein. The contents do not necessarily reflect the official views or policies of the State of California or the University of California. This report does not constitute a standard, specification, or regulation."

Chapter 1

Introduction

Humans constantly search for ways to simplify their lives and often find them in the form of machines. When introduced to society, most machines seem heavenly, people's minds wander in abyss, dreaming of time saved, relief of their aching bodies, and of previously unthinkable explorations. Unfortunately, this feeling of utopia often ends in a realization of unexpected adverse effects caused by the new machine, commonly environmental pollution. Even with the negative side effects, these machines often truly benefit society; therefore, engineers often find themselves designing new machines to correct problems caused by the dream machine. Thus, the development of machines offering both the characteristics a dream machine and a problem solver receives vast energy from the engineering and scientific community. Mobile Manipulators (MMs) present such potential. Consequently, interest in applying mobile manipulators to industrial, space, and public service applications grows annually. A Mobile Manipulator is a robotic manipulator arm mobilized to function in a large workspace. Often MMs implement conventional robotic manipulator arms that typically mount to a fixed support and perform carefully planned tasks within a limited workspace. Mobilizing the manipulator almost always results in kinematic redundancy increasing the dexterous manipulation of the end effector. This enables the manipulator to perform a broader range of tasks.

Unfortunately, increasing mobility also substantially increases the system's complexity. First, an entire additional machine, the mobile platform, is added to the robot. Second, coordinating the control of a manipulator and platform is a complex problem. In general, the major control issues involve the coordination strategy of the mobile manipulator as a means of

resolving kinematic redundancy, and the dynamic interaction of the mobile platform and the manipulator (Chung and Velinsky, 1996). Additionally, some common platform propulsion mechanisms (eg. conventional wheels) constrain the platform non-holonomically, complicating dynamic modeling.

Due to their mobility and dexterity, if equipped with appropriate sensing and control equipment, MMs are ideal for performing operations in unstructured environments. For this reason, MMs are ideal for highway maintenance and construction tasks. Recognizing their abilities, the Advanced Highway Maintenance and Construction Technology (AHMCT) Research Center is developing a MM for highway operations. Eventually the AHMCT Center intends to design MMs to perform highway maintenance operations within a traffic lane behind a moving support vehicle, maintenance within a closed lane where worker safety is at risk, and to assist human workers. Highway maintenance operations performed behind a moving support vehicle (on the fly) require traffic to be slowed; however, they do not require lane closure, thus reducing traffic congestion and improving worker safety. Additionally, for maintenance within a closed lane, MMs could be deployed to the road while workers operate them from a safer environment, e.g., within the confines of a support vehicle.

1.1 Current Mobile Manipulator Research and Uses

Mobile Manipulators have tremendous potential to relieve humans of time consuming routine tasks, and work in environments harmful to human health. This has spurred interest in MMs and resulted in the conception of several possible applications. Generally, MMs currently in existence or under development fall into two categories, those implementing autonomous automatic control and those controlled by remote human operators (tele-operated). Autonomy is

coined in the literature to describe several aspects of Mobile Robots (mobile platforms without manipulators) and Mobile Manipulators. For instance, autonomy sometimes describes the measure of mechanical or electrical freedom of the robot (e.g., whether it is tethered and whether it houses its own power supply). Other times autonomy describes the ability of the control scheme, sensors, and actuators to evaluate, "reason," and react to the robot's environment based on a simple operator command to perform a certain type of task (e.g., seal all cracks in the workspace or vacuum the room). As used here, the term autonomy characterizes a vehicle with a copious ability to "reason" and react to its environment.

Both autonomous and human controlled Mobile Robots and Mobile Manipulators take many different forms. Various holonomic and non-holonomic platforms exist, commonly propelled by conventional and omnidirectional wheels and by tracks. Although these propulsion methods prevail, many legged platforms also exist. For example, the Humanoid designed by Honda is a two legged man-like MM. (Honda Motor Co. "Humanoid Robot," 1998.) Several multi-legged Mobile Robots (no manipulator) also exist. An example of a multi-legged Mobile Robot is the Multifunctional Automated Crawling System (MACS) designed by Jet Propulsion Laboratory (JPL) under contract with NASA. (Volpe, "Multifunction Automated Crawling Sys," 1998) The MACS, shown in Figure 1.1, utilizes several suction cup feet to scale fuselages of C5 aircraft while onboard sensors and cameras inspect for damage. IS Robotics designed a multi-legged Mobile Robot, Ariel, capable of traversing the ocean floor or land to remove mines or other obstacles. MMs not only use diverse platforms, but they also implement a wide variety of manipulator arms. Many utilize 6 or 7 Degree of Freedom (DOF) articulated manipulators manufactured by companies such as Robotics Research Corporation and Unimation while others use manipulators designed for specific tasks. Sugar and Kumar (1998) give one example of a

task specific manipulator arm. They use a planar 3 DOF parallel manipulator to test a decentralized control scheme for cooperative control of multiple MMs. Specifically, two of their MMs can cooperatively lift a box and move it along a trajectory.

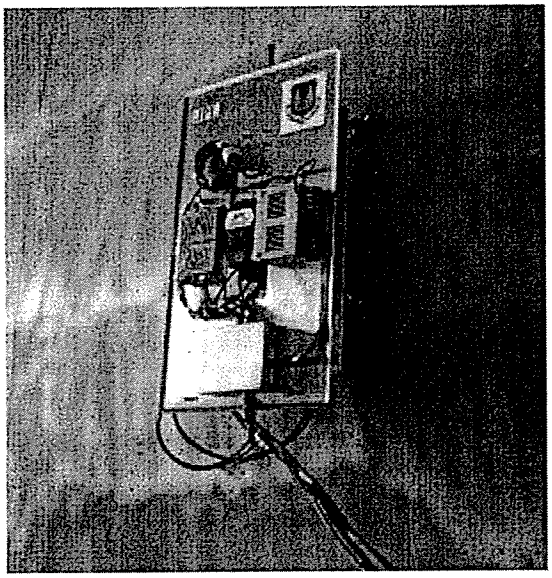

Figure 1.1: MACS Crawling on C5 Fuselage (Volpe, "Mulifunction ," 1998)

Due to phenomenal possible applications and the inherent complexities of their control, developing MMs with autonomous automatic control interests researchers worldwide. These robots require advanced sensing, control, and actuation technologies. Thus, vast literature exists regarding the development of these technologies for various MM applications. Most of the literature discusses control system design. Other common and sometimes related topics are the dynamic interaction of the platform and manipulator, and the interaction of the mobile manipulator with its environment including its collaboration with human workers. Yamamoto and Yun (1996) studied the dynamic interaction of a non-holonomic mobile platform and a manipulator on the tracking performance of the manipulator end effector. On the other hand, the mechanical design is rarely discussed in the literature except geometric considerations for specific environments. Quiang et al. (1998) consider the size requirements of a MM working in

offices and houses and consider stabilization in the control. This is because most of the literature discusses automatically controlled MMs fabricated to prove technologies, analytical simulations, or the usefulness of MMs to specific applications. In this situation, detailed mechanical design is not important.

To date MMs guided by autonomous automatic control operate successfully only in structured laboratory environments performing well-planned tasks. As an example, the semi-autonomous ROMAN (Hanebeck et al., 1997) performs typical household or office service tasks such as surface cleaning or fetching in environments prepared w/ reflective tape and a priori recognized objects. Construction is another industry finding potential applications for these robots. Pritschow et al. (1995) discussed the development of a MM for Automated Construction of Masonry on the Construction Site. This robot is semi-autonomous in that the brick laying operations are automated once the workspace is defined, but a human operator controls the global motions.

Researchers study a plethora of specific areas within the Mobile Manipulator and Mobile Robot realm. Much of the research focuses on control scheme development. Hatano et al. (1996) present the construction and simulation of an adaptive controller designed to improve the performance of a MM operating on unknown irregular terrain. A more specific part of control often discussed in the literature is resolution of the kinematic redundancy formed by combining the DOF of a manipulator arm redundancy with those of a mobile platform. One such paper by Pin et al. (1996) explains a method of resolving this redundancy using Full Space Parameterization (FSP), which utilizes constraints that may vary in time and in number during a trajectory. The paper gives examples for MMs with up to 11 DOF. Also, Lim and Homayoun (1997) present a control system for real-time resolution of kinematic redundancy using a

configuration-control technique. This technique performs two additional tasks to resolve the system.

Additional references to other literature discussing control system design are made elsewhere in this chapter and abundant material is available. Other control methods often encountered are robust and force control. Coordinating the work efforts of multiple MMs to perform a single task receives a lot of attention as well (Sugar and Kumar, 1998). For many control schemes, the location of the MM in its workspace must be precisely known. Precisely measuring a MMs position within a large workspace proves very difficult, so several researchers concentrate on applying various available sensors to this task.

Asakura et al. (1998) propose a position/orientation measurement method using a Hand-eye camera and 3-D landmark. Holenstein and Badreddin (1994) suggest updating erroneous odometric information with ultrasonic range measurements using an Extended Kalman Filter algorithm.

Researchers are increasingly concerning themselves with the interaction of Mobile Robots and their environments. This involves both safely operating in conjunction with humans and ensuring the usefulness of the robot as part of the workspace ecology. Arkin et al. (1997) present neurophysiological and ethological modeling methods for understanding and dynamically modeling the relationship between a robot and its environment. This approach ensures that robots are competitive with other agents that performing the same tasks before they displace those agents.

MMs controlled by remote human operators already find applications in less structured industrial environments. Hazardous materials teams and environmental disasters have expedited the development of these MMs for jobs such as nuclear facility work and explosive ordinance

disposal. Many scientific research institutes such as Oak Ridge National Laboratory, as well as many universities and businesses have developed this type of MM to work in areas that are hazardous or detrimental to human health. By utilizing the stupendous sensory, computational, and reasoning capabilities of humans, control schemes for these robots remain simple relative to more autonomous vehicles. However, the perception, computation, and reaction speed of the operator also limit the real-time operating speed of these robots. Although simpler, the control schemes for these robots often contain several closed feedback control loops to decompose commanded end effector motion into movement of the many manipulator joints and the mobile platform. Several of these robots exist. One example is the HAZBOT III (Figure 1.2) developed by California Institute of Technology and Jet Propulsion Laboratory (JPL) under contract with NASA. This robot utilizes a rebuilt ANDROS Mark V Mobile Robot manufactured by REMOTEC along with a custom built manipulator. Using the HAZBOT III, workers deploy a wide variety of tools and sensors into hazardous areas to perform preliminary clean up operations and determine the status of the hazard. This way, a well-planned and safe human intervention takes place.

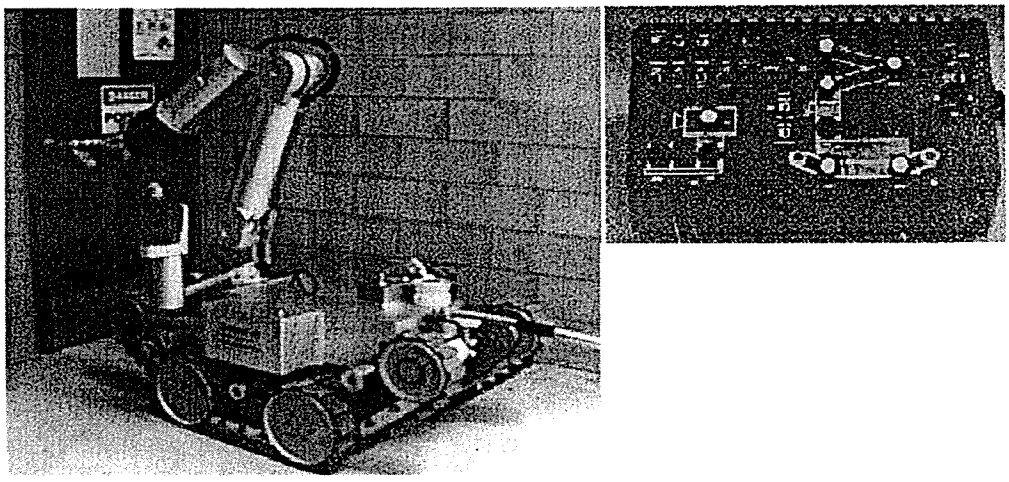

Figure 1.2: The HAZBOT III and its Control Pendant (Volpe, "Ground," 1998)

Redzone Robotics, Inc. manufactures several Mobile Manipulators for nuclear applications. These robots perform waste retrieval and handling, decontamination, decommissioning, inspection, and characterization operations at several nuclear sites worldwide. Rosie and Houdini (Figure 1.3) are examples of Redzone's tethered Mobile Manipulators. Both utilize hydraulic actuation and employ several tools such as buckets, booms, cameras, saws, torches, and vacuums. Conventional wheels propel Rosie while tracks propel Houdini.

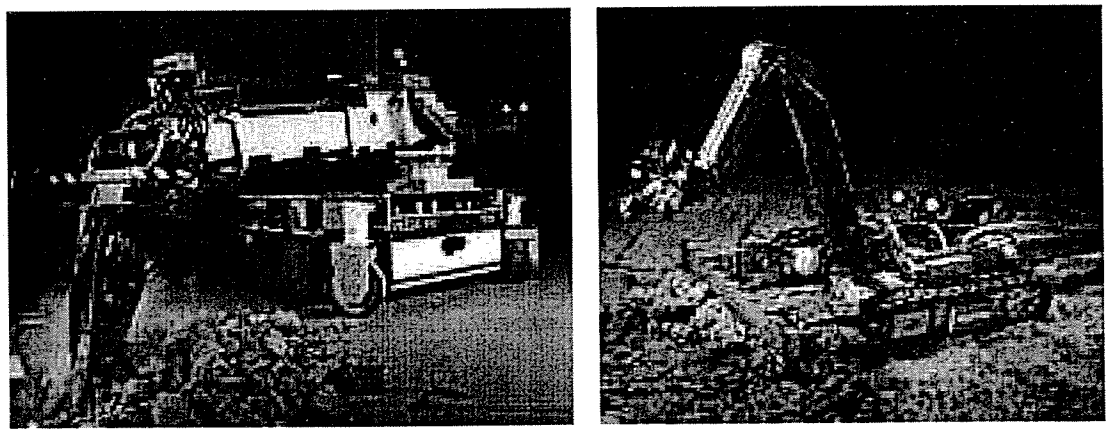

Figure 1.3: Robots for Nuclear Environments - Rosie and Houdini (Redzone, "Nuclear Product," 1998)

Remotely controlled Mobile Robots are also being used to explore regions of space currently inaccessible to humans. JPL and NASA have developed several Mobile Robots for this purpose, the most famous is Sojourner, shown in Figure 1.4, which debuted with the Mars Pathfinder mission. Many of these Mobile Robots either do not have manipulators or have simple, task specific manipulators.

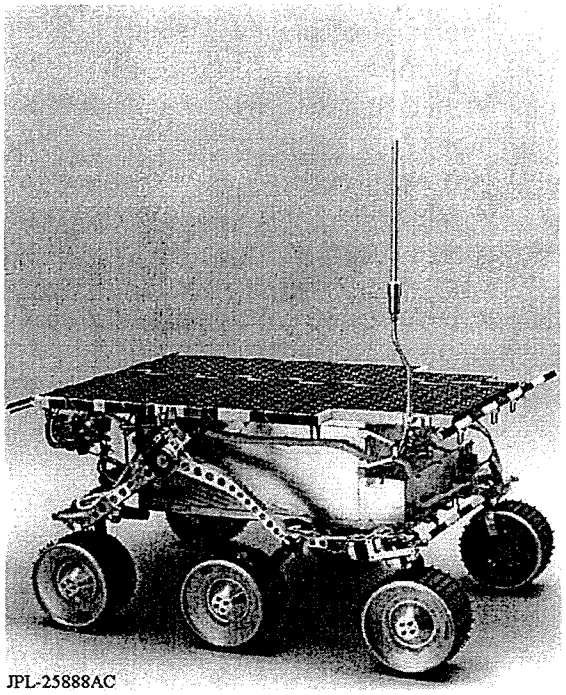

Figure 1.4: Sojourner, the Star of the Mars Pathfinder Mission (Sojourner, 1996)

A twist on remotely controlled Mobile Manipulators are robots that assist or supplement human efforts, ie., they lend a helping hand. This is one of the capabilities of the Stanford Assistant Mobile Manipulators (SAMMs) shown in Figure 1.5. Much research has been done on mechanical systems with human-robot interaction, such as Hardyman, a master-slave manipulator system, a robot for man-robot cooperation, an Extender, etc. Hirzinger and Landzettel (1985) proposed a direct teaching method of a manipulator using a force sensor mounted on a robot. Fukuda et al. (1990) have proposed a manipulator, which is designed for handling heavy objects in cooperation with a human operator (Fukuda, et al., 1990; Fukuda and Fujisawa, 1991). Kazerooni (1990) has proposed the extender or the manipulator system to extend the strength of the human arm; he has designed a control algorithm, so that the force augmentation ratio could be specified, based on the modeling of the system including the human

operator and the environment. Yamamoto, Eda and Xiaopong, (1996) also discuss coordinating human and MM efforts to complete a task based on the human's initiative.

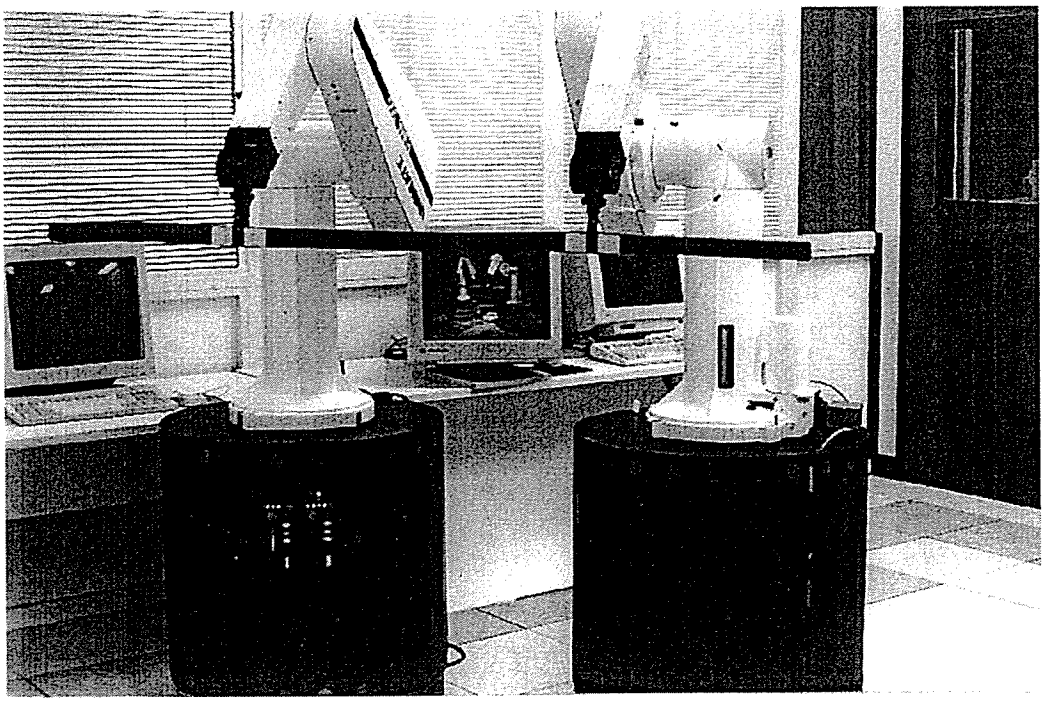

Figure 1.5:Stanford Assistant Mobile Manipulators (Khatib, 1995)

Although the Real-World applications of these two types of MM, are at different stages, much of the research discussed here applies to both types. For example, although the information may be utilized very differently, the research studying the dynamic interaction of the mobile platform and the manipulator, the position and orientation sensing, and the interaction between the MM and its environment are important for both types. The mechanical design of the manipulator described in this report is straightforward, and does not implement revolutionary technology. Therefore, the intent of this section is purely to give the readers insight into the potential applications of MMs and awaken them to the emphasis being placed on the

development of these machines. Though thorough, this section is only a synopsis of MM research and applications.

1.2 Mobile Robots Designed by AHMCT

Formerly, the AHMCT Center developed four Tethered Mobile Robots (TMRs). TMRs are autonomous motorized platforms with tooling attached directly to them. These TMRs are used for concept realization, to develop control algorithms for multiple coordinated TMRs, for routing and crack sealing operations, and to test sensor technologies.

AHMCT engineers performed extensive literature searches and studied several drive wheel configurations during TMR development. Only wheels were considered for propulsion because they propel more efficiently than legged or treaded methods on fairly smooth and hard surfaces (Winters and Velinsky, 1992). Additionally, several options for measuring platform position and heading were explored during TMR development. A robust method of accurately measuring platform position and heading is essential for accurately traversing the workspace.

Several useful concepts and technologies were developed during TMR design. Since the MM platform is serving a purpose similar to the TMR, to mobilize tooling on a nearly 2D (i.e., flat) workspace, it utilizes concepts and technologies developed for the TMRs.

1.3 Problem Description and Objective

Previously, AHMCT research engineers modeled mobile manipulator dynamics and developed several control algorithms for them. Efforts have continued to further advance these dynamic models and control schemes. However, several of the control algorithms have been tested using dynamic computer simulation and now must be validation tested with a physical

system. This report discusses the detailed mechanical design of an Autonomous Redundant Mobile Manipulator with Advanced Control Scheme (ARMMACS). This autonomous vehicle is a scaled mobile manipulator developed to validate software and conceptual mobile manipulator designs. Furthermore, this report discusses the modeling of mobile manipulators as well as presenting two designs for mobile manipulator force-based control.

The ARMMACS utilizes a differentially steered, wheeled platform, and is tethered for electrical power and communications. An Integrated Motions Inc. (IMI) Zebra ZERO manipulator was selected for the ARMMACS. The AHMCT Center designed and fabricated the platform to mobilize this manipulator. Once control schemes are validated and the intricacies of mobile manipulator dynamics and control are well understood, larger mobile manipulators will be built to perform highway maintenance tasks.

This chapter gave an introduction to Mobile Manipulators, a synopsis of Mobile Manipulator research, and a statement of the ARMMACS project objective. Chapter 2 presents product design specifications and develops the overall robot conceptual design. In Chapter 3, various design concepts or components are discussed for each major vehicle subsystem, concluding in the selection of the most promising concepts or components. Chapter 4 presents the detailed design of each subsystem with engineering reasoning. Chapter 5 presents experimentation used to compare vehicle performance to design specifications and to measure vehicle parameters. The overall design is evaluated in Chapter 6 and suggestions for improvement are given.

The second section discussed modeling and control and begins with Chapter 7. In chapter 7, a systematic, unified kinematic analysis of wheeled mobile manipulators is presented. Furthermore, the chapter investigates the effect of manipulator placement of the overall

manipulability of the system. Chapter 8 discusses the dynamic modeling of mobile manipulators and analyzes the coupling forces between the manipulator and platform. In Chapter, 9 two new types of coordinated control schemes are presented. These designs are based on the potential for using mobile manipulators to assist in human directed tasks.

Several appendices contain detailed calculations, detailed prints and assembly drawings and Zebra ZERO specifications.

Chapter 2

Robot Conceptual Design

2.1 Introduction

Early in the design process the customer and the customer's needs must be identified. Customers may be consumers or coworkers, but a product is successful only if their needs are met. Customers needs must be transformed into explicit target specifications for the product and, where applicable, these should be quantifiable. With these product specifications in mind, the design team can then generate concepts for the overall product and each product subsystem. Significant concepts are then rated against selection criteria derived from overall product specifications. Selection criteria may be weighted to emphasize their importance. Once rated against each criterion, ranking the concepts reveals the most promising concept. The rating and ranking process may unveil small shortcomings in certain concepts that can be easily changed to better the concept; therefore, this process of concept selection may be iterative.

This chapter presents the overall conceptual design of the ARMMACS. Considering user needs, the project budget, available components, and time constraints, the design team determined Product Design Specifications (PDS) for the platform. This set of technical metrics ensures that the product will satisfy the user's needs. Using these specifications as guidelines, the general platform geometry and the platform drive wheel configuration are determined. Next, manipulator requirements are discussed and a manipulator is selected. Mounting locations for the manipulator are selected for the manipulator based on information presented in Gardner and Velinsky (1999). Last a method for measuring the position and orientation of the platform is chosen.

2.2 Product Design Specifications

2.2.1 Kinematic and Dynamic Requirements

For usefulness as a test platform for an on-the-fly highway maintenance mobile manipulator, the platform must move at speeds representative of those necessary for highway maintenance. This led to the following requirements: the platform must accelerate at 3.26 m/sec^2 (10.7 ft/sec^2) minimum with a maximum speed of 2.29 m/sec (7.5 ft/sec).

Additionally, for sufficient path following capability, platform kinematics must provide a minimum of two DOF in the horizontal plane. Also, the platform should be allowed constrained roll and heave, 1.27 cm – 2.54 cm (½ in - 1 in) compliance at each wheel and caster should allow sufficient roll.

2.2.2 Weight Requirements

In order to study the dynamic interaction between the manipulator and the platform, the base weight of the platform, without load or ballast, should not exceed 10 times the manipulator weight. Ideally, the ratio of platform weight to manipulator weight would be less. However, the manipulator is lightweight and many of the available electrical components, which are to be platform based, are not; therefore, a lower ratio is unreasonable. Ballast capability should be provided to ensure stability of the platform in modified test configurations and to vary dynamic performance. Enough Ballast should be provided to achieve a total platform weight of 227 kg (500 lb).

2.2.3 Tire Specifications

To isolate the errors introduced in control accuracy due to tire slip, two sets of tires with greatly different compliance must be used. One set must have minimal compliance and the other must have liberal and adjustable compliance. These sets should be easily interchangeable and should have similar diameters and widths.

2.2.4 Motors and Drives

Electro-Craft F4050 brushless servo motors, DDM-030 servo drives, and Bayside RA 115 precision gearheads are available and should be used to propel the platform if power specifications meet vehicle requirements.

2.2.5 Drive Train Specifications

Servomotors are sensitive to backlash (temporary uncoupling) between the applied loads and the servo. Backlash can result in poor servo performance or instability since the servo must be tuned for both the loaded and unloaded cases. Therefore, backlash between the motor and the tire should be limited to the backlash within the gearhead, and the selected gearhead must have minimal backlash. Additionally, servomotors are sensitive to compliance within the mechanism transmitting motor torque to the load. Compliance effects can result in a torsional resonance, which causes instability and leads to servo degradation. ORMEC, a manufacturer of servos, claims that this resonance usually occurs between 100 and 500 Hz; therefore, the natural frequency of the coupling mechanism should be 500 Hz minimum. Furthermore, the Drive Train must easily accommodate both sets of tires. Bayside RA-115 precision 20:1 reduction planetary

gearheads are available and should be utilized if this reduction is sufficient to meet other requirements.

2.2.6 Electronics

Zebra ZERO manipulator encoder signals are single ended signals sensitive to electromagnetic noise. Additionally, the Zebra encoder cables are not shielded. Magnetic fields can be contained only within a ferrous enclosure. Since the flow of current produces a magnetic field, the power electronics must be shielded in a steel enclosure. Power electronic circuitry will include a SQUARE D DPA63 Definite Purpose Contactor, two Roxburgh MDF36 AC Line Filters, two Omron 67J-3A1B-B-W1 relays, two Dayton 5X842F General Purpose Relays and their bases, a minimum of 12 BUSS R25030-1SR fuse holders and two BUSS R25060-1SR fuse holders, and wiring.

Single phase 208 volt power will be tethered to the platform and connected via a Hubell Twist-Lock receptacle. A remote control Pendant will be tethered to the platform and connected through a 16 pin Amphenol 24 5S connector. Remote keyboard and monitor signals will be amplified by a CYBEX™ PC EXTENDER PLUS. An additional shielded cable connected to the platform using a 15 pin DIN connector will be tethered for computer communication. Also, an Industrial Computer Source® 9300-10 chassis, a Zebra Power supply, and a PC EXTENDER Transmitter must be attached to the Chassis.

2.2.7 Manipulator Mounting

The manipulator should be mounted to the platform in a location that maximizes its workspace at ground level. Additionally, guidelines for the geometric design of differentially

steered mobile manipulators set in Garner and Velinsky, 1999 should be followed to maximize the mobile manipulator performance. Also, vibration at the base of the robot would result in accelerations of the end effector causing force readings at the six-axis force sensor. To prevent vibratory excitation during normal operation, the Zebra mounting surface must be stiff and have a high natural frequency.

2.2.8 Operating Environment

The ARMMACS prototype is intended to be used in the laboratory only, and thus, the operating environment for the ARMMACS will include any of the AHMCT indoor laboratory facilities. The flooring in these facilities is nearly flat and either concrete or linoleum.

2.2.9 Manufacturing Processes

Since the vehicle is a software validation test bed and only one will be built, processes should include only those not requiring high cost or unique tooling. Therefore, the manufacturing processes should be limited to welding, forming, machining, and common plating and painting.

2.2.10 Materials

Only stock materials and shapes should be used in the platform's design.

2.2.11 Users

Only AHMCT Center engineers will operate the ARMMACS.

2.3 Overall Conceptual Design

Mobile Manipulators generally are a fusion of two major subsystems, a mobile platform and a robotic manipulator. Both of these subsystems can take on several forms. For example, the platform could be configured many different ways resulting in vastly different footprints. Likewise, one of several known propulsion methods may be utilized, or a unique method may be developed specifically for the platform. Additionally, depending on the task to be performed, the manipulator could be a simple linkage with few DOF or a complex arm with several DOF. Also, the end-effector may be a job specific tool, a general one DOF gripper, or a complex gripper with several DOF. Conceptual design for these major subsystems is developed in this section.

2.3.1 Platform Layout

The work environment of a MM plays a large role in determining its general geometric layout. The primary tasks and the development cycle time of a MM also contribute to the general layout. If the mobile manipulator must traverse a crowded or cluttered workspace or through a living space, the overall footprint must be small and components must be selected and organized compactly. On the other hand if the workspace is clear of obstructions, component selection and compact organization are not as critical. Additionally, if the manipulator's tasks are general, modifications to the hardware and electronics in preparation for specific tasks are probable, and a well-organized and spacious organization will favor quicker modifications. A short development cycle requiring concurrent engineering also favors a more spacious organization with minimal component interfaces. This type of layout allows room for changes and unexpected components. Furthermore, a MM designed to perform tasks high above its traveling surface would likely have

a tall platform, with a manipulator mounted near its top. Conversely, a MM designed to perform tasks at the ground level will most likely have a manipulator mounted near the ground.

The ARMMACS was developed primarily to verify software that was written to control a MM performing tasks at ground level; therefore, the manipulator will be mounted near the ground. Also, the ARMMACS was designed and fabricated on a short timeline, which required concurrent mechanical hardware and electrical system design. This along with general task specifications and a clear workspace favors a well-organized and spacious component layout. Accordingly, the ARMMACS will be configured low to the ground and all electrical and mechanical components will be readily accessible and easy to change.

2.3.2 Platform Propulsion Concept Selection

As with the TMRs, the ARMMACS is a ground vehicle that will operate on fairly smooth and hard surfaces where wheels propel more efficiently than treaded or legged methods (Winters and Velinsky, 1992). Various wheel types and configurations would adequately propel the ARMMACS platform and several were explored. The main purpose of the platform is to mobilize the manipulator (a tool) in a two dimensional workplace, a task vary similar to the TMR tasks. While the ARMMACS is a test bed that will be used in indoor labs only, its configuration should be transferable to a highway maintenance robot. With the previous statements in mind, it makes sense to refer to TMR wheel configuration concept selection in determining the wheel configuration for the ARMMACS platform.

Several drive wheel configurations were studied during TMR development. Configurations that were studied implemented either conventional, omnidirectional, or ball wheels. Conventional wheel configurations included steered wheel configurations and a

configuration steered by differential wheel speed, both of which have 2 DOF and singularities in the workspace. Steered wheel configurations cannot follow all planar paths due to turn radius constraints; whereas, the configuration steered by differential wheel speed can follow any planar path. Singularities in the workspace occur because the drive wheels are constrained to travel in a path normal to their axis. Symmetrical omnidirectional drive wheel configurations and ball wheel configurations exhibit 3 DOF; consequently, they experience no singularities in the workspace. Ball wheel concepts were quickly precluded because they require complex mechanical support and actuation mechanisms that are not practical for the budgets and short timelines of the TMR projects. For the same reasons, they will also not be considered for the ARMMACS platform.

Omnidirectional and conventional wheels require relatively simple actuation; therefore, AHMCT engineers extensively studied concepts that implement them. Omnidirectional wheels are more difficult to manufacture than conventional wheels because they consist of a wheel with rollers on its circumference. The operating principle of this type of omnidirectional wheel requires that each roller on every wheel must have similar hub friction, and must have similar ground interface properties. For these reasons, kinematics and dynamics of an omnidirectional wheel driven platform may be more sensitive to uneven and irregular road surfaces, and to workspace contamination. This research determined a differentially steered, conventional wheeled platform as shown in Figure 2.1 to be the most robust and cost effective configuration for a highway maintenance TMR (Winters and Velinsky, 1992). Therefore, the ARMMACS platform inherited a differentially steered, conventional wheel configuration concept from the TMR development.

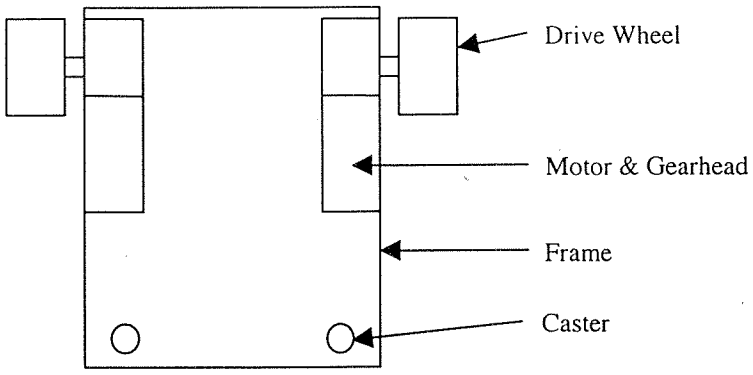

Figure 2.1: Differentially Steered, Conventional Wheeled

2.3.3 Manipulator Selection

Much of the preliminary dynamics and control work was performed anticipating the use of a vertically articulated six DOF manipulator. Thus, to achieve desired kinematic redundancy and test the control algorithms, a manipulator of this form must be used. Since several six DOF manipulators are commercially available and development costs and time would exceed those available, a commercially available manipulator will be used. Coordination of the platform and manipulator motion will require modification of the manipulator controller source code; therefore, the selected manipulator must have open software and hardware architecture. Also, the manipulator cost must meet budget requirements.

Manipulators manufactured by Robotics Research Corporation, CRS Robotics Corporation, and Unimation were considered. These manipulators utilize embedded software and proprietary control code making them difficult to incorporate with the platform control. Detailed controller specifications and code for some of these robots are available with special orders; however, the cost of a special order far exceeded funds available for the manipulator. For these reasons, none of these manipulators were suitable.

An Integrated Motions Inc. (IMI) Zebra ZERO vertical articulating manipulator, as shown in Figure 2.2, was slated for the ARMMACS. Figure 2.3 shows the kinematic configuration of the Zebra ZERO. This seven DOF manipulator provides the desired kinematic redundancy. Equally important, the Zebra has open software and hardware architecture. The Zebra uses a commercially available Hewlett-Packard (HP) HCTL 1 controller for which detailed documentation is readily available. Furthermore, access to IMI control source code simplifies modifications to the controller that are essential for real-time, coordinated platform and manipulator control. The HP HCTL 1 control board installs in and communicates directly with an IBM PC. A PC based manipulator controller is ideal for this research robot because controllers for both the manipulator and platform can be installed in the same computer. As a result, a single program written in any code capable of real-time operation can communicate with both the platform and manipulator controllers. This is essential because for coordinated platform and manipulator control, both controllers must communicate with a single control algorithm. Furthermore, with a PC based system, control algorithms can be revised quickly and several algorithms can be stored in the computer simultaneously. Another advantage of the Zebra is a six axis force sensor that feeds back a 6X1 vector of forces and moments acting on the end effector. This vector can be utilized to resolve position error and expands control capability. In addition to meeting all technical specifications, the Zebra also met budget requirements.

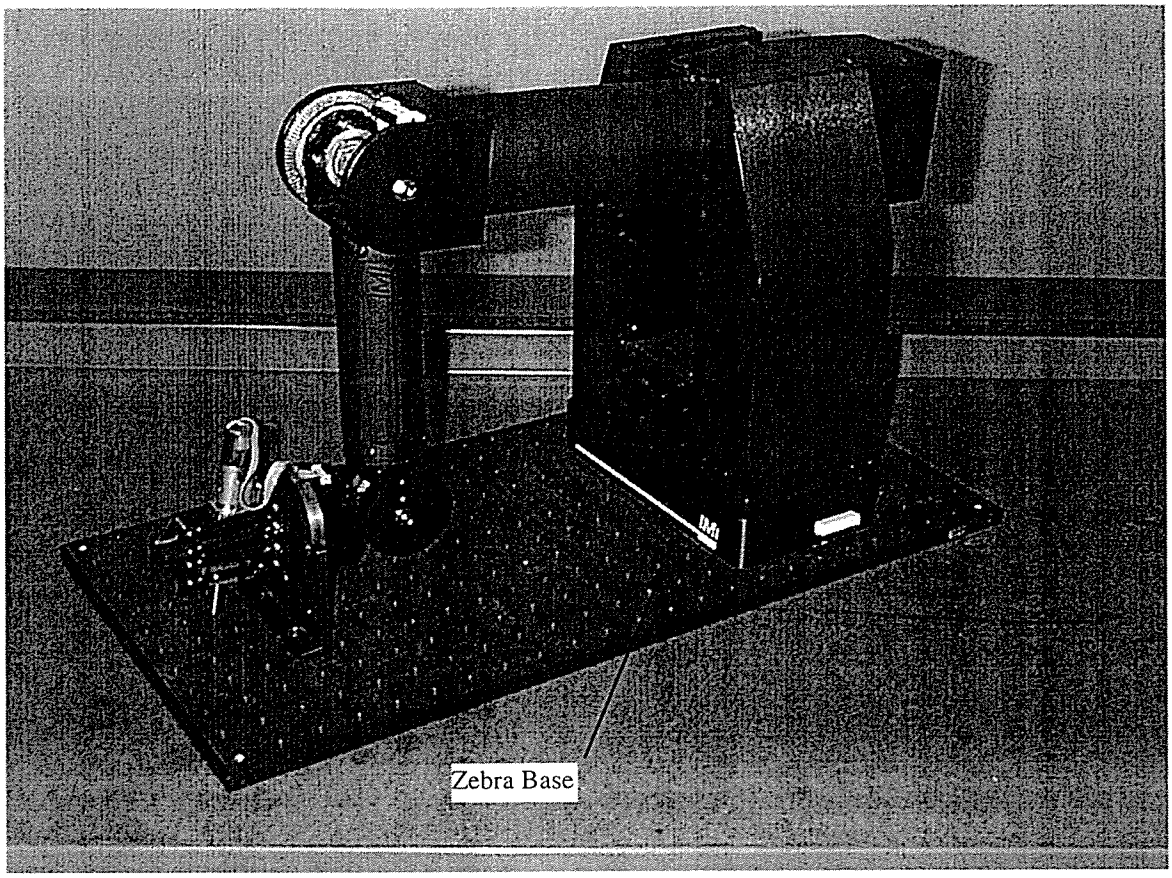

Figure 2.2: Zebra ZERO Manipulator

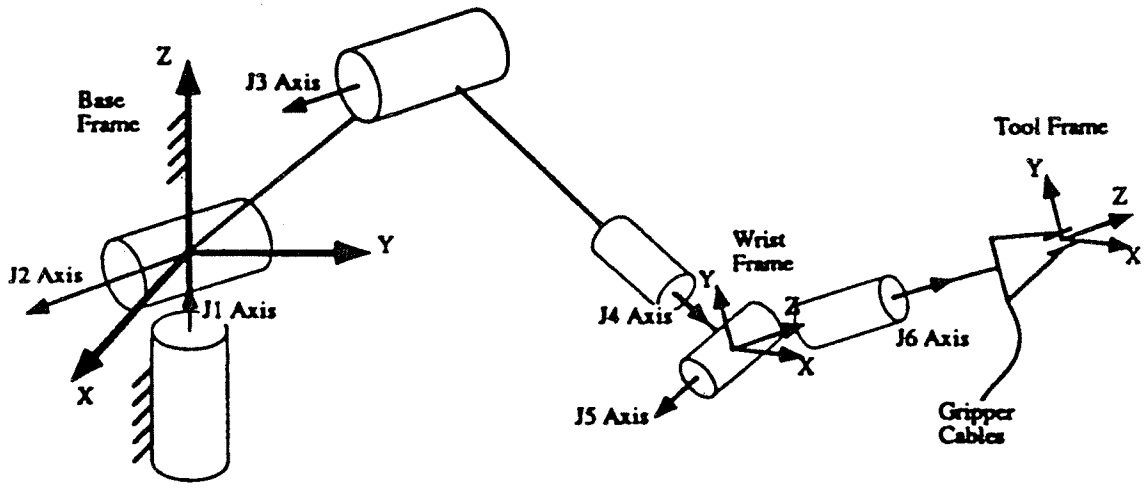

Figure 2.3: Zebra ZERO Kinematic Configuration

2.3.4 Selection of Manipulator Mounting Location and Method

The primary purpose of the ARMMACS is to test control algorithms and mobile manipulator configurations to determine the feasibility of a larger robot tooled to perform highway maintenance behind a moving support vehicle (on the fly). In on the fly highway maintenance, the mobile manipulator will be tethered to a support vehicle that will move down the lane with a nearly constant velocity. Simultaneously, the mobile manipulator will maneuver such that the end-effector contacts a single point on the road surface for a sufficient length of time to perform a task. The placement of the manipulator on the platform plays a key role in determining the maximum speed and/or maximum contact time of the end effector.

In Gardener and Velinsky (1999), traditional measures of manipulability for fixed based manipulators have been extended to differentially steered mobile manipulators to determine the best location for the manipulator relative to the platform drive wheels. The kinematics of the platform and manipulator were combined and a general Jacobian matrix was derived that accounted for maximum actuator velocities and related the velocity of the wrist frame to the joint velocities. This Jacobian was then reduced to a two-dimensional case under the assumption that the end effector will stay near the road surface (constant vertical position) while the mobile manipulator maneuvers. With this assumption, vertical motion can be dealt with separate from motion in the horizontal plane. Singular values of this Jacobian were used as the manipulability indices to study the effects of manipulator placement on the end-effector velocities. These indices allow computation and visualization of the end-effector velocity resulting from joint velocities. When working behind a moving vehicle the main concern is the ability of the end-

effector to exhibit large velocities in the direction parallel to the lane (x-direction) which coincides with high contact time capability.

Several manipulator-mounting locations were simulated, and the end-effector velocity capabilities were plotted throughout the workspace to visualize mobile manipulator performance. Figure 2.4 and Figure 2.5 are plots containing several sets of axes. These are the major axes of manipulability ellipses for several end-effector locations in the workspace. The length of each axis represents the magnitude of the end-effector velocity in the direction of that axis. The forward direction of the platform (ie. the global x-direction) is oriented vertically in the plot; therefore, for on the fly operations, it is desirable that all vertically oriented axes be as long as possible. Figure 2.4 simulates a configuration where the manipulator is forward facing with its J1 axis (represented by {B}) at the platform midline and aligned with the axis of the drive wheels (represented by (0,0) coordinate). Figure 2.5 is plotted for a configuration where again J1 is aligned with the axis of the drive wheels, but the manipulator is side-facing and located directly above a drive wheel.

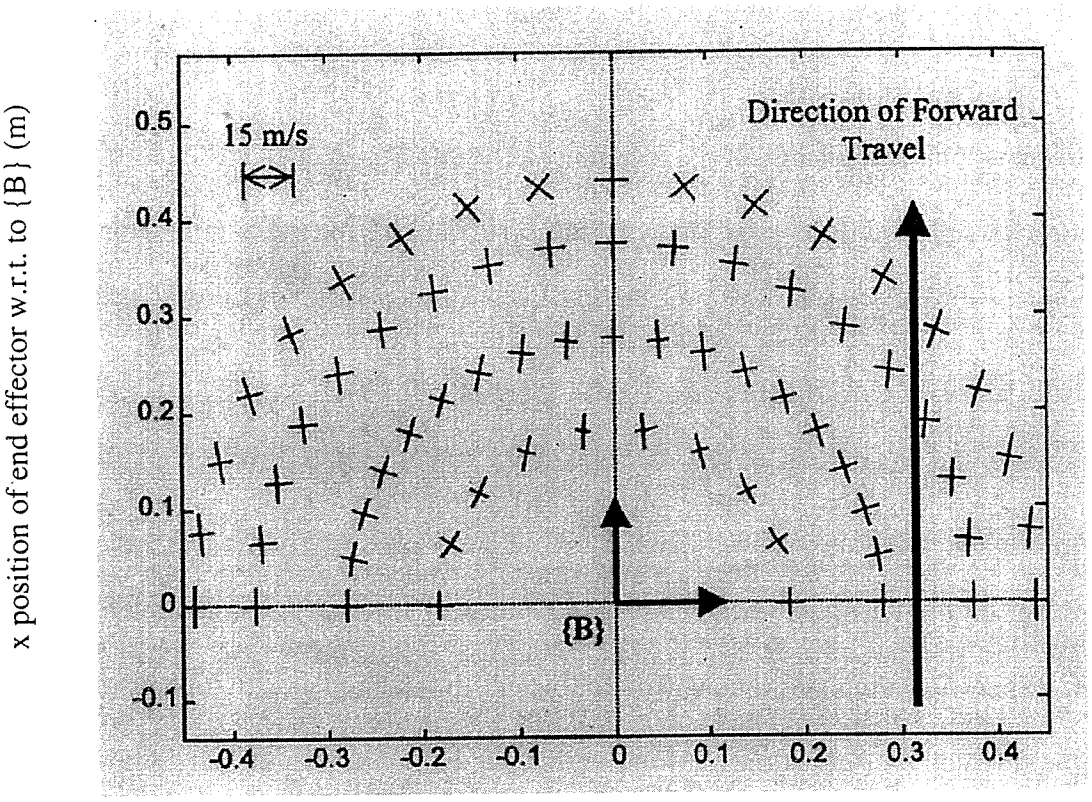

Figure 2.4: Manipulability Plot with a Forward-Facing Manipulator (Adapted from Gardner and Velinsky, 1999)

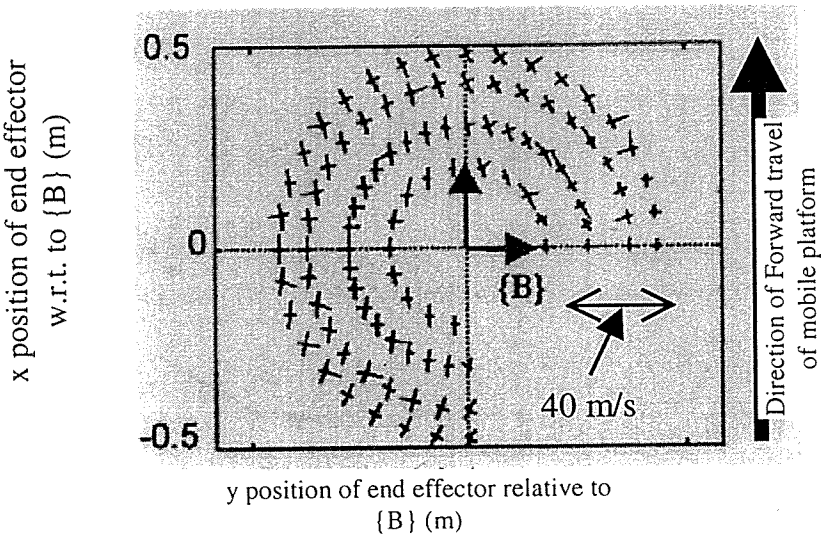

Figure 2.5: Manipulability Plot with a Side-Facing the Manipulator (Adapted from Gardner and Velinsky, 1999)

Examination of these two figures clearly shows that generally the manipulator is capable of higher global x-direction velocity when the manipulator is mounted above the tire than when it is mounted at the platform centerline. Additional simulations were performed with the manipulator located fore and aft each of these positions, and similar manipulability plots were produced for each mounting location.

From these simulations the report concludes that the superlative location for mounting the manipulator when performing on the fly maintenance operations is outboard a drive wheel with the J1 axis aligned with the drive wheel axis. Accordingly, the platform will be designed such that the manipulator can be mounted outboard of at least one drive wheel in this configuration. For versatility and comparison to simulation results, the platform design must also allow the manipulator to be located at the platform centerline aligned with the axis of the drive wheels in the forward-facing configuration.

The Zebra-ZERO must be mounted and operated in the upright position. This configuration inherently reduces the workspace at ground level because the manipulator reaches down to the work surface. To maximize the workspace at ground level the manipulator base will be mounted as low to the ground as practical, ensuring sufficient ground clearance so that small obstacles and workspace irregularities are not problematic.

Furthermore, reprogramming the manipulator's homing nest location with respect to the base is time consuming and laborious. Since testing will require the manipulator to be moved between the two mounting locations, the final design should enable the manipulator to be moved without revising the homing program. A few conceptual designs were considered to simplify moving the manipulator from one mounting location to another.

One option that would enable the manipulator to be portable between two locations using a single homing routine would be to attach two nests to the platform in identical locations relative to the manipulator base for each of its locations. Another option would be to mount one nest to the platform in a suitable location for nesting from both mounting locations. Either one or two nesting programs could be used depending on exact locations relative to the manipulator base. The final method considered involves mounting both the manipulator base and the nest to a single portable unit. The manipulator, the nest, and this portable unit would be moved from one location to another as an assembly; therefore, the location of the nest relative to the base would never change.

Repeatable homing of the manipulator requires that the nest location be precisely known. Because the manipulator is located only by its mounting bolts, the exact mounting is not repeatable. Therefore, fine-tuning would be necessary each time the manipulator were moved with respect to the nest. Fine tuning the homing program is time consuming since it requires using the wrist force sensor in an iterative process. With the first two options, the manipulator base would be moved relative to the nest when the testing configuration is changed which requires the homing program to be fine-tuned; therefore, they were ruled out. As a result, the selected concept utilizes a single portable mount for both the manipulator base and the homing nest.

2.4 Selection of Position and Heading Sensor

Both for software validation and later for highway maintenance work, a path or point in the workspace will be determined (via sensors or cameras) as the place where work is to be performed. The position and orientation of the platform and end-effector in the workspace must

be accurately measured and controlled to place the end-effector at the desired location. The position of the end-effector relative to the platform can be determined from its joint encoders; however, the position of the platform must be measured. During development of the Tethered Mobile Routing Robot (TMRR), the latest TMR, several devices and methods for measuring position and heading were researched. These methods included dead-reckoning methods, sonar navigation, laser rangefinder methods, global positioning systems, a passive mechanical linkage, and a method using Cable Extension Transducers (CETs). Reason and experimentation determined a triangulation method using Cable Extension Transducers (CETs) fit the scope of the project and provided accurate results (Mueller, Hong, and Velinsky, 1997). Measuring position and heading with CETs has been proven on the TMRR. Although problems have occurred, with mechanical refinements, the system will work well in the laboratory environment; therefore, the ARMMACS will also utilize the CET triangulation position and heading measurement method.

2.5 Summary

In this chapter, robot performance requirements were specified in the form of Product Design Specifications. Based on these specifications, the configuration of the overall robot system was determined. Referring to research performed during TMR development, conventional wheels were selected to propel the platform, using differential wheel speeds to steer. An IMI Zebra-ZERO manipulator was chosen, and forward and side facing mounting locations were defined. Last, a triangulation method for measuring position and orientation that was developed for a TMR was chosen for the ARMMACS.

Chapter 3

Platform Design Concepts

3.1 Introduction

The overall conceptual design and general layout of the system were discussed in the previous chapter. During conceptual design, two major subsystems were defined, these were the mobile platform and the manipulator. The conceptual design process concluded that a commercially available IMI Zebra ZERO manipulator would be used. From this chapter forward, this report focuses on the development of the mobile platform. The platform has two major subsystems, the Chassis and the Drive Train. This chapter will build on the overall conceptual design and develop concepts for each of these subsystems, evaluate them, and select the most promising concepts. Taking into account the overall conceptual design and the Product Design Specifications (PDS), reasonable concepts were generated for the Chassis and Drive Train subsystems. Using engineering judgement, each concept was then rated against subsets or derivative sets of the PDS. Ratings for each concept were summed and the totals were used to rank the concepts.

3.2 Chassis Concept Selection

Included in the ARMMACS Chassis are the Frame, Electrical Box, Cable Tower/Sensor Mount, and mounts for the Zebra power supply, the casters, and the Industrial Computer. Many product design specifications drove the Chassis layout. The main component of the Chassis is the Frame; therefore, several concepts were explored for the frame design and a Trade-Off analysis was performed to select a concept to pursue. Detailed design of the other components

would be based on the frame design. Among the frame concepts were a single flat plate design, a multiple flat plate design, and a tubular design.

3.2.1 Single Plate Design

Initial brainstorming for the ARMMACS frame concept yielded a single plate structure as shown in Figure 3.1 with the addition of mounts for the various components. Simplicity is the primary advantage of this concept, because it requires the design and manufacture of few critical parts. Design and manufacturing costs are highly dependent on the quantity of manufactured parts, thus this concept may result in the least expensive robot as well. Additionally, attaching all parts to a single plate simplifies achieving precise assembly tolerances.

Unfortunately, there are significant drawbacks to this design. The most obvious drawbacks are the low bending strength and stiffness to weight ratios occurring because the cross sectional moment of inertia is proportional to the cube of the thickness. Thus, regardless of the material used, the plate will need to be thick to be stiff. Also, to maximize the manipulator workspace, the manipulator must be mounted as low to the ground as possible. If a single plate were used, then the entire plate would be close to the ground and component placement would be limited to the top side of the plate. Placing all components on one side of the plate forces adjacency of components if additional brackets are not designed to stack and isolate them. Placing specific electrical components adjacent to one another increases the risk of electromagnetic noise problems, whereas, additional brackets add weight to the already inherently heavy design. Also, the design provides no shielding or protection of the servomotor and control cabling. Susceptibility to electromagnetic noise and noise emissions from these cables may result in noisy encoder signals. Furthermore, cable damage may result in temporary

loss of control of the robot causing human injuries or costly damage to the machine; therefore, these cables should be protected. Installing conduit solves these problems but increases the weight of the Frame.

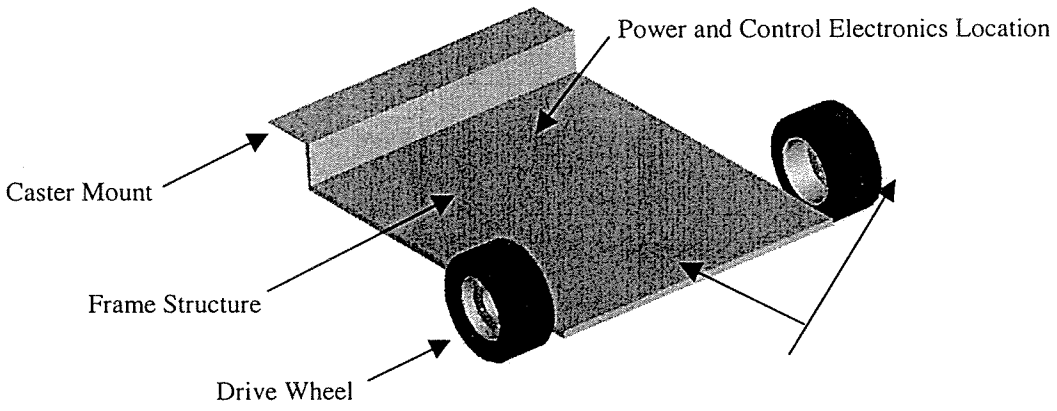

Figure 3.1: Single Plate Frame Concept

3.2.2 Multiple plate design

A design implementing an elevated main plate and several flat plates as shown in Figure 3.2 improves many weaknesses of the single plate design. Vertical flat plates attached to the horizontal main plate will lower the mounting surface of the manipulator. These drop brackets will add height to the frame cross-section and if they are attached securely to the main plate, they will increase the bending and torsional stiffness of the Frame. Consequently, a thinner main plate might provide sufficient stiffness and presumably this design will yield a higher bending stiffness to weight ratio than a single plate. In addition, elevating the main plate enables attachment of components to both sides of the plate. Consequently, brackets for stacking are not necessary, and the main plate will isolate components from one another.

This concept improves upon the single plate design, but its shortcomings prevented it from being used. The potential for increasing the stiffness ratio exists; however, joints often require additional material for fastening (e.g., thicker plates or separate joints), and this will increase the weight and reduce stiffness to weight ratio improvements. While mounting components to both sides of the main plate is advantageous, a disadvantage also exists. Components mounted to the bottom of the plate will be difficult to service or modify. Furthermore, this concept requires several parts, resulting in higher design and manufacturing costs.

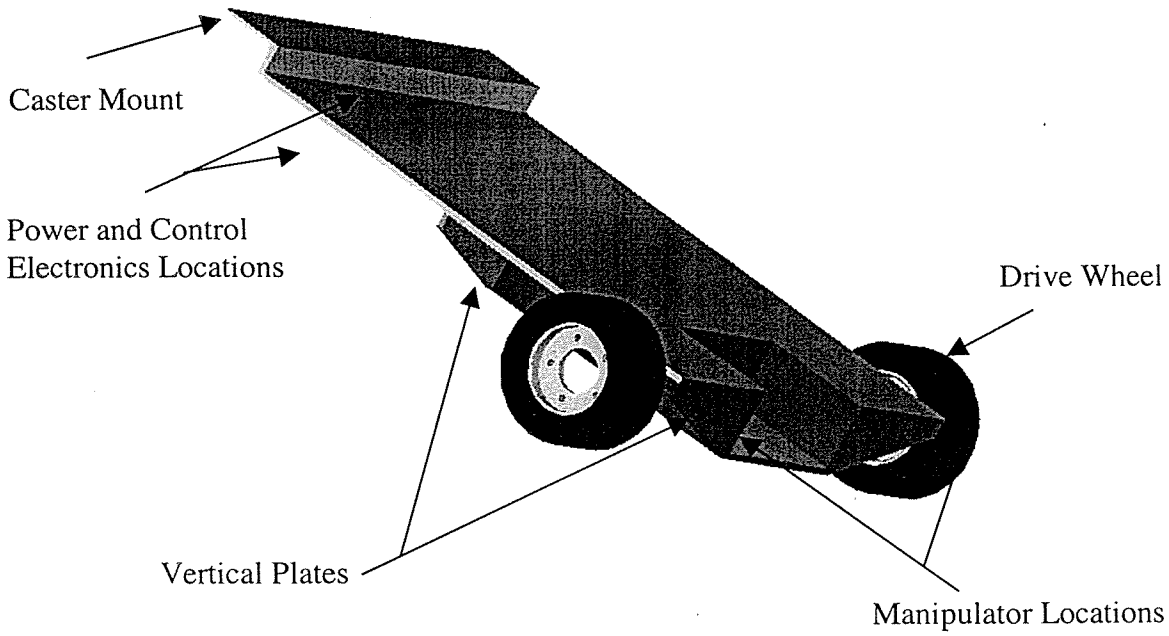

Figure 3.2: Multiple Plate Design

3.2.3 Tubular design

The Trade-off analysis shown in Table 1 resulted in the selection of a tubular frame design as shown if Figure 3.3. For most practical materials, this design will yield high strength

and stiffness-to-weight ratios, which are critical for achieving weight requirements while providing precise and stiff mounting locations for the manipulator and sensors. A high strength to weight ratio is also important for providing a versatile test platform capable of various, currently unknown, loading conditions. Preliminary design calculations proved this frame concept to be approximately 23.6 kg (52 lb) lighter than the single plate concept if each were made of aluminum, yet it would be much stiffer. Additionally, the structural tubes serve as conduit providing physical protection and EMI shielding for cabling. Tubing geometry lends well to a two level architecture increasing the ability to separate components. Physically separating components will help to isolate sensitive components from electromagnetic noise. Several components can be mounted at the bottom level of the tube, with their bodies standing within the height of the tube, and others can be mounted at the top level of the tube extending above the tubes.

As with the other concepts, this Frame also has disadvantages. Several critical components make up the Frame; therefore, the cost of this Frame is most likely higher than the other options. Also, precautions must be taken during design and manufacture to ensure that tight assembly tolerances necessary for manipulator, platform and sensor calibration are met.

Because the ARMMACS is a test bed and only one will be built, design and manufacturing costs are less critical than versatility and functionality; therefore, the advantages of this design outweigh the disadvantages.

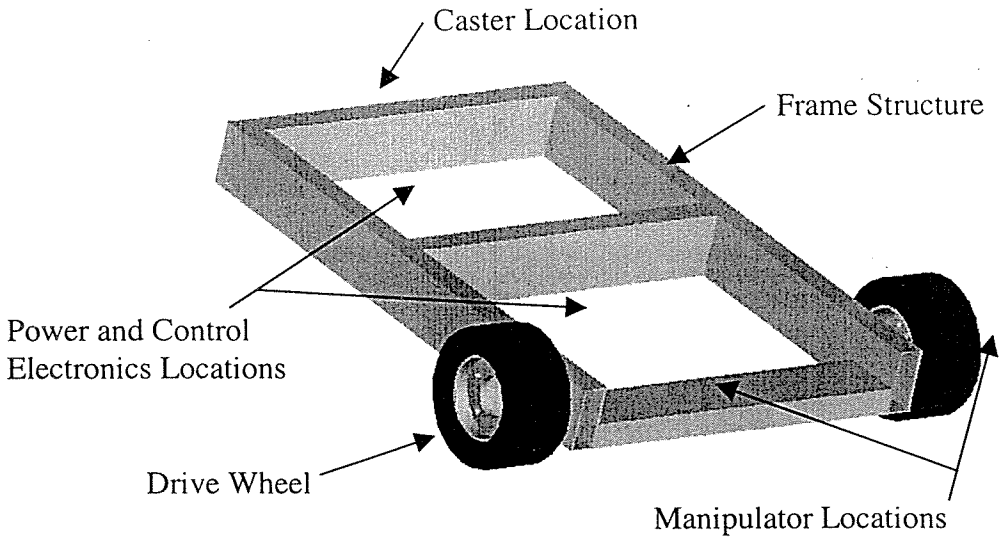

Figure 3.3: Tubular Frame Concept

Selection Criteria	Weight	Frame Concept					
		Single Plate		Multiple Plate		Tubular	
		Rating	Weighted Score	Rating	Weighted Score	Rating	Weighted Score
Stiffness/weight	20.00%	1	0.2	3	0.6	5	1
Cost	5.00%	5	0.25	3	0.15	2	0.1
Cable noise shielding	20.00%	1	0.2	3	0.6	5	1
Cable protection	10.00%	1	0.1	1	0.1	5	0.5
Component isolation	15.00%	1	0.15	4	0.6	5	0.75
Compactness	10.00%	1	0.1	5	0.5	3	0.3
Component accessibility	20.00%	3	0.6	1	0.2	5	1
Total Score			1.6		2.75		4.65
Rank			3		2		1
Continue?			**No**		**No**		**Yes**

Table 3.1: Frame Concept Trade-Off Analysis

3.3 Suspension concepts

The PDS specify that the platform should be allowed constrained roll and heave under normal operation and that 1.27 cm – 2.54 cm (1/2 in – 1 in) of compliance at each wheel and caster is desired. This section presents the suspension concepts that were considered as methods for achieving this compliance. Separate concepts are explored for the drive wheels and the

casters. Capabilities, advantages, and disadvantages of each concept are discussed, and the Trade-Off analysis used to select a concept for the drive wheel compliance is presented.

3.3.1 Rear Suspension

Sprung casters were selected to provide a low cost and low complexity suspension for the rear of the ARMMACS platform. Compliance is provided by two parallel coil compression springs with adjustable preload, and the mechanism allows 2.54cm (1 in) of maximum deflection. The suspension is not damped except for the inherent damping within the elastomer tires and the friction damping within the suspension mechanism. The springs can easily be replaced with springs having different spring rates or with elastomer springs that would provide both compliance and damping.

A few other options were explored to ensure that sprung casters were the best choice. One method involved attaching standard casters to sprung and damped swing arms, so that each caster would comply independently. Another concept attached both casters to a single suspended member. Both of these methods would require the design and manufacture of several components, and would not perform significantly better than sprung casters; therefore, sprung casters were a good choice.

3.3.2 Front Suspension

Suspending the front (drive wheel) end of the platform is far more complex than suspending the rear because torque must be transmitted to the drive wheels and tractive forces are transmitted to the Frame through the suspension. Three suspension concepts were considered. In the first method, the entire Drive Train assembly would be suspended by attaching each motor,

Drive Train, and wheel assembly to a suspended swing arm that pivots at the Frame structure. The second idea was to suspend only the wheel and rigidly mount the motor and gearhead assemblies to the Frame structure. In this concept, the wheel would be suspended on a swing arm or A–arm pair, and torque would be transmitted from the gearhead output shaft to the wheel via half-shafts. The last option considered was to mount the motor and gearhead assemblies directly to the Frame, rigidly attach the Drive Train and wheel to the gearhead, and achieve suspension by using sufficiently compliant tires. A Trade-Off analysis was performed rating each of these methods against the following criteria: drive train torsional stiffness, drive train backlash, drive train complexity, suspension complexity, suspension effectiveness, and suspension weight.

Further consideration of the concept that suspended the entire Drive Train determined that the ratio of sprung weight to unsprung weight would be small, which would result in poor suspension performance. In fact, the suspension may not deflect when the tire crosses workspace surface irregularities. Consequently, the effectiveness of this suspension would be minimal. The tractive forces that accelerate the platform would be transmitted through the swing arm and the pivot; therefore, they must be strong enough to support these loads. Moreover, deflection of the pivot and swing arm will add error to the wheel location, which may add to positioning error. However, a stiff swing arm assembly would most likely be heavy, making it more difficult to achieve weight specifications. For these reasons, pursuit of this concept halted.

The second concept, which considered suspending only the wheel, improves upon the performance of the first concept by greatly increasing the ratio of sprung weight to unsprung weight. In addition, while all the forces are still transmitted through the suspension pivots, the reduction of suspended components makes it easier to implement A-arm type suspension

members (single or paired). These arms would be more compact, and their geometry leads to a higher stiffness-to-weight ratio; therefore, this concept would also lead to a lighter suspension assembly. This concept also has disadvantages that outweigh its benefits. Shafts with flexible joints would be required to transmit torque from the gearheads to the wheels. These shafts would be relatively long, and each would have a joint on each end. These features would inherently reduce the torsional stiffness and increase the backlash of the Drive Train. Careful design, manufacture, and component selection may alleviate these problems; however, the time and funds necessary for this development exceed the scope of the project.

The last concept, which implements compliant tires to suspend the front of the platform, was determined to be most promising. Although compliant tires will decrease the torsional rigidity of the Drive Train, this system is as light weight as possible, and does not add backlash to the Drive Train. Furthermore, while the tire may not suspend the platform as well as the second concept, they will provide sufficient degrees of freedom. Therefore, after studying the feasibility of a suspension mechanism for the front of the platform, the design team decided using compliant drive tires was the most appropriate choice.

		Suspension Concept					
		Suspended Drive Train		Suspended Wheel		Compliant Tire	
Selection Criteria	weight	Rating	Weighted Score	Rating	Weighted Score	Rating	Weighted Score
Drive train backlash	25.00%	5	1.25	2	0.5	5	1.25
Drive train complexity	5.00%	5	1.25	2	0.5	5	1.25
Drive train torsional stiffness	25.00%	5	0.25	2	0.1	3	0.15
Suspension complexity	5.00%	3	0.15	3	0.15	5	0.25
Suspension effectiveness	20.00%	2	0.4	5	1	3	0.6
Suspension weight	20.00%	2	0.4	3	0.6	5	1
	Total Score		3.7		2.85		4.5
	Rank		2		3		1
	Continue?		No		No		Yes

Table 3.2: Suspension Concept Trade-Off Analysis

3.4 Drive Train Concept Selection

This section presents the conceptual design of the Drive Train. Section 2.3.2 concluded that using parallel conventional wheels is the most robust and cost effective of the methods explored for propelling and steering the ARMMACS platform. Now that the wheel configuration is known, a Drive Train must be developed to transmit the external loads acting on the tires to the Frame and to apply power to the wheels. Included in the Drive Train are all the components from the power source to the tire.

The PDS state that servomotors and precision gearheads are available and should be used if they produce the required power. Many devices produce rotary power; however, a quick review of the most common devices verifies that servomotors are the best choice for this application. Combustion engines are commonly used to transfer fuels into rotary power. Combustion engines are capable of large power to weight ratios and notable crankshaft speed. However, combustion engines are clearly the wrong choice for the mobile manipulator for the following reasons:

1. they exhaust deadly gases that must be piped from indoor work environments,
2. either two engines or differential gearing would be required to produce differential, wheel speeds and two engines would be difficult to calibrate,
3. a transmission would be required to reverse wheel rotation,
4. a clutch and brakes would be required for steering and positioning,
5. they produce large vibrations that would result in encoder noise, and
6. they would require a complex controller and several actuators to control the transmission, brakes, clutch and throttle

Hydraulic orbit motors are also used to produce rotary power. These motors are also capable of large power to weight ratios and moderate shaft speeds. Hydraulic motors are a better choice than combustion engines, but still are not the best choice for the following reasons:

1. they require a pump, reservoir, and valves that would enlarge the platform footprint
2. hydraulic fluid leaks would contaminate the workspace causing wheel skid and less predictable kinematics, and
3. delays between valve commands and actuator response, as well as system compliance are difficult to model exactly which would increase position uncertainty

On the other hand, electric servomotors are an excellent method for propelling the platform because:

1. with a gear reduction they provide power to weight ratios that are sufficient for the ARMMACS application,
2. they are capable of high shaft speed which, through simple gearing, can be transferred to higher torque,
3. they will not contaminate the workspace or the control electronics,
4. their power and their rotation angle can be controlled precisely and they can rotate in either direction,
5. they produce minimal vibration, and
6. they are designed to be controlled by a computer and are relatively easy to incorporate with the robot controller.

Preliminary kinematic and dynamic calculations determined that the Electro-Craft F4050 servomotors coupled with the Bayside RA115 20:1 planetary gearheads provide ample power. These gearheads are designed for precision applications that utilize servomotors. Thus, the gears

and shafts are torsionally stiff and have minimal backlash. Therefore, they satisfy the PDS and are an excellent choice for the ARMMACS. Consequently, these motors and gearheads will be used.

3.4.1 Mechanism for Coupling the Wheels to the Gearheads

Forces acting on the tire will be transmitted to the hub on which the wheels are mounted. Radial, axial, and tangential forces will occur at the tire/ground interface. Radial force will act on the wheels due to the static weight of the system, vertical accelerations of the platform from workspace surface irregularities, and possibly from manipulator accelerations. Axial force will occur in the tires when the platform corners and possibly when the manipulator accelerates. The tangential force occurring at the tire/ground interface is characterized by longitudinal tire slip, and results from longitudinal platform acceleration.

These forces maneuver the platform; therefore, they must be transmitted from the tire contact patch to the platform Frame. The current section presents the conceptual design of the mechanism that will transmit these forces. As specified in the PDS, backlash between the motor and wheel should be limited to that within the gearheads, and the torsional stiffness of the Drive Train must be high, preferably with a natural frequency greater than 500 Hz. Before the geometry of this mechanism could be conceptualized, it was necessary to determine the tire dimensions. Vehicle kinematic and dynamic performance requirements, the servomotor specifications, the gear reduction ratio, and estimated platform weight and inertia parameters were used to determine the required tire diameter. After calculating the approximate tire diameter, tire types that provide the desired compliance were investigated to determine stock diameters and widths. From this investigation, it was concluded that the wheel mounting-flange

must be offset approximately 8.89 cm (3.5 in) from the gearhead face to provide sufficient tire clearance. The gearhead output shafts are 5.08 cm (2 in) long; therefore, based on geometry alone, the wheels cannot be coupled to the gearheads without a shaft or hub that extends the output shaft. Forces acting at the ground/tire interface will be transmitted to this extension shaft; therefore, the shaft and its supports must be designed to withstand these loads. Preliminary calculations showed that the radial loading would result in the most critical stresses.

Bayside specifies a static radial load rating of 499.4 kg (1100 lb) applied to the output shaft 2.54 cm (1 in) from the gearhead face. Reaction forces at the bearings increase when the load is applied further from the gearhead face; therefore, Bayside recommends this rating be reduced by a cumulative 25% (ie. the 25% is taken from the already reduced value) for each additional 2.54 cm (1 in) beyond this 2.54 cm (1 in). Using this formula, the static radial load rating is reduced to 245.8 kg (541.4 lb) when the load is applied 8.89 cm (3.5 in) from the gearhead face. Typically, the radial load rating is reduced significantly further when dynamic load is accounted for through life cycle calculations. To account for dynamic load, Bayside recommends providing them with the radial loading scenario, speed vs. time profiles, and torque vs. time profiles for life cycle analysis with proprietary software.

3.4.1.1 Shaft Extension Concepts

The design of the Drive Train assembly will be dictated by the selected shaft extension design concept; therefore, it is discussed first. Three conceptual designs were considered for extending the gearhead shafts:

1. attaching the shaft extension directly to the gearhead shaft with no additional support,

2. supporting the outboard end of the shaft extension with a single bearing, and supporting the other end with the gearhead shaft, and
3. fully supporting the shaft extension with a pair of bearings and coupling it to the gearhead shaft with a separate stock shaft coupling.

To analyze and compare these concepts, it was assumed that the two methods utilizing bearings would use either Deep Groove Ball, Angular Contact Ball, or Tapered Roller Bearings. These concepts were then ranked in the Trade-Off analysis shown in Table 3.3 to converge on the most promising design. The criteria used in the analysis were the radial load carrying capability, the axial load carrying capability, cost, complexity, and the ability to adjust the friction torque of the Drive Train assembly.

3.4.1.1.1 Shaft Extension Supported Only by the Gearhead Output Shaft

A shaft extension (Drive Shaft) that is supported only by the gearhead output shaft would be simplest to implement. A mechanical interference style coupling could be incorporated directly into the Drive Shaft, or a separate rigid shaft coupling could be used to couple the Drive Shaft with the gearhead shaft. With this design, the Drive Shaft and the wheel flange could possibly be combined into one piece; therefore, it is possible that only one component per wheel would be needed. Consequently, this design would require the fewest parts and provide the most compact and lightweight mechanism. However, with this design all external loads are transmitted to the gearhead shaft, and supported by its bearings. To minimize gear wear and ensure long term reliability and accuracy of the gearheads, the design team decided the Drive Shaft should be supported by some combination of designated bearings. Therefore, this design was not selected.

In addition to transmitting external loads to the Frame, if the preload of these bearings is adjustable, the total drive train friction torque will be adjustable. Adjustment of the drive train friction torque may compensate for friction differences within the gearheads and performance differences of the servomotors. This compensation will help in synchronizing the Drive Trains powering each wheel, which is a must for torque mode operation. If they are not synchronized, identical torque commands sent to each motor will result in differing torques at the wheels and the platform will not follow commanded trajectories. Obviously, significantly over or under loading the bearings would damage them, which limits the adjustment capability. Bearings that require radial preload (i.e., preload from interference fits) do not provide this advantage because radial preload cannot be adjusted. Therefore, the bearings considered will be limited to those that require axial preload, and the axle and shaft design will provide a preload method.

3.4.1.1.2 Shaft Extension Supported by a Single Outboard Bearing

Supporting the outboard end of the Drive Shaft with a single bearing will reduce the radial force transmitted to the gearhead Output Shaft, and thus reduce the stresses in the shaft in the bearings. If a single bearing is used, the inboard end of the shaft must be supported by the gearhead Output Shaft; thus, the bearing must be mounted coaxial with the gearhead Output Shaft within tight tolerances. To axially preload a single bearing, the coupling attaching the Drive Shaft to the gearhead Output Shaft must be capable of supporting sufficient axial force. Axially preloading the bearing will result in axially loading the gearhead bearings. This design decreases the radial loading on the gearhead, which may increase the long-term reliability of the gearhead; however, it does not isolate the gearhead from all external radial loads and it biases the axial load acting on the system. In addition, this design concept adds significant mechanical

complexity to the Drive Train. For example, a tight-tolerance axle must be designed and manufactured to support the bearings and transmit the external forces from the bearings to the Frame. The axle must also be designed so that the bearing preload is adjustable, so that the bearing can be lubricated, and to seal the bearing from contaminates. Since the exact effects of decreasing the radial load and biasing the axial load are difficult to determine, the added value of the single bearing design may not justify the increased complexity.

3.4.1.1.3 Shaft Extension Fully Supported by a Pair of Bearings

By adding minimal complexity and cost to the axle and shaft, the shaft can be fully supported such that only torque acts on the gearhead output shaft. This will result in minimum gear and bearing wear, and the longest gearhead life. Thus, it was decided that the wheel would be fully supported by two designated bearings that are supported by an axle. The axle will transmit all external radial and axial loads directly from the bearings to the Frame. Due to geometric compatibility, slight axial misalignment between the inboard and outboard bearings or between this bearing pair and the gearhead Output Shaft could result in extremely high stresses within the shafts and bearings. Therefore, a coupling method that compensates for misalignments (i.e., transmits minimal bending moments and radial forces) will be used to couple the shafts, and the axle will be designed with tight tolerances to ensure near perfect bearing alignment.

Selection Criteria	weight	Extension Shaft Selection					
		No Support Bearing		One Support Bearing		Fully Supported	
		Rating	Weighted Score	Rating	Weighted Score	Rating	Weighted Score
Axial load carrying capability	25.00%	0	0	3	0.75	5	1.25
Complexity	15.00%	5	0.25	2	0.1	0	0
Cost	5.00%	5	0.75	3	0.45	0	0
Friction torque adjustability	25.00%	0	0	2	0.5	5	1.25
Radial load carrying capability	30.00%	0	0	3	0.9	5	1.5
	Total Score		1		2.7		4
	Rank		3		2		1
	Continue?		No		No		Yes

Table 3.3: Drive Shaft Concept Selection

3.4.1.2 Axle Design Concept

A non-rotating axle must be designed to transmit the external radial and axial loads from the bearings that support the Drive Shaft to the Frame. This axle will be attached to the Frame and support the fixed bearing raceways radially and axially. After reviewing the geometry of the gearhead and the Frame and deriving several possible axle and Drive Shaft configurations, it was decided that a hollow axle should be used, and the rotating Drive Shaft should pass through the inside of the axle. Using this design, the outer bearing race is fixed and supported by the axle, and the inner race rotates and supports the shaft.

Bearings that are preloaded by axially displacing one of the raceways with respect to the other will be used. For a rotating inner ring load, the inner ring should be press fit tightly on the shaft, and the stationary outer ring should have a transitional fit in its housing so that it can be displaced for adjusting preload. An external thread lock-nut arrangement was considered for adjusting preload. However, estimated machining costs for this arrangement were high; therefore, a shimmed bearing retainer fastened by standard bolts was selected.

3.4.1.3 Method of Transmitting Torque to the Fully Supported Drive Shaft

Torque produced at the output end of the gearhead must be transmitted to the Drive Shaft powering the wheels. Because the Drive Shaft is fully supported by designated bearings, it does not need to be supported by the gearhead Output Shaft. Therefore, the Drive Shaft does not need to be coaxial with the gearhead Output Shaft. Several components are available to transmit power from one rotating shaft to another for various shaft orientations. Coaxial shafts can be coupled using one of several styles of stock shaft couplings. On the other hand, common methods for coupling offset parallel shafts include belts, chains, and gears.

Conventional chains will not suffice as a Drive Train for servomotor applications because they allow backlash and typically are not stiff enough in tension. In addition, conventional chains wear relatively quickly which will result in deterioration of the servo tuning and compel a need for regular maintenance. Although it is possible to design a gear system that contains virtually no backlash, it would require expensive gears and a close-tolerance housing as well as a lubrication method. Accordingly, there are much less expensive and more practical ways for coupling the shafts. Both timing belts and shaft couplings would provide sufficient performance; however, shaft couplings and a coaxial configuration were chosen for the design.

Both the gearhead and the Axle will be attached to a one-piece Coupling Housing. Each end of the Coupling Housing will be equipped with pilots that mate with pilots on the gearhead and on the Axle to ensure coaxiality of the Output Shaft and the Drive Shaft.

3.4.2 Ensuring Drive Wheel Axial Alignment

Dynamic and kinematic models created by AHMCT researchers to simulate the performance of mobile manipulators, assume perfect axial alignment of the drive wheels, and

assume that the location of the manipulator with respect to the drive wheel axis is known exactly. Physical systems are never perfect or exact; therefore, models are typically perturbed to account for imperfections. However, to properly perturb the model, designers must understand the accuracy of the physical system. Additionally, if critical components are close to perfect, fewer problems come about during implementation. For the computer models to closely represent the mobile manipulator physical system, it is critical that the wheels form a well-defined axle line, that the track width is known closely, and that the manipulator is precisely located. To ensure this, both coupling housings will be aligned on a common plate (Alignment Plate) by dowel pins. This plate will also have mounting provisions for the manipulator. Because all critical components will be mounted to a common plate, the small inaccuracies in their mounting will be well known.

3.4.3 Tire Selection

When torque is applied to a tire, shear forces within the tire cause longitudinal slip. In addition, turning maneuvers induce shear forces within the tire that cause side slip. These slips are often used to determine the longitudinal and lateral reaction forces produced at the tire-ground interface; therefore, understanding them can be critical in modeling ground vehicle dynamics. Additionally, if these slips are not properly accounted for they introduce error in kinematic models. Several tire models exist that characterize this phenomenon. These tire models often require various tire mechanics characteristics that are available for many automotive tires. However, kinematics and geometry dictate much smaller tires for the ARMMACS. Tires available in the desired size are seldom used in precision or performance applications; therefore, the manufactures do not determine the required characteristics for these

tires. By approximating these parameters, a model can be created; however, the model will undoubtedly introduce error into the dynamic and kinematic simulations and thus into controller tuning.

To help understand the effects of tire slip and compliance on platform control, two interchangeable sets of drive tires will be used. One of these sets must have minimal compliance, and the other set should have liberal and adjustable compliance. It was desired that these sets of tires have similar dimensions so that the platform kinematics do not change when the tires are swapped from one set to the other. As concluded in section 3.2.2, tire compliance will also serve as the front suspension for the platform allowing roll and heave.

Using the specifications for the F4050 servomotors and Bayside RA 115 20:1 precision gearheads and inertia estimates for the platform and Drive Train, kinematic and dynamic calculations were performed for the platform to determine the required tire size. These calculations determined a 25.4 cm (10 in) to 30.48 cm (12 in tire) diameter would work well. Weight estimates for the platform were also performed to determine the weight force acting on the drive wheels. Once the load and size requirements were known, an iterative process was carried out to find two sets of tires with different compliance, but similar in size, that would meet all requirements.

3.5 Summary

In this chapter conceptual designs were proposed and analyzed for the ARMMACS Chassis and drive assembly design. Because of a high stiffness-to-weight ratio, an inherent capability to protect cabling and provide Electromagnetic Interference (EMI) shielding for cabling and electrical components, a tubular frame concept was selected. Various suspension

concepts were also presented in this chapter, and it was determined that sprung casters would provide the rear suspension, and compliant tires would act as the front suspension. Once the Chassis concepts were selected, the chapter turned towards the development of the Drive Train. Reasons for using servomotors and precision gearheads were presented. Then a mechanism for coupling the wheels to the gearheads was conceptualized. To retain the accuracy of the gearheads for a greater number of cycles, the selected drive train design concept will support all radial and axial loads applied to the tire, and only torque will act on the gearhead Output Shaft. The chapter then briefly discusses the importance of closely aligning the drive wheel axes, and a design attaching both Drive Trains to a common plate to ensure accurate alignment is presented. Finally, the tire characteristics were discussed, and it was determined that two sets of tires with greatly different compliance would be used to help understand the effects of compliance and slip.

Chapter 4

Detailed Design

4.1 Introduction

In Chapter 3, design concepts were selected for each major ARMMACS subsystem, namely the Chassis and the Drive Train. These ideas must now be taken from conceptual design to a realized product. Various methods were used to finalize the detailed design of each component, depending on the critical requirements and functionality of the component. For some components, stresses were analyzed to determine the component geometry and material needed to prevent failure. Deflection analyses were typically used in designing components that calibrate the vehicle. In other cases, component functionality dictated geometry that resulted in robust components, thus minimizing stresses and deflection. While all design details and iterations cannot be captured in a chapter of reasonable length and clarity, this chapter discusses the design methodology performed for each major component. Results of the most critical design calculations are provided within this chapter while the calculations themselves are embodied in Appendix A. Appendix B contains a complete set of Detailed Component and Assembly Prints.

4.2 Detailed Design of Drive Train

Conceptual design of the Drive Train assembly was discussed in Chapter 3. The selected conceptual design requires that a Drive Shaft, an Axle, a Coupling Housing, and Wheel Flanges be designed. Additionally, adequate shaft couplings, bearings, seals, and tires must be selected from available stock components. A quality Drive Train with minimal backlash, a high torsional natural frequency, and close tolerance geometry is the most critical component of the platform.

Therefore, the Drive Train was designed before the frame when few constraints existed and the design options were plentiful. This allowed stock components to be selected based on their critical performance characteristics rather than by arbitrary geometric constraints. As discussed in Chapter 3, two different sets of drive tires will be used on the ARMMACS platform to understand the effects of tire slip and compliance on platform control. These tires will also propel the platform and serve as front suspension. Selecting two sets of tires similar in size, but with very different performance characteristics required a broad exploration of the many available stock tires and wheels. By selecting the tires before any other Drive Train component, any two sets of tires that met the performance requirements and were of similar size could be used, regardless of their wheel or hub type. Because the platform is a high performance robot driven by servomotors, several constraints were placed on the coupling used to couple the gearhead with the drive shaft. Therefore, this coupling was selected before the design of other drive train components so that any coupling with reasonable size that satisfied all the performance criteria could be used. Once both sets of tires and the coupling were selected, the remainder of the Drive Train components were designed accounting for constraints created by these components.

4.3 Tire and Wheel Selection

Before the search for tires began, a range of tire diameters that satisfies the kinematic and dynamic performance requirements set in the Product Design Specifications was determined. Detailed calculations were performed that accounted for the maximum continuous speed of the available Electro-Craft® F4050 servomotors, estimated Platform, drive tire and wheel inertias, gearhead and servomotor inertias, and the reduction ratio of the available Bayside™ gearheads.

These calculations, shown in Appendix A, determined that the effective tire diameter must be greater than 21.8 cm (8.6 in) and less than 70.1 cm (27.6 in). Because the platform is relatively small and the robot must be close to the ground, the tire search was limited to sizes at the lower end of this range. Also, the estimated maximum static radial load at the maximum platform load was determined to be 778.4 N (175 lb) using the weight estimate shown in Appendix A. Therefore, only tires that could withstand this load while transmitting torque were considered. Furthermore, consideration was limited to tires rated for a minimum speed of 2.3 m/s (7.5 ft/s).

4.3.1 Selection of Tires with Minimal Compliance

Two types of tire and wheel arrangements, and several tire material types were investigated when looking for a tire with minimal compliance. One option was to purchase a one-piece wheel and mold-on tire assembly. Another option was a two piece assembly utilizing a wheel and a separate Press-on tire.

Most one-piece wheel and mold-on tire assemblies are not designed to serve as drive wheels, but rather as casters or idler wheels. Typically, the wheels are made of cast aluminum, cast iron, or phenolic and have a bearing or bushing for use in a free-wheel application. The mold-on tires are available in several natural rubber, neoprene, and polyurethane compounds. Although these assemblies are not typically designed to transmit torque, some manufacturers give rule of thumb load rating reductions for use as drive wheels at low speeds. However, manufacturer representatives feared that periodically reversing the wheel rotation direction and subjecting the tire to high torque would lead to premature delaminating of the mold-on tire. Since ARMMACS is steered by differential wheel speed, these types of actions are probable. Furthermore, some manufacturers, upon special order, provide keyways and set screws for torque

transmission. This coupling method introduces backlash into the Drive Train, which is unacceptable. Machining the hub so that a mechanical interference bushing or a bolted flange could be used to mount the wheel was possible with some of the wheels; however, many of the hubs were thin walled making this impossible. Additionally, the exact value of the desired compliance and the actual tire compliance are unknown; therefore, it is probable that changes will be desired. Since these are one piece wheel and tire assemblies, if the compliance must be changed, an entire new assembly must be purchased and machined. For these reasons, a one-piece tire and wheel was not used.

Finding a two piece wheel and tire assembly required some craftiness. While several manufacturers produce standard size Press-on tires in various polymer compounds and tread patterns, none produce generic wheels. Typically, these tires are designed for material handling equipment such as forklifts and pallet trucks, and the manufacturers of the trucks design wheels for their application. Each truck manufacturer makes a plethora of wheels; unfortunately, they are catalogued by part numbers and complete technical specifications are not available. After visiting forklift distributors, a 12.7 X 16.5 cm (5 X 6.5 in) wheel designed as a drive and steer wheel for a Clark motorized pallet truck with 22,240 N (5000 lb) load capacity was selected. This wheel, shown in Figure 4.1, is designed for mounting to a flange using five studs or bolts, and has a center bore for alignment. By using conical shaped nuts, this mounting is backlash free, and an excellent way to transmit torque.

Several 25.4 cm (10 in) and 26.7 cm (10.5 in) diameter Press-on tires are available with 16.5cm (6.5 in) inside diameters to fit the selected wheels. Since all of these tires are designed to withstand much higher loads and transmit higher torque than the ARMMACS application will present, any of the compounds would provide adequate longevity. While the goal is to select a

tire with minimal compliance, some compliance is necessary to generate traction. Polyurethane compounds are typically stiffer than natural rubber compounds which themselves are extremely stiff for the weight of ARMMACS; therefore, natural rubber was selected for greater tractive force. A Maine Rubber International 25.4 X 12.7 X 16.5 cm (10 X 5 X 6.5 in) Energy King (M-68) natural rubber tire was chosen because it meets the size requirements and extensive technical data was available from Maine Rubber International. This tire is rated for 8184.3 N (1840 lb) at 4.5 m/s (14.7 ft/s) which far exceeds the load requirements of ARMMACS. Detailed technical data may be helpful when creating tire models and is provided in Appendix C.

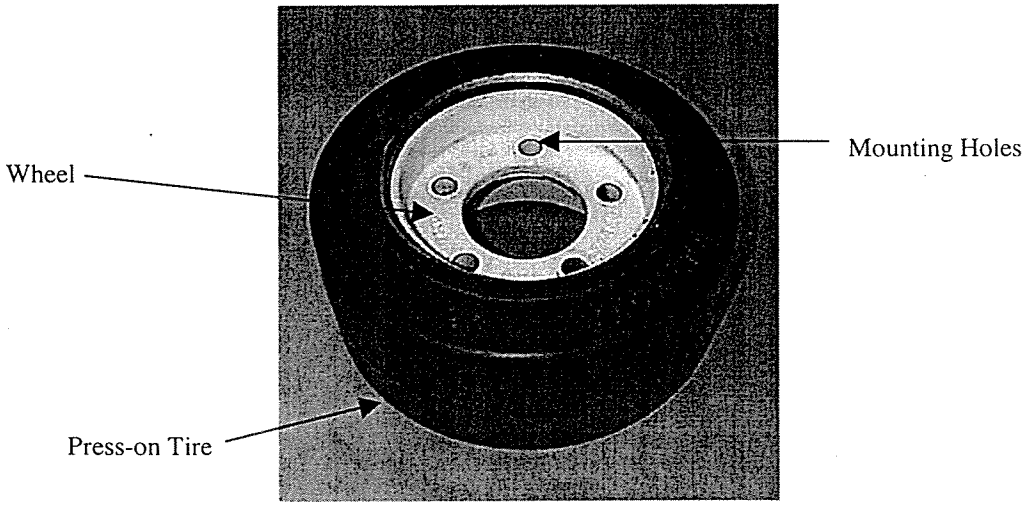

Figure 4.1: Minimally Compliant Tire Wheel

4.3.2 Selection of Tire with Liberal Compliance

Semi-pneumatic and Full-pneumatic tires are very compliant and both were considered for use as the more compliant tire. Both Semi-pneumatic and Full-pneumatic tires are available in diameters near 25.4 cm (10 in). However, Semi-pneumatic tires operate at atmospheric pressure and their pressure is not adjustable; therefore they do not satisfy the adjustable

compliance requirement. Also, load ratings for 25.4 cm (10 in) diameter Semi-pneumatic tires are typically significantly lower than for Full-pneumatic tires this size. Consequently, 410/3.50-4 Full-pneumatic tires were selected as the compliant drive tires. These tires are rated for a radial load of 177.1 kg (390lb) at 4.5 m/s (14.7ft/s) for manual operation. The nominal (unloaded) diameter of these tires is 27.7 cm (10.9 in). However, they will deflect further than the minimal compliance tires and their effective radius will be nearly the same. Although they are not rated for transmitting torque, they are often used flawlessly in light-duty drive wheel applications. Additionally, since the load rating far exceeds the design requirement, problems are not expected. Torque is easily transmitted to these tires which are mounted to stamped steel wheels designed for mounting to a flange using four studs or bolts.

The Full-pneumatic tire is much lighter than the minimal compliance tire, and higher percentage of its mass is closer to the axis of rotation; therefore, its rotational inertia will be lower than the inertia of the minimal compliance tire. However, as shown in the calculations determining the maximum tire diameter shown in Appendix A, this inertia is negligible compared to the platform inertia, therefore, the effects on performance should be minimal.

4.4 Shaft Coupling Selection

Servomotors implementing feedback control are sensitive to backlash and torsional windup between the motor shaft and the load. Since servomotors propel the ARMMACS platform, the Product Design Specifications require that all backlash in the Drive Train joining the motors and the wheels be inherent to the gearhead, and that the natural frequency of the Drive Train be 500 Hz minimum. Taking these precautions during the mechanical design increases the accuracy of dynamic models, which typically neglect these effects. Thus, control algorithms

designed using these simulations should transfer more easily to the physical system. More importantly, without these anomalous characteristics to account for, control algorithms and servo tuning should be simplified. In an effort to achieve these two design goals, the shaft coupling that joins the gearhead output shaft and the Drive Shaft was selected carefully. Also, torsional stiffness was a critical design parameter for the Drive Shaft.

Preliminary calculations were performed to determine the maximum torque the coupling must transmit and to determine the minimum bore diameter needed for the shaft to satisfy the natural frequency requirements and to have a long fatigue life. The maximum torque the coupling must transmit is limited by the friction force between the tire and the ground and was determined to be 69.3 N-m (613 lb-in) as shown in Appendix A. A spreadsheet (shown in Appendix A) was developed to determine the natural frequency of the Drive Shaft and the Drive Train. By substituting shaft diameters into this spreadsheet, the minimum shaft diameter at the coupling was determined to be 2.3 cm (0.9 in). Additionally, it was determined that only unreasonable increases would significantly increase the drive train natural frequency. An appropriate shaft coupling was selected using the criteria shown in Table 4.1 before the other drive train components were designed. Bellows, Chain, Composite Disk, Elastomer Jaw, Multi Beam (Coil), Rigid, and Single Beam (Coil) type couplings were all considered.

Properties of stock couplings that met the bore size requirement were evaluated against the selection criteria to determine the potential of each coupling type. To expedite the remainder of the drive train design, which was pending coupling selection, special orders were not considered. As an initial measure, each coupling type was evaluated against the maximum torque requirement. Next, they were evaluated to determine whether backlash existed within the coupling and whether they allowed shaft misalignments. To prevent the high radial stresses that

occur when slightly misaligned shafts are forced into geometric compatibility by rigid coupling, the selected coupling needed to allow angular and parallel misalignments. Additionally, the hub options were examined to determine how the hubs mated to the shafts. Keyed and set screw fits often cause backlash, hence they were unacceptable. Hubs implementing mechanical interference fits by means of clamps or tapered bushings were sufficient because they produce reliable, zero backlash joints. Furthermore, using the natural frequency program, the torsional stiffness of each coupling was analyzed to determine its effect on the drive train natural frequency. Also, because the platform weight should be kept relatively low, and the envelop relatively small, the coupling dimensions were limited to 10.2 cm (4 in) in diameter and 10.2 cm (4 in) long.

A Zero-Max 6A37C Composite Disk coupling was selected. This coupling, shown in Figure 4.2, is rated to transmit 135.6 N-m (1200 lb-in) of torque with clamp style hubs. For a reversing load application without shock the manufacturer recommended a service factor of one; therefore, this coupling provides a factor of safety against slip of 2, and a larger factor of safety against failure. Neglecting the tire compliance, the natural frequency of the Drive Train using this coupling is 400 Hz. Although this natural frequency is less than the specification, the torsional stiffness of this coupling far exceeds other couplings that allow misalignment and transmit the required torque. Small gains are earned by utilizing a larger Composite Disk coupling, but they are not worthwhile. Special disk packs with thicker disks or disks with shorter arms will increase the torsional stiffness significantly, while sacrificing some misalignment capability. However, unless the torsional stiffness of the shaft and coupling are unreasonably high, a drive train natural frequency of 500 Hz will never be achieved due to tire compliance.

Therefore, the stock coupling will be used. Even the stiffest tire will significantly reduce the natural frequency of the Drive Train because compliance is requisite to generate tractive force.

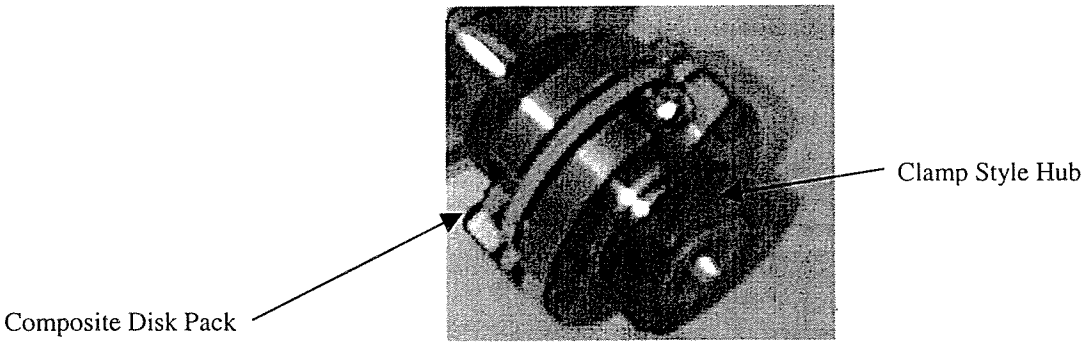

Figure 4.2: Zero-Max 6A37C Composite Disk Coupling

	Coupling Type						
Selection Criteria	Bellows	Chain	Composite Disk	Elastomer Jaw	Multi Beam (Coil)	Rigid	Single Beam (Coil)
Torque Range	n	y	y	y	n	y	n
Backlash Free Coupling	y	n	y	n	y	y	y
Torsional Stiffness	n	?	y	n	n	y	n
Backlash Free Hubs	y	y	y	y	y	y	y
Angular Misalignment	y	y	y	y	y	n	y
Parallel Misalignment	y	y	y	y	y	n	y
Reasonable Dimensions	y	y	y	y	y	n	y
Pursue Further	**NO**	**NO**	**YES**	**NO**	**NO**	**NO**	**NO**

Table 4.1: Coupling Selection

4.5 Coupling Housing Design

A Coupling Housing was designed to join the gearhead casing and the axle and to shield operators from moving coupling components. Because of the desired alignment accuracy, and

the required strength and dimensions of the structure, it was made as a separate part rather than integrated into the frame members. This also increased the modularity of the Chassis allowing parts to be fabricated while others were being designed. Before selecting the one-piece design shown in Figure 4.3, several multi-piece options were considered. Designing the part as an assembly of multiple parts made from stock shapes would have required more design time. Also, the assembly would have been more expensive to machine and there were no cost savings in material. In addition to the added design time and manufacturing cost, tolerance stack-ups would have resulted in increased parallel and angular shaft misalignments.

This one-piece coupling housing was designed and machined to close specifications to ensure that the gearhead Output Shaft and the Drive Shaft are aligned within the Composite Disk Coupling specifications. A female alignment pilot machined into one face of the coupling housing mates with a male alignment boss on the gearhead casing. A male alignment boss is machined into the opposing face of the coupling housing, which mates with a female pilot of the axle. The boss and pilot on the coupling housing are concentric within close tolerance to ensure nearly perfectly concentric shafts. Furthermore, these faces are machined parallel to one another within tight tolerance meet the angular misalignment specifications of the coupling. In addition to the shafts being concentric, to meet parallel misalignment specifications, these faces are also perpendicular to the through bore within close tolerance. To ensure that the axes of the right and left Drive Wheels are coaxial, two dowel pins are used to precisely locate the couplings on a common plate.

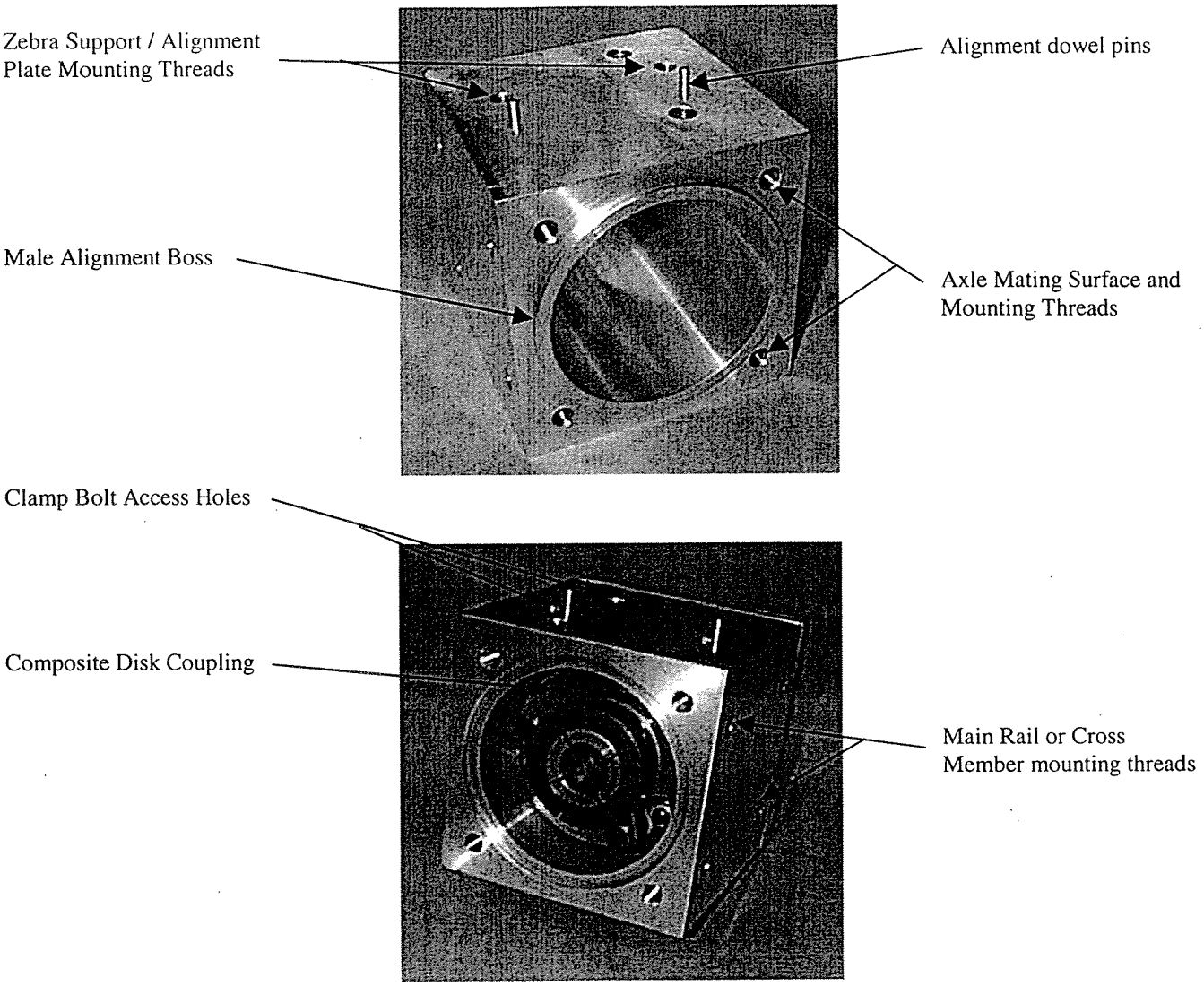

Figure 4.3: Coupling Housing and Coupling

Every face of the Coupling Housing, except the top, is tapped with 7.94 mm (5/16 in)-18 thread groups. These threads are used to attach the Gearheads and Axles to the Coupling Housings, and to attach the Coupling Housings to several frame members. All of these threads were designed with an engagement length such that 7.94 mm (5/16 in)-18 Socket Head Cap Screws with 1241.1 MPa (180,000 psi) yield strength will break before internal threads strip. Then stainless steel HeliCoil® thread inserts were used to increase strength and to improve the durability of the threads for multiple uses. The minimum engagement length for 7.94 mm (5/16

in)-18 6061-T651 AL threads without inserts is 1.75 cm (0.69) in. 7.94 mm (5/16 in)-18 Socket Head Cap Screws provide a safety factor against yielding of 1.5 for the bolts with the highest loading (including preload). Appendix A shows the thread engagement length and bolt stress calculations. Because the shear area of threads cut for the inserts is significantly larger, the threads cut in the housing will be stronger than 7.94 mm (5/16 in)-18 threads. Additionally, the inserts transform shear force into radial and shear force components, which better distribute the loading over the engagement length. Therefore, the 1.59 cm (0.625 in) long inserts used are sufficiently strong. Other stresses in the Coupling Housing due to external loading were assumed to be negligible since all critical cross sections are reinforced by other components (e.g. Gearhead, Axle, Main Rail and Cross Member Flanges).

4.6 Design of Axle Assembly

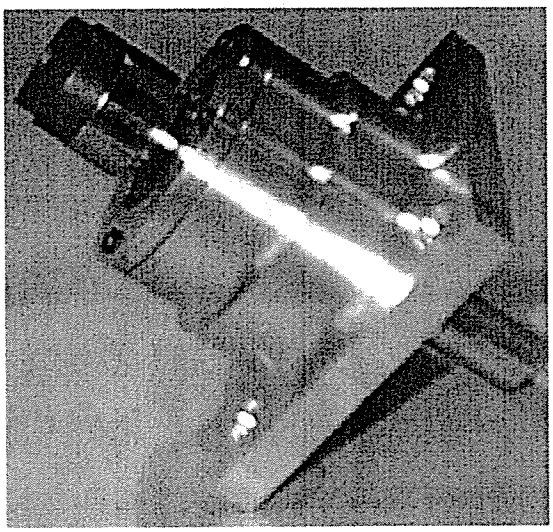

Figure 4.4: Drive Axle Assembly

Several custom designed machined components and stock purchased components make up the Axle Assembly shown in Figure 4.4. Custom designed and machined components include the Axle, Drive Shaft, Bearing Retainer, Solid Tire Flange, and Pneumatic Tire Flange. Standard

purchased components included the bearings, seals and tires. Because these components join together into an assembly and are interdependent, iterations are required to design and select components that meet all performance and geometric requirements. Design and/or selection of each aforementioned component is discussed within this section.

4.6.1 Drive Shaft Design

To provide sufficient tire clearance the Gearhead Output Shaft was extended with a Drive Shaft. Following arguments made in the previous chapter the Drive Shaft is designed to transmit Gearhead output torque to the Drive Wheels, and to support all forces acting on the tire. Several key parameters dictated the design of the Drive Shaft. These parameters include torsional natural frequency, fatigue life, static load yielding, and meeting the geometric requirements of the tires, bearings, seals, and couplings. As a result, concluding on a final design required several iterations and, for the most part, only the characteristics of the final design are presented here.

Supporting all forces acting on the tire places axial loads, bending moments, and torque on the shaft. These forces establish a combined state of stress within the Drive Shaft. The critical stresses within the shaft are the shear stress due to torsion, and the normal stress due to bending. The shaft rotates and the radial loads and moment are nearly stationary, this places the shaft in completely reversed bending. Additionally, the torsional stress fluctuates and reverses during operation; however, the fluctuation frequency varies. Because the Drive Shaft is subject to dynamic loads, two possible failure modes were analyzed. Static yielding under maximum load is one possible failure mode, and fatigue failure is the other.

The Distortion Energy failure theory was used to determine the factor of safety against yielding. Von Mises stresses were calculated for the maximum loading case and compared to the

yield strength of the shaft material. Stressproof AISI 1144 cold drawn bar was selected as the shaft material because of its high yield strength of 689.5 MPa (100,000 psi), and its high hardness and machinability. Because the maximum load conditions are not likely to occur often or suddenly, they were treated as static loads. A maximum weight of 2220 N (500 lb), lateral acceleration of 1g, and torque of 69.3 N-m (613 lb-in) were used for the maximum static loads. One g of lateral acceleration is commonly used as a maximum in ground vehicle dynamics. This acceleration is very conservative for the ARMMACS platform, which has only two tires producing lateral force, and does not have suspension. Under these conditions, the calculations in Appendix A give a factor of safety against yield of 3.

Although analytical fatigue failure analysis alone is insufficient when designing mass produced parts or where human safety is at risk, it is the norm for prototypes or parts produced in small quantities where human safety is not jeopardized by part failure. To determine the factor of safety against fatigue failure (for infinite life), Von Mises alternating and mean stress components were determined for use with the Distortion Energy failure theory, and the Modified Goodman failure criterion was implemented to combine the mean and alternating stress components. The following load case, which better represents the normal operating conditions than the maximum load case, was used for the fatigue analysis. Based on the size of the laboratory workspace and the complexity of the control algorithm development, most testing will likely be performed at forward velocities near 0.61 m/s (2 ft/s) and forward accelerations less than 1.83 m/s^2 (6 ft/s^2). The torque required to achieve these accelerations is approximately 60 N-m (531 lb-in). Various maneuvers will require different torque, and the torque was assumed to fluctuate between 2.3 N-m (20 lb-in) and 60 N-m (531 lb-in). Basic dynamic and kinematic models (without tire model) presented in Boyden and Velinsky (1993) were used to determine

the maximum lateral force exerted on the drive wheels during normal operation. Using these models, the lateral force is a function of the angular velocities and accelerations of each drive wheel. The forward velocity and acceleration above were used to determine approximate maximum angular velocity and acceleration for the wheels. A maximum lateral force of 125 N (28.1 lb) per wheel will be used and will provide conservative results. These calculations are presented in Appendix A. Torque fluctuation results in shear stress fluctuations that were assumed to often reach an in-phase condition with the alternating bending stress so that the maximum of the components could be combined into a maximum stress state. Using this loading condition, calculations shown in Appendix A determined the factor of safety against fatigue failure to be 2.

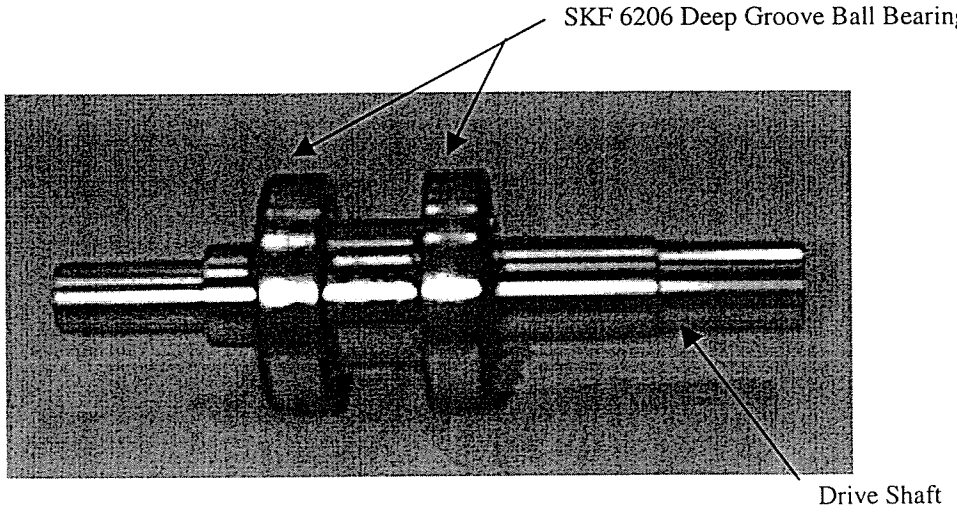

Figure 4.5: Drive Shaft with Bearings Installed

In addition to being sized for infinite life and to prevent yielding under maximum load, the shaft was sized, stepped, chamfered and finished to accommodate necessary and available bearings, seals, and couplings, and to meet torsional stiffness, and length requirements. Additionally, appropriate tolerances were specified to meet recommended bearing, seal, and coupling fits and runout. Design iterations were performed until all reasonable requirements

were satisfied resulting in the shaft shown in Figure 4.5. Final shaft dimensions resulted in a natural frequency of 529 Hz.

4.6.2 Bearing Type Selection and Bearing Sizing

In Chapter 3, a concept of the Drive Train was developed that requires designated bearings to support all external radial and axial loads applied to the Drive Shaft via the wheel. During this concept development it was deemed beneficial to use bearings requiring axial preload so that the drive train friction torque would be adjustable. Deep Groove Ball, Angular Contact Ball, and Tapered Roller bearings are three common bearing types capable of combined axial and radial loading that require axial preload. Because they satisfy the general functional requirements, the specifications of these three bearing types were compared more closely in Table 4.2 and Angular Contact Ball Bearings were selected.

		Bearing Type					
		Deep Groove Ball		Angular Contact Ball		Tapered Roller	
Selection Criteria	Weight	Rating	Weighted Score	Rating	Weighted Score	Rating	Weighted Score
Preloaded axially	20.00%	5	1	5	1	5	1
Combined Loading	30.00%	2	0.6	4	1.2	5	1.5
Cost	5.00%	5	0.25	3	0.15	2	0.1
Mounting design complexity	20.00%	5	1	5	1	3	0.6
Seals	5.00%	5	0.25	0	0	0	0
Shaft locating capability	20.00%	5	1	5	1	5	1
	Total Score		4.1		4.35		4.2
	Rank						
	Continue?		No		Yes		No

Table 4.2: Selection of Bearing Type

Iterating with the shaft design, so that sufficient shaft strength and stiffness and bearing life were achieved, SKF® 7206 BEP Angular Contact Ball Bearings were selected for both the

inner and outer bearings. Arranging these bearings in a face-to-face configuration simplified the Axle geometry and allowed the inner (rotating load) raceway to be press-fit onto the Drive Shaft. The outer raceway fits into the Axle with a transitional-fit allowing axial displacement for preload adjustment. Press–fitting the raceway interfaced with the rotating load prevents wear or fretting corrosion of the shaft and raceway contact surfaces.

Initial calculations using the Anti-Friction Bearing Manufacturers Association (AFBMA) life equation determined that the most heavily loaded (outer) bearing would have an L10 life of 10688 hours operating at a 150 rpm under the maximum loading condition used in the shaft static yield factor of safety calculation. However, later after all parts were designed and machined, these calculations were found to be seriously flawed. The initial calculations placed the radial reactions at the midlines of the bearings instead of at their pressure centers. Because angular contact bearings were oriented in a face-to-face configuration (Figure 4.5), the radial loads acted very near one another. Consequently, tilting moments caused by weight and axial forces resulted in much higher radial and thus axial forces than expected. This greatly reduced the life of the bearings to less than one hour at max load. A more realistic loading condition for fatigue life was considered for this design, but the life was extended only to 64 hours. Additionally, these high radial forces induced extremely high axial forces that caused yielding in the bearing retainer or its bolts at maximum load. Consequently, a fix was required.

Several options were considered to reduce the loads and extend expected bearing L10 life without significant rework of manufactured components. Analysis deemed that the best options were replacing the Angular Contact bearings with Deep Groove Ball bearings, or moving the Angular Contact Bearings closer together. Deep Groove Ball bearings have a smaller contact angle than Angular Contact Bearings; accordingly, their axial load carrying capability is smaller.

However, because they have a smaller contact angle, their pressure centers are closer to the bearing midlines. Therefore, when oriented in a face-to-face configuration the pressure centers and the radial reactions are much further apart than when Angular Contact Ball bearings are used. Consequently, the radial reactions resulting from tilting moments are much smaller. Deep Groove Ball bearings are available in the exact same dimensions as the SKF® 7206 BEP; therefore, they can be directly substituted. On the other hand, if the Angular Contact Bearings are closer to each other, their pressure centers change sides and separate. Placing the bearings close to one another separates the pressure centers sufficiently to greatly reduce radial loads resulting from tilting moments. However, moving the Angular Contact bearings closer together requires machining the shaft and machining a collar to place behind the inner bearing. Although the axial load carrying capability of the Deep Groove Ball bearings is less than that of Angular Contact Ball bearings as indicated in Table 4.2, analysis determined that their life will be sufficient and longer than the Angular Contact bearings moved closer together. Therefore, the bearings were replaced with SKF® 6206 Deep Groove Ball bearings.

Two sets of final life calculations performed for the SKF® 6206 bearings are shown in Appendix A. Utilizing the AFBMA Life theory, these calculations found the expected L10 life of the most heavily loaded bearing to be 1847 hours under the maximum load used in shaft yield analysis, and 174,000 hours under the loading condition used to predict shaft fatigue strength. Either of these life spans is acceptable for this software validation test bed; however, the latter better represents normal operation and obviously provides a large buffer against failure.

4.7 Design of Axle

A stationary Axle made of 6061-T651 AL bolts to the Coupling Housing and supports the outer raceways of the Deep Groove Ball bearings. This Axle transmits the external radial and axial loads from the bearings to the Frame. The dimensions of the Axle were dictated by the geometry of the wheels of the press-on and pneumatic tires, the Drive Shaft, the Bearings, and the Coupling Housing. A few key features of the Axle, shown in Figure 4.6, are worth mentioning. A female alignment pilot machined coaxial to the bearing bore within close tolerance, mates with the male alignment boss on the Coupling Housing to ensure coaxiality of the gearhead output shaft and the Drive Shaft. 7.94 mm (5/16 in)-18 Socket Head Cap screws are used to fasten the Axle to the Coupling Housing, counterbores ensure flush contact between the bolt heads and Axle. A smaller bore behind the bearing bore is sized so that the seal presses into it. A bearing retainer is used to constrain the bearings axially and apply preload. To adjust preload, shims are placed between the bearing retainer and the to the outer face of the axle. Four 10-24 X 15.9 mm (5/8 in) long Socket Head Cap screws thread into four tapped blind holes to fasten the retainer to the Axle. For added strength and durability, these threads are lined with stainless steel HeliCoil® thread inserts. Tolerances were specified to ensure proper bearing raceway and seal fits, square bearing abutments, and minimal angular shaft misalignment. Stress analysis shown in Appendix A determined the factor of safety against yield for the Axle is 37. The factor of safety for the 10-24 bolts is 1.5 under maximum load. For the Axle, strain is more critical than stress because deflections result in additional bearing and shaft stresses. However, the Von Mises stress within the axle is small and 6061-T651 AL obeys Hooke's Law so the

deflections will also be small. From this it was concluded that deflection analysis was not necessary.

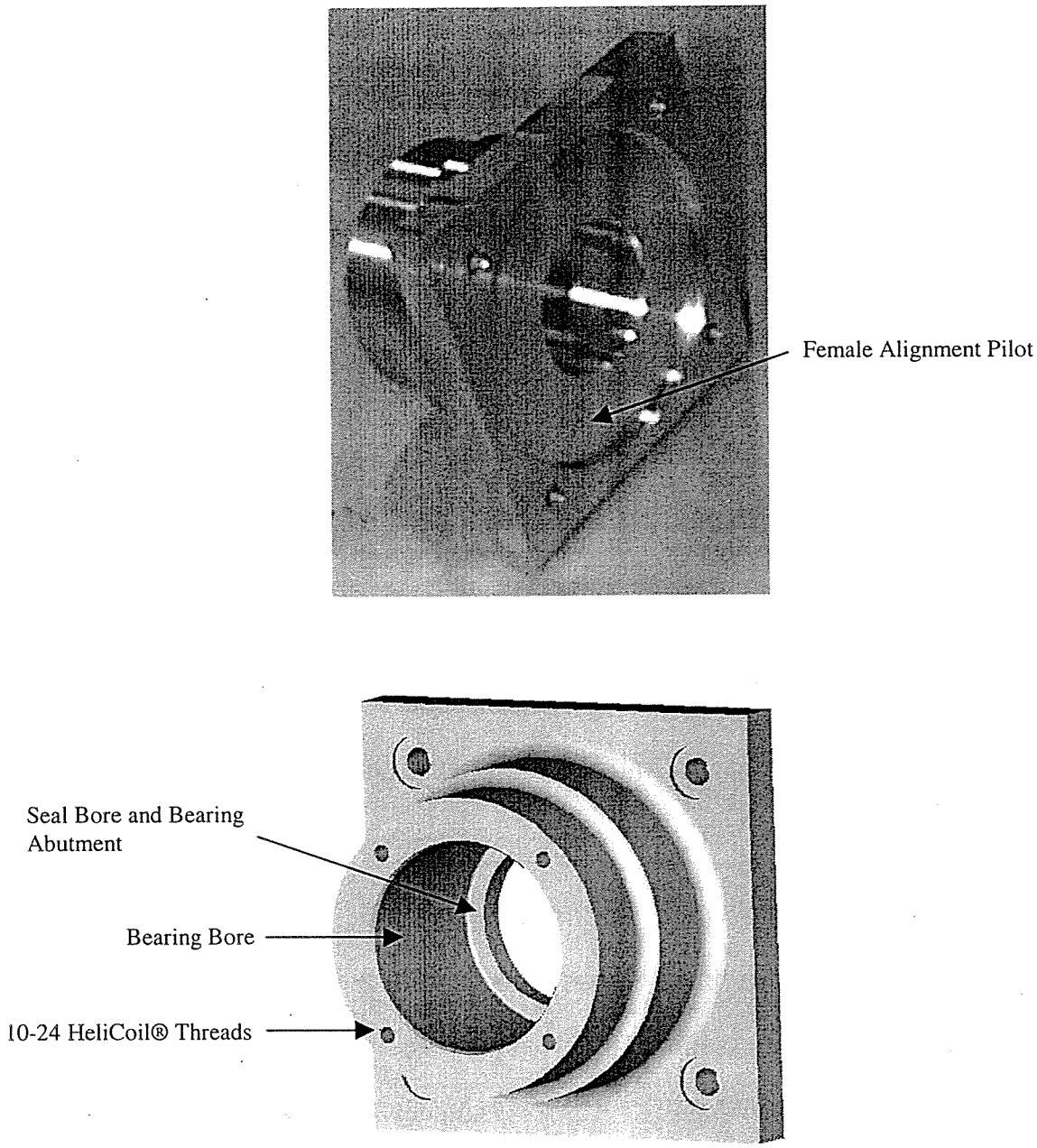

Figure 4.6: Front and Rear View of Axle

4.7.1 Bearing Retainer Design and Shim Selection

A bearing retainer, shown in Figure 4.7, was designed to constrain the cross located bearing pair and apply axial preload to the bearings. In addition to constraining and preloading the bearings, the bearing retainer also houses the outer lip seal. Tolerances were specified for the parallelism of the bearing abutment and shim surfaces to ensure even preload on the outer bearing raceway. Under the maximum loading condition used for the Drive Shaft yield analysis, the bearing retainer supports the maximum axial load. Assuming the axial load is distributed equally to each of the four bolts, the shear stress of the material clamped by the bolt heads was calculated. Using 6061-T651 Aluminum provides a factor of safety against yield of 47.

Shim Stock is available in several materials including plastic, stainless steel, mild steel, spring steel, brass, aluminum, copper, and monel, and Nickel. Shims for the Axle Assembly were made of plastic Shim Stock. Plastic Shim Stock is relatively easy to cut to the desired dimension, which was ideal for this case where only a few shims are needed. Additionally, plastic Shim Stock is available in smaller sheets than many of the other materials, which makes it less expensive. Plastic Shim Stock is minimally compressible, thus it performs well in bearing preload applications. Shims of various thicknesses were used in the shim packs, and Chapter 5 contains a chart relating shim color and thickness. The bearing preload, and thus the drive train friction torque can be adjusted somewhat by adjusting the thickness of the shim pack. However, exceedingly under or overloading the bearings will reduce their life.

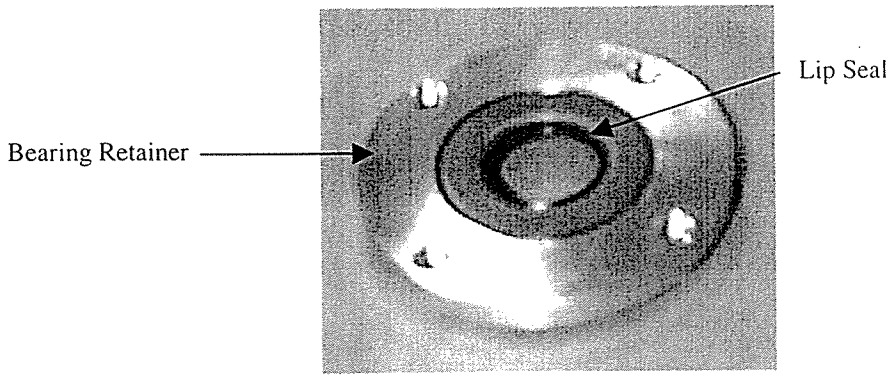

Figure 4.7: Bearing Retainer with Seal Installed

4.7.2 Seal Selection

Seals were used both at the inside and outside of the Axle to keep contaminants out of the bearing and retain grease within the bearings. Seals are available in a variety of styles, materials, and sizes for various applications and lubricant types. For grease lubricated, low to medium speed applications, Nitrile Lip Seals are a common low cost effective solution. Seal sizes were determined by examining the dimensional requirements of the Drive Shaft, Axle, and Bearing Retainer and iterating to satisfy the requirements of all three components with a stock Nitrile Lip Seal. One-piece National Oil Seal #471762 seals were selected for both the inner and outer locations.

4.7.3 Wheel Flange Design and Trantorque® Selection

In Chapter 3, Press-on and Pneumatic tires and their corresponding wheels were selected to propel the platform. Both sets of wheels easily mount to flanges with threaded bolts or studs; however, they have significantly different dimensions. Therefore, to accommodate dimensional differences, separate flanges were designed to mount each type of wheel to the Drive Shaft. Trantorque® keyless bushings were selected as a uniform, durable, and simple method for

mounting both flanges to the Drive Shaft. Keyless bushings produce a mechanical interference fit, and here they provide backlash-free coupling of the Drive Shaft and wheel-mounting flange, as shown in Figure 4.8. Additionally, keyless bushings do not require keyways or cuts in the shaft, which results in the strongest possible shaft for a specific size and material. Several keyless bushings are available; however, Trantorque® bushings are more compact and easier to install. These bushings use a single nut to interlock the bushing components and are self aligning whereas others use multiple bolts and caution must be taken to prevent cocking during assembly.

A Standard Series 6202160 Trantorque® with a 19.0 mm (0.75 in) inside diameter and 38.1 mm (1.5 in) outside diameter was selected. This bushing is capable of transmitting 282.5 N-m (2500 lb-in) of torque yielding a factor of safety of 4, and 19571.2 N (4400 lb) of axial force providing a factor of safety of 17. Additionally, these dimensions enabled the flanges to be designed to withstand the internal radial pressure placed on their inner bore by the bushing. Furthermore, a 19.0 mm (0.75 in) shaft diameter (in this section of the shaft) met the shaft natural frequency and strength requirements.

Wheel-mounting flange dimensions were selected to fit the wheels, to ensure sufficient strength, and so that the track width of the platform is identical for both sets of tires (i.e. the midlines of the Press-on and Pneumatic tires are located equidistant from the platform centerline). Trantorque® bushings place high radial pressure on the internal bore of the flange resulting in significant stress within the flange. This stress is a function of the Internal Diameter (ID), Outside Diameter (OD) and width of the flange. The ID and OD are constrained by the Trantorque® and wheel dimensions respectively. Because the wheel of the Pneumatic tire is smaller in diameter than the wheel of the Press-on tire, the OD of the flange for the Pneumatic tire is also smaller than for the Press-on tire. Stress calculations due to radial pressure were

performed for the Pneumatic tire flange using equations provided by the Trantorque® manufacturer. Using 6061-T651 Al, the minimum factor of safety against yield is 1.9.

Each flange is drilled with a hole pattern matching its respective wheel, and threaded studs are pressed into them for attaching the wheels (Figure 4.8). Automotive studs and conical lug nuts fasten the Press-on tire. The conical lug nuts prevent slippage between the wheel and flange. The studs fastening the pneumatic tire came with the tire. Also, Pilots that support the wheel and ensure coaxiality of the wheel and Drive Shaft are machined into both flanges.

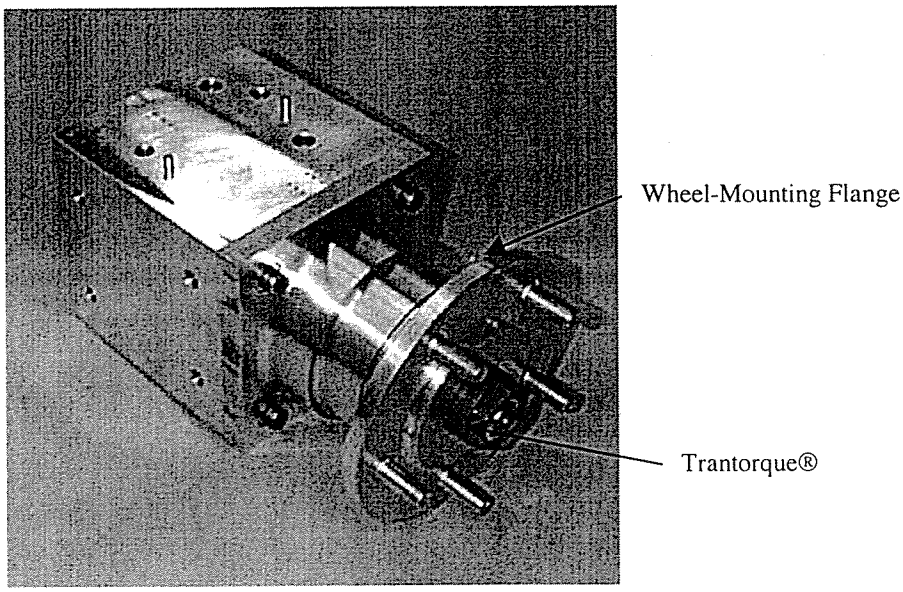

Figure 4.8: Wheel-Mounting Flange and Trantorque

4.8 Frame Design

In Chapter 3, a tubular frame concept was selected. Detailed frame design, discussed here, resulted in the aluminum rectangular tube frame shown in Figure 4.9 with two Main Rails, three Cross Members joining the Main Rails, a plate that ensures coaxial drive wheels and supports the manipulator, and a mount for the casters. The Main Rails and Cross Members are

manufactured from stock aluminum tubing. A steel sheet metal enclosure houses the power electronics, and miscellaneous brackets hold the Zebra Power Supply and the Industrial Chassis computer. Joining the Cross Members and Main Rails with well designed bolted joints resulted in a square, true, and rigid frame. Additionally, this design allowed separate components to be concurrently designed and manufactured which expedited the design and manufacturing process.

Selection of the frame geometry was discussed during concept selection. Specific frame dimensions were dictated primarily by the space needed for the electrical components, the Drive Train, and the ZEBRA manipulator. A wood prototype of the power electronics enclosure was used to layout electrical components and determine their space requirements. The Frame is approximately 89 cm (35 in) wide and 145 cm (57 in) long, and the overall ARMMACS footprint, including tires is approximately 119 cm (47 in) wide.

The ARMMACS robot is a test bed that will be used to validate control algorithms and dynamic models. Verifying the accuracy of the dynamic models and the robustness of the control algorithms may require testing under various loading conditions. For this reason, the Product Design Specifications (PDS) state that the platform should withstand a total weight, including ballast, of 2220 N (500 lb). However, the ballast distribution is unknown. Using the maximum expected load state presented during Drive Shaft yield analysis for the frame design ensures the Frame is sufficiently strong and stiff for all anticipated operations. The distribution of the total weight, including ballast, was assumed to be the same as the distribution of the no-ballast Chassis weight. To determine the distribution of the no-ballast Chassis weight, a frame configuration was assumed, and the weight and its distribution were estimated. As shown in Appendix A, the estimated total weight of the robot including the manipulator was 1546N (348 lb) with 70% of the weight distributed equally to the drive wheels and 30% distributed equally to

the casters. Distributing the total weight of 2220 N (500 lb) results in maximum normal forces of 778 N (175 lb) per Drive Wheel and 334 N (75 lb) per caster. In addition to the normal forces, the lateral and radial forces applied to the Drive Wheels are also transmitted to the Frame. A maximum lateral force of 1110 N (250 lb), and maximum propulsive (longitudinal) force of 547 N (123 lb) per wheel were used.

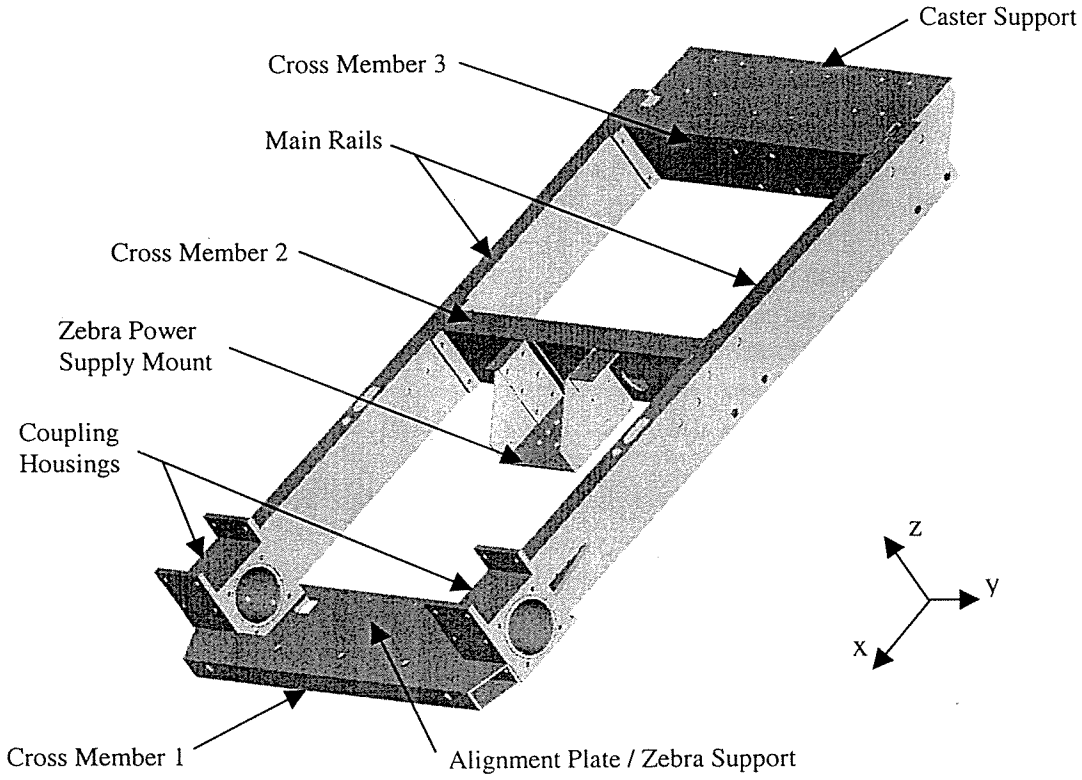

Figure 4.9: ARMMACS Frame Components

4.9 Main Rail and Cross Member Material Selection

To satisfy the Product Design Specification requirement that all ARMMACS components be made of stock materials, the tubing material and sizes were selected from available stock. Metallic materials were preferred for this application because they shield electrical fields. Steel and aluminum are the most readily available and least expensive metals with reasonable strength-

to-weight and stiffness-to-weight ratios; therefore, only these materials were considered for structure members of the Frame. The motors, gearheads, and electrical components available for ARMMACS were purchased early in the conceptual design process, before the Zebra manipulator was selected, and are heavy relative to the manipulator. Therefore, the platform must be lightweight to approach the desired platform-to manipulator weight ratio. During operation, the frame members are subject to weight force in the vertical plane, and dynamic forces in the horizontal plane, resulting primarily in normal stresses due to bending and bending deflections. Therefore, the yield strength and bending stiffness were analyzed for steel and aluminum sections of equal weight per unit length to determine which material endures the highest bending moment and deflects least. This analysis, included in Appendix A, shows the stiffness, K of a steel tubing section is slightly higher than an aluminum section

($(K_{eq})_{ST} = 1.04\ (K_{eq})_{AL}$). However, for sections of equivalent weight, the walls of steel tubing are approximately one-third the thickness of aluminum tubing walls. Consequently, modeling the tubing walls as flat plates using the Von Karmon Theory shows that the flexural rigidity, D of steel tubing walls is much lower than aluminum tubing walls ($D_{AL} = 9.3D_{ST}$). Additionally, because the cross-section area moment of inertia of the steel section is much less than the aluminum section, the maximum allowable moment, M_{ALL} that can be applied to the steel section is significantly lower than the moment that can be applied to the aluminum section $(M_{ALL})_{AL} = 1.5(M_{ALL})_{ST}$.

To firmly join thin walled tubing with flanges and bolted joints, either only one wall can be clamped, or spacers must be installed in the clamped tube to prevent collapsing of the walls and ensure sufficient bolt preload. Therefore, it is easiest to join thin walled tubing by bolting to a single wall. In this case, the flexural rigidity of the tubing walls is crucial to ensuring stiff

joints. Since the Main Rails and Cross Members are joined with bolted joints, high flexural rigidity of the tubing walls is key to a simple and stiff joint design and thus to a stiff Frame. Additionally, either aluminum or steel sections have adequate bending stiffness. Thus the slightly higher bending stiffness of a steel section does not warrant the significant sacrifice to joint stiffness incurred with the use of a steel section. Furthermore, since the aluminum section can withstand a higher bending moment, aluminum structural members will provide a more versatile Frame. From this analysis, 6063-T52 Aluminum tubing was selected as the material for the Main Rails and Cross Members. 6063-T52 is common for structural aluminum sections and is weldable so flanges can be easily attached. Aluminum tubing will not shield magnetic field; however, it will dissipate electric field emitted from the cables.

Main Rail Design

Two Main Rails constructed of 50.8 X 127 X 3.18 mm (2 X 5 X .125 in) 6063-T52 aluminum tubing run the length of the Frame. This tubing size was selected primarily for geometric reasons; however, it also provides a stiff and lightweight structure. The 127mm (5 in) height dimension is very robust in strength, but works well for mounting many of the available electrical components within the confinement of the Frame. Using a larger tube also enabled several control and power cables to be routed through the rails for protection and electromagnetic field shielding. Furthermore, because the strength is high, deflections are minimal which is important for precise relative locations of position sensors and the Zebra manipulator.

For maximum load state, the forces applied to the Main Rails in the vertical and horizontal planes are of similar magnitude. However, the unsupported span is over two times longer in the vertical plane so the tube is oriented with the larger dimension in the vertical plane. Simplified and conservative analyses were performed to approximate the normal stress due to

bending and the deflection of the Main Rails. In the vertical plane running the length of the rails, these analyses model the Main Rails as simply supported beam subjected to ½ the maximum weight force concentrated at the Center of Gravity location. In the horizontal plane, they are modeled as fixed-fixed beams because they are clamped at each end by the Cross Member flanges. A maximum force due to lateral acceleration is applied at the Center of Gravity location and distributed equally to each main rail. These analyses give a minimum factor of safety against yield of 19. From the calculations, the maximum deflection in the vertical plane is 0.13 mm (0.005 in), and the maximum deflection in the horizontal plane is 0.22 mm (0.009 in). Because conservative analysis resulted in large factors of safety and small deflections, more detailed analysis was deemed unnecessary.

Flanges are welded to the front end of each Main Rail. Bolts pass through these flanges and attach the Coupling Housings to the rails. The longitudinal propulsive forces applied at the ground/tire interface produce a moment about the vertical (z-axis) as well as a force in the longitudinal (x-axis). This force/moment couple, lateral forces, and weight forces are transmitted through the welds that join the flanges to the Main Rails. To strengthen and stiffen these joints, triangular gussets are welded at the intersections of the tubing and flanges, see Figure 4.10. Because the walls are thin, stiffeners are located inside the tubes and plug welded to both tubing walls to join the walls in the region of the gussets. This way forces transmitted through the gussets are distributed to both walls.

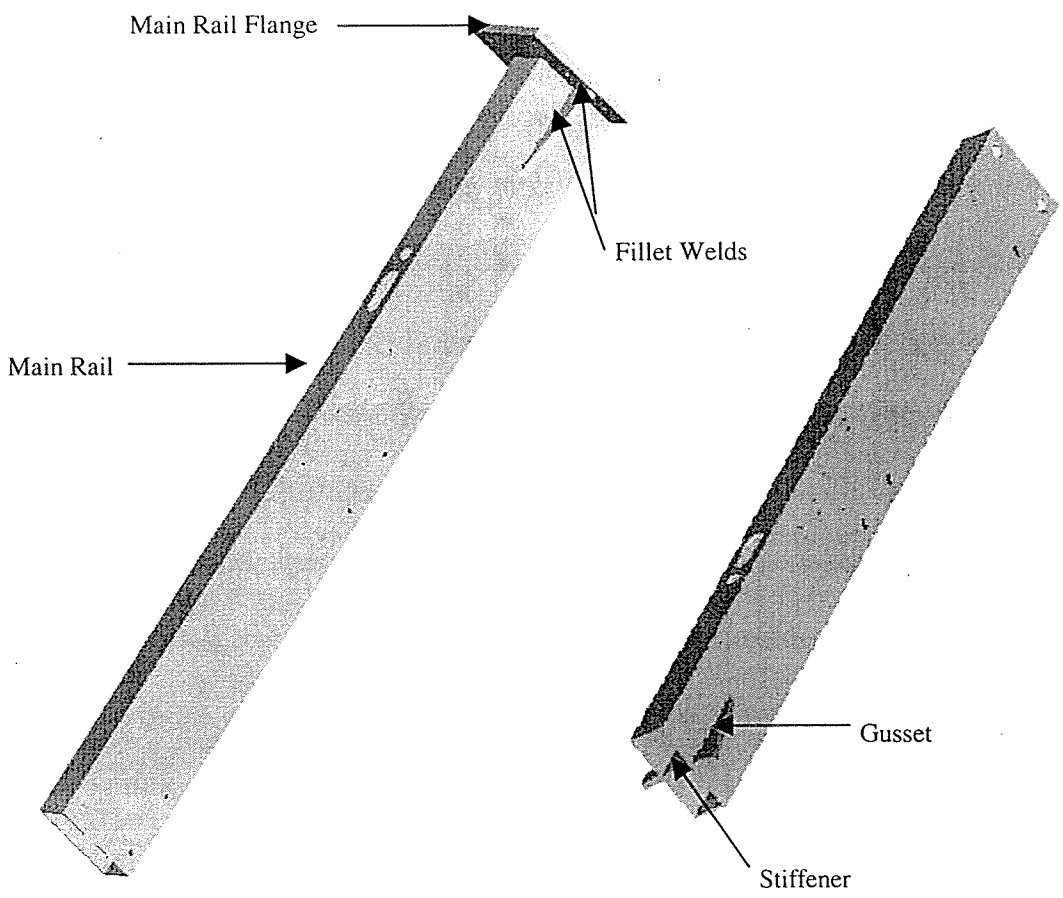

Figure 4.10: Mail Rail Stiffener and Flange

4.9.1 Cross Member Design

Two Cross Members constructed of 50.8 X 127 X 3.18 mm (2 X 5 X .125 in) 6063-T52 aluminum tubing and a third made of 44.5 X 76.2 X 3.2 mm (1.75 X 3 X .125 in) 6063-T52 aluminum tubing span the width of the Frame and join the right and left Main Rails. The two 50.8 X 127 X 3.18 mm (2 X 5 X .125 in) Cross Members, titled Cross Members 2 & 3 on their prints, have flanges welded at each end and they bolt directly to the inner wall of both Main Rails. Plates are placed inside the Main Rails at the joints to distribute forces over a larger area of their walls and reduce localized stresses under the bolt heads. Cross Member 2 is machined

with several features to hold connectors for power and control cabling. The 44.5 X 76.2 X 3.2 mm (1.75 X 3 X .125 in) Cross Member, titled Cross Member 1 and shown in Figure 4.11, is smaller to provide clearance for the manipulator. Flanges welded to each end of Cross Member 1 bolt to the front surface of the Coupling Housings. By attaching this Cross Member directly to the Coupling Housings, moments applied to the coupling housing are distributed to the Cross Member and the adjacent Main Rail. Equally important, this Cross Member passes in front of the manipulator protecting it from frontal collisions and stiffening the manipulator mount surface.

Several external forces act on all three Cross Members in both xz and zy planes (refer to Figure 4.9 for reference frame). To show the robust strength and stiffness of the cross members, simplified conservative analyses were performed modeling the cross members as fixed–fixed beams in the yz plane and as cantilevers in the xy plane. These calculations assume the Main Rails are rigid. For the yz plane, the maximum load state applies the entire platform weight centrally to Cross Member 2. With these loads and boundary conditions, the factor of safety against yield is 30, and the maximum deflection in the z direction is 0.03 mm (0.001 in). For the xz plane, the maximum transmittable torque is applied to one Drive Wheel, and the other Drive Wheel and corresponding Main Rail are fully constrained. The longitudinal force applied to the free Main Rail is distributed equally to each Cross Member. Under these boundary conditions and loads, the factor of safety against yield is 26, and the maximum deflection in the x direction is 0.61 mm (0.024 in). These analyses are simplified; however, because they are conservative and show large factors of safety and small deflections, more accurate analysis is not necessary.

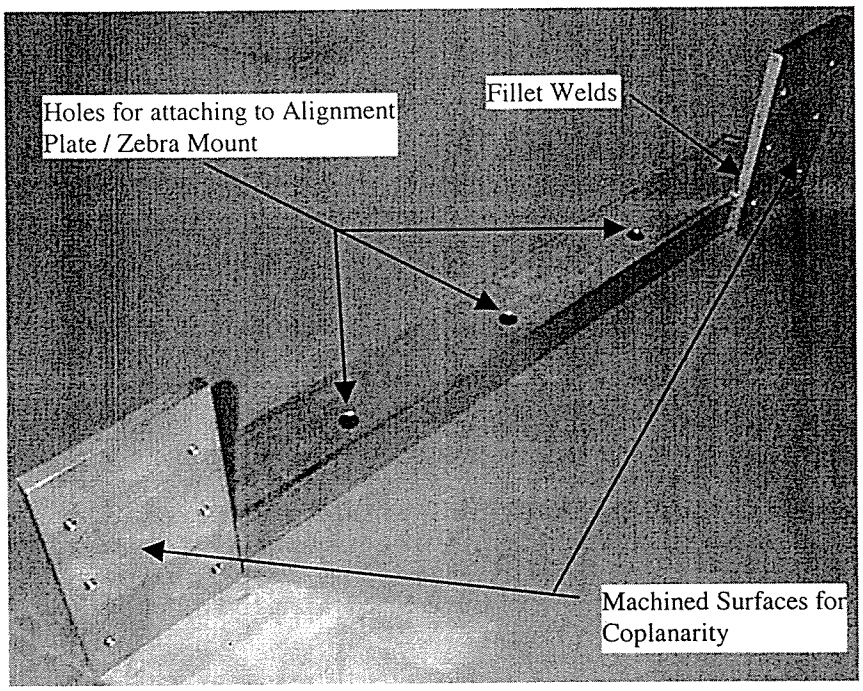

Figure 4.11: Cross Member 1

4.9.2 Flange Attachment

Flanges were attached to the tubes using standard fillet welds when clearance was available. However , because the Electrical Box fits flush against one side of the tubes and flanges of Cross Members 2 & 3, the welds were kept flush with the tube wall. This was done by welding a 4.76 mm (0.188 in) thick backing plate to the inner wall of the tube where the weld was to be placed, notching the tubing wall to provide space for the weld, welding to the backing within the notch and machining the welds flat. A key feature of all flanges are the 1.59 mm (0.063 in) deep slots that locate them precisely on the tubes to ensure that flange holes align with their counterparts. One important aspect of the fabrication is that all critical faces of all flanges where machined to specification after welding. This ensures a true, planar Frame with correct perpendicularity and dimensions. All flanges are thicker than strength requirements dictate to reduce welding warpage and to increase the stiffness of the joints.

4.9.3 Alignment Plate / Zebra Mount

Because the Frame consists of several members bolted together, tolerance stack-ups could easily result in misaligned drive axles and a poorly located manipulator. Therefore, the Coupling Housings are precisely located with Dowel Pins on a common plate to ensure coaxial Drive Shafts, see Figure 4.12. Likewise, because the location of the manipulator with respect to the Drive Wheels is important, the manipulator is also attached to this plate.

Since the Zebra manipulator is attached to this plate it must be stiff to prevent resonant excitation of the assembly. This is important because vibration of the end-effector force sensor results in noisy signals. An Aluminum beam with rectangular cross section subject to a point load is approximately 8.4 times stiffer than a steel section of equal weight if only the thickness can be varied; therefore, this plate is made of 6061-T651 aluminum. By securely fastening the mid span of the Alignment Plate / Zebra Mount to the front cross member at its front edge, and to the Zebra Platform of the Zebra Mount at its rear edge, the stiffness of the Zebra mount surface is increased vastly. When the weight of the Zebra Manipulator and the Zebra Mount, 186.8 N (42 lb), is applied to this plate, the front portion of the plate will deflect less than 0.03 mm (0.001 in) and the rear portion will deflect less than 0.4 mm (0.016 in). If the plate deformation is linear from front to rear, the deflection at the J1 axis of the manipulator will be less than 0.2 mm (0.009 in).

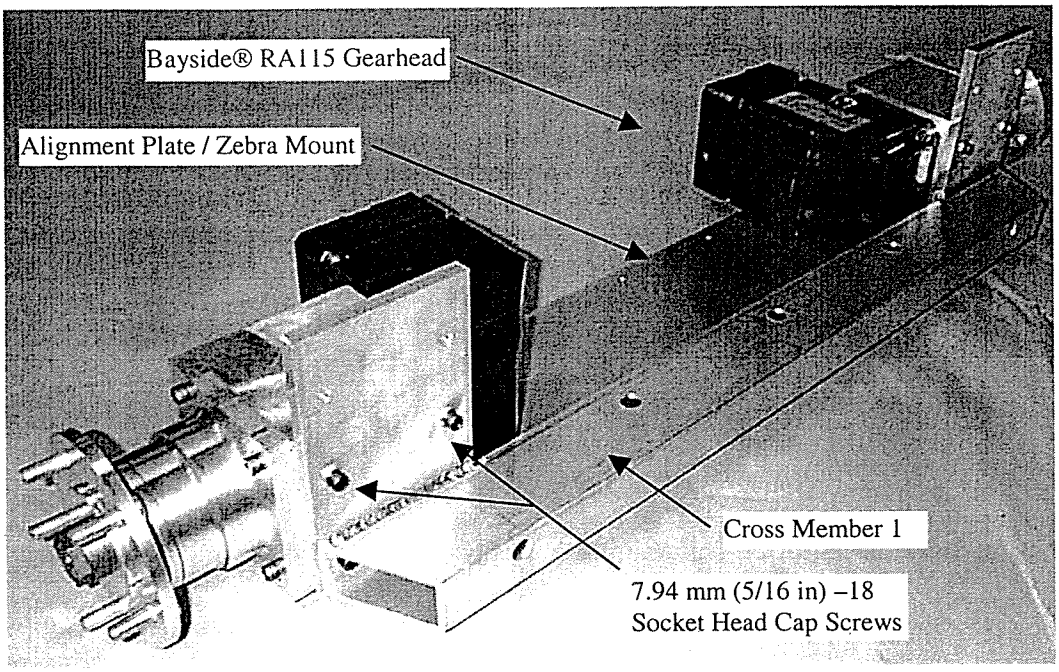

Figure 4.12: Alignment Plate / Zebra Mount with Drive Train Attached

4.10 Zebra Mount

Chapter 2 concludes that the Zebra ZERO manipulator and its Homing Nest should be mounted to a single portable mount. The mount shown in Figure 4.13 attaches to the Frame and locates the manipulator either between the Drive Wheels or outboard of either Drive Wheel. High Stiffness and low weight are the key characteristics of this mount. When located between the wheels the Zebra Platform (refer to Figure 4.13) is bolted directly to the Alignment Plate / Zebra Mount component of the Frame, and the vibration of the Zebra Base is dependent on the stiffness of the Alignment Plate / Zebra Mount and its supports. On the other hand, when the Zebra is located outboard a wheel, it is attached to the platform from the Upper Mount of the Zebra Mount, thus the Zebra mount is stiff to prevent vibratory excitation or large deflections of the Zebra Base. A stiff and lightweight structure was achieved using tubes and channel sections to reach outboard of the tire. Tubes and channels provide high area moments of inertia and thus

high flexural rigidity with minimal weight. All components are aluminum because it provides the greatest strength-to-weight and wall stiffness-to-weight ratios for the sections used. Furthermore, some components are design purely for specific geometry, in which case aluminum components are approximately one-third the weight of steel components.

When the Zebra manipulator is located outboard the wheel, longitudinal platform acceleration will result in longitudinal force applied to the Center of Gravity of the manipulator. Since the Channels cantilever from the support tubes, this force will result in some bending deflection of the Channels and torsional deflection of the tubes. The Lateral Stiffener prevents torsional deflection and relative displacement of the tubes. Additionally, it stiffens the Channels and ties together the tubes, the channels, and the Zebra Platform to minimize relative displacements of these components. Joining the tubes with two Cross Members at the Upper Mount Assembly also adds stiffness to the structure. These Cross Members form a Frame that resists relative displacements of the left and right tubes that could propagate into large deflections of the Zebra platform.

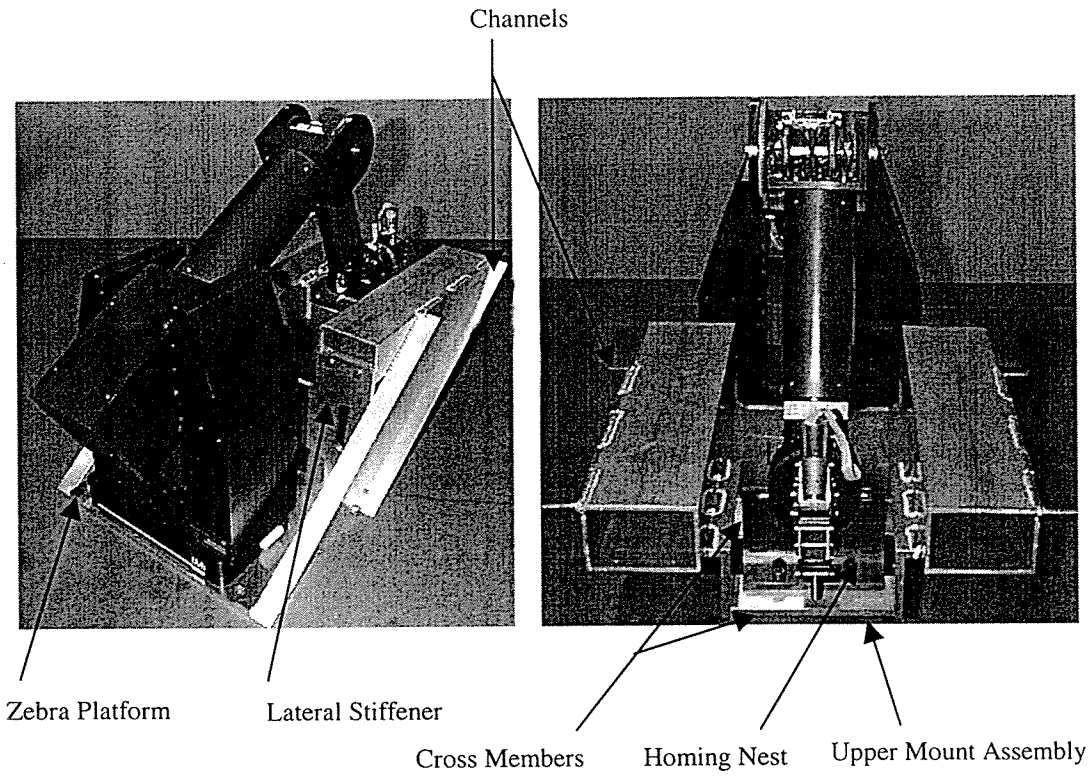

Figure 4.13: Zebra Mount with Manipulator Attached

The Zebra mount was designed and manufactured to tight tolerances to ensure the J1 axis of the Zebra (Figure 2.3) is located on the Drive Wheel axis and that the base is mounted at the designed height. This was achieved in manufacturing by welding subassemblies first and then drilling and machining features to tight tolerances with respect to appropriate assembly surfaces. The Lateral Stiffener also assists in precisely locating the Zebra Platform.

4.11 Design of Other Chassis Components

4.11.1 Electrical Box

A steel sheet metal electrical box, part of which is shown in Figure 4.14, was designed to house all relays, fuses, power electronics wiring, and the termination of the remote pendant

wiring. Steel was used because ferrous metals dissipate and contain electrical and magnetic fields that may otherwise degrade signals from sensitive encoders and sensors. All electrical components were mounted to an aluminum sheet designed to fit inside the box. This enabled concurrent component layout and electrical box design and fabrication with minimum weight increase. Mounting the servo drives and AC line filters to opposite sides of the electrical box doors minimized the length of power cable between them and the length outside the enclosure, a precaution taken to minimize unshielded electromagnetic fields. Grommets and Liquid Tight Cord Connectors are used where cables pass though the electrical box or the frame members to prevent potentially dangerous wear to cable shields.

The enclosure was made of 18 Gauge Zinc plated steel. Zinc plated material was used to prevent corrosion and contamination of the electronic components. 18 Gauge is lightweight material; therefore, appropriate breaks were located to stiffen the structure. Breaks along the top edges of all four walls of the pan add stiffness along the lengths of the walls. This is especially important for the walls that the door hinges are attached to. Placing breaks along both the width and the length of the doors gave them the strength necessary to support the drives and filters. The ledge and door stop were stiffened by geometry required for their respective functions. Standard slam latches are implemented to securely fasten the doors closed so that the motor drives are mounted to a firm base. The doors are attached to the pan with continuous hinges that are drilled with a staggered hole pattern for solid mounting.

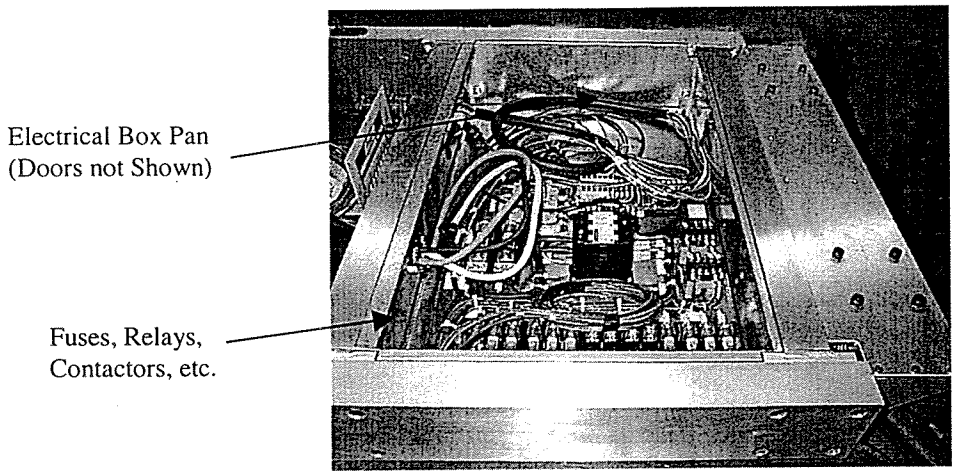

Figure 4.14: Power Electronics in Enclosure Pan and Mounted to Frame

4.11.2 Zebra Power Supply Mount

The Zebra manipulator uses a power supply to transform voltage from 208AC to 24V DC. This power supply weighs 107N (24 lb) and is attached to the Frame by the Zebra Power Supply Mount. Cantilevered from Cross member 2, this mount is designed to support the power supply load and a portion of the Industrial Chassis computer. A tray (bottom tray) passes under the power supply and extends just beyond the power supply Center of Gravity to provide ample support while inhibiting natural convection as little as possible. Several 12.7 mm (0.5 in) holes in the bottom tray provide an inlet for cooler air to enable natural convection in the region of the mount. Mounting the Industrial Chassis computer to the Frame with Rubber Stud Bumpers provides some shock protection for the computer.

4.11.3 Caster Mount

Shock-Absorbing Swivel Casters support the rear of the ARMMACS platform. As shown in Figure 4.15, these casters bolt to a Caster Mount plate that is supported by the Caster

Support plates at each end. The factor of safety against yield of the Caster Mount is 6.5 under maximum load. In addition to supporting the Caster Mount, the Caster Supports also distribute the forces at the joints between Cross Member 3 and the Main Rails to a larger area of the Main Rail walls. Since the Caster Support plates are cantilevered, the moment acting on them is highest at the root and the cross section is largest at the root and tapered to reduce weight. Under the maximum load the Caster Support plates have a factor of safety against yield of 290.

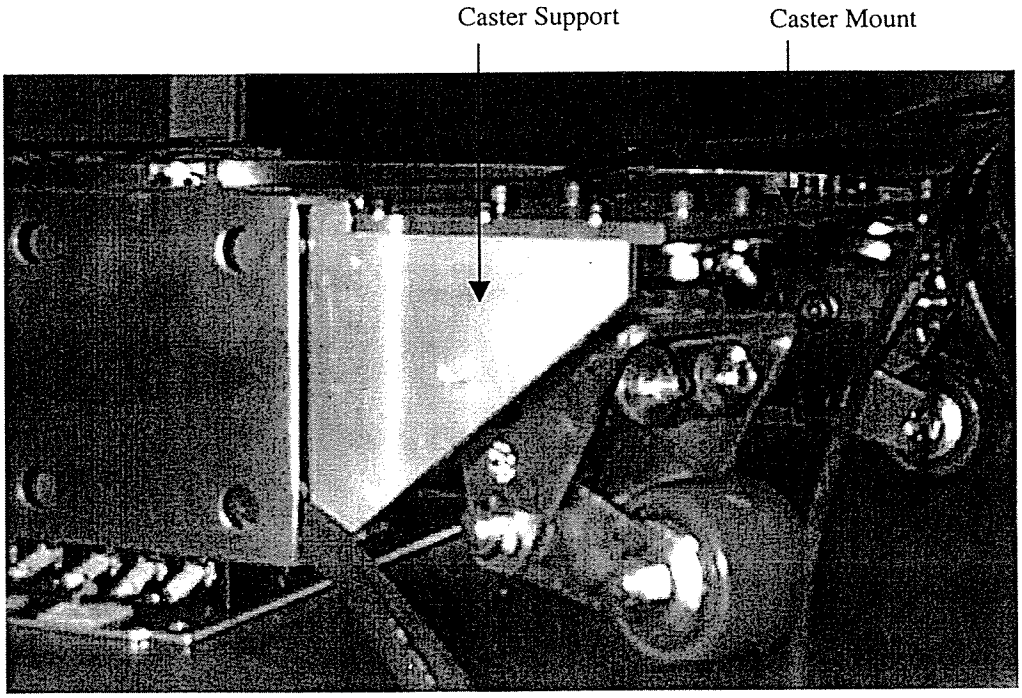

Figure 4.15: Caster Mount and Casters

4.12 Summary

This chapter presented the detailed mechanical design or the selection of each component forming the ARMMACS robot. A natural division exists within the chapter, separating it into

discussions of the Drive Train and the Frame. A common maximum load state used for yield and deflection analysis of Drive Train and Frame components was stated, and a separate load state better representing ordinary operating conditions was discussed. The latter load state was used to analyze the fatigue strength (or life) of drive train components. Results of stress, life, and deflection analysis of various parts were presented as appropriate. Additionally, significant features and fabrication methods of each component were discussed.

Chapter 5

Technical Specifications

5.1 Introduction

The ARMMACS is an assemblage of components. For this reason, engineering the ARMMACS required tentative assumptions of final product characteristics to parameterize specific constituents of the system. Significant assumptions were the robots weight and weight distribution, because they dictated the design loads for several components. Accordingly, the integrity of these components and of the entire system depends on the validity of the values used. Therefore, after fabricating the ARMMACS, measurements were taken to determine the accuracy of the estimated values. This chapter presents the measured weight and the weight distribution of the physical system and compares them to corresponding values used for design.

Furthermore, formulating accurate dynamic models also requires accurate knowledge of the weight and weight distribution of the ARMMACS. Similarly, dynamic models require several dimensions and the rotational inertia of the platform. Determining assembly dimensions from detailed prints is tedious; therefore, foreseeable required dimensions are summarized in this chapter. Additionally, because most of the components on ARMMACS have awkward shapes and non-constant mass distribution, accurate calculation of the rotational inertia is cumbersome. For ARMMACS, measurements will provide more accurate and expedient inertia data; consequently, a discussion of the inertia measurement is presented.

5.2 Validation of Assumed Weight and Weight Distribution

5.2.1 Weight Data

Weight measurements were taken using electronic floor scales with 2.2 N (0.5 lb) accuracy. The vehicle was weighed at a single point at the rear and at each Drive Wheel as shown in Figure 5.1, summing moments revealed the x and y Center of Gravity (CG) locations with respect to Reference Frame 1 in Figure 5.1. Additionally, the total weight at the Drive Wheels was measured with the rear lifted to several elevations, then moments were taken about point A in Figure 5.2 to determine the CG location in the z direction. These data points are plotted in Figure 5.3 and their average value is given in Table 5.2. The raw data and detailed calculations for x,y, and z locations are given in Appendix A.

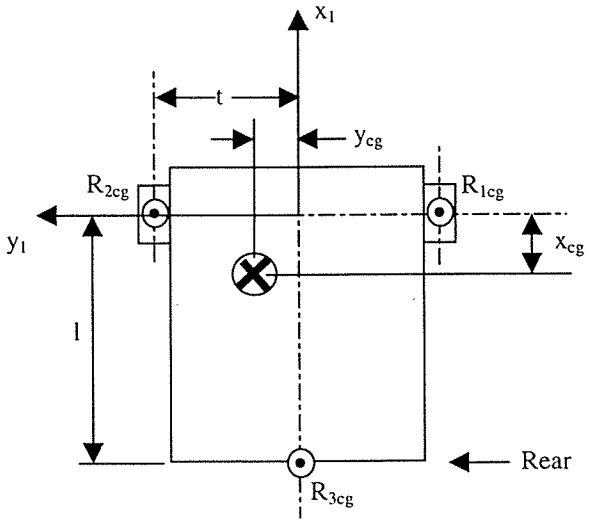

Measurements: R_{1cg}, R_{1cg}, and R_{1cg}

Figure 5.1: FBD for x & y cg Location Calculation

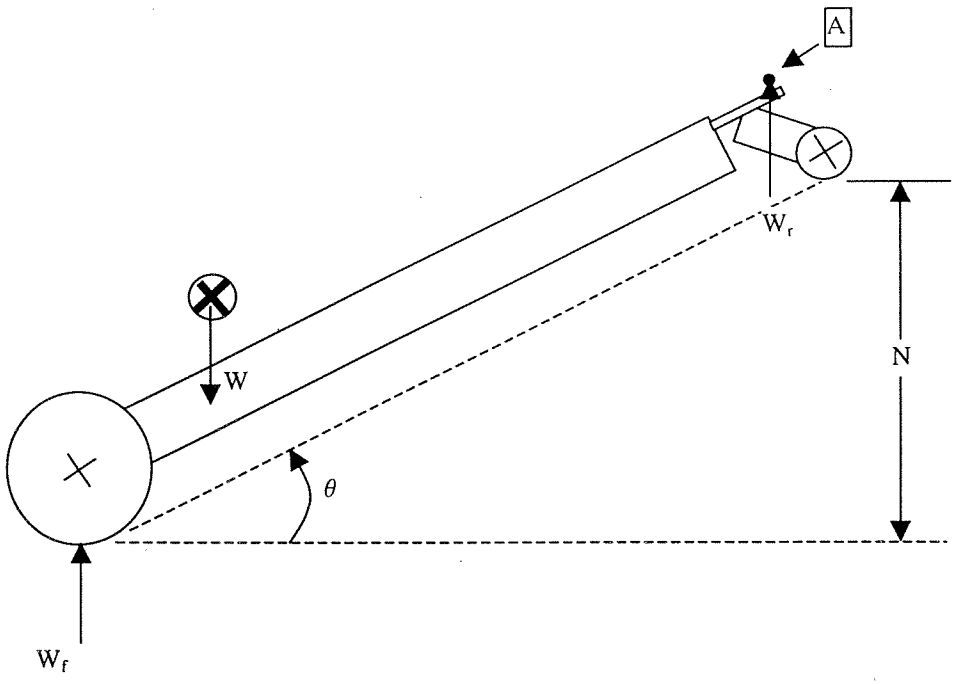

Figure 5.2: FBD for z cg Location Calculation

Weight measurements were collected for the following scenarios:

1. Complete ARMMACS robot:
   - Manipulator installed at the platform midline location with the end effector resting in the Homing Nest
   - Press-on tires installed (111 N (25 lb) each)
   - Temporary Cable Tower installed
   - Integrated Motions Inc. (IMI) computer supplied with Zebra ZERO manipulator installed
   - Tethered cables suspended from ceiling such that only the cable tied to the robot was being weighed
2. Platform without the manipulator
   - Same case as scenario 1, but without the manipulator

Table 5.1 displays the weights of the robot and manipulator, and Table 5.2 gives the CG location of the robot with and without the manipulator.

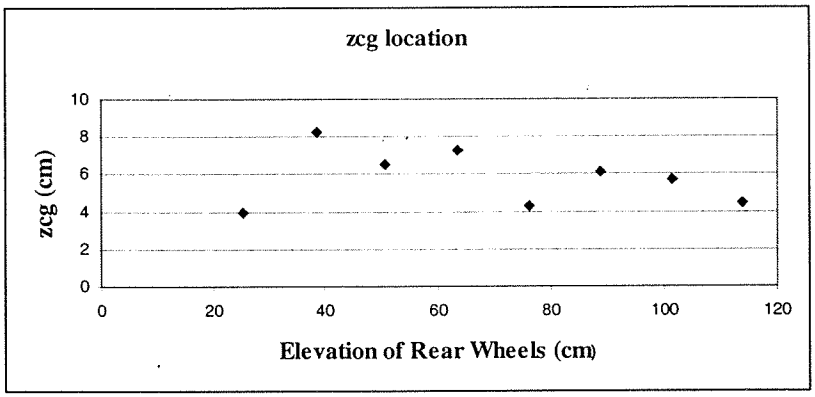

Figure 5.3: Data points used to calculated z_{cg}

Component or Assembly	Weight N (lb)
Complete ARMMACS robot	2091 (470)
Platform w/o the manipulator	1913 (430)
Manipulator	120 (27)
Zebra Mount	60 (14)
Press-on tire (each)	111 N (25 lb)
Pneumatic tire (each)	18 N (4 lb)

Table 5.1: Weight Data

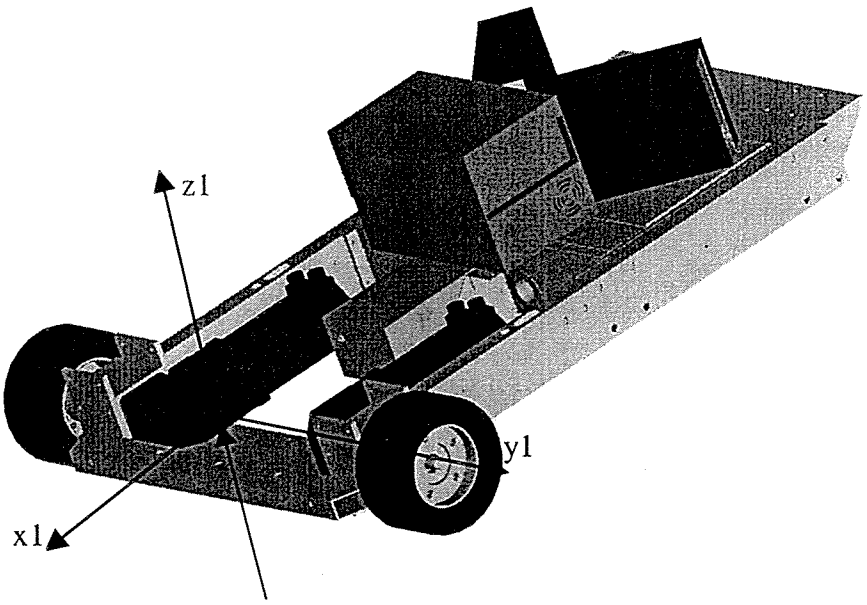

Figure 5.4: Reference Frame Orientation

Assembly	Center of Gravity Location		
	x cm (in)	y cm (in)	z cm (in)
Complete ARMMACS Robot	-42.6 (-16.8)	0.3 (0.1)	15 (6)
Platform w/o the manipulator	-45.7 (-18.0)	0.3 (0.1)	Not Measured

Table 5.2: Center Of Gravity Location

5.2.2 Conclusion on Weight

Significant approximations made in the ARMMACS design process were the total weight (including ballast) and the weight distribution. All structural members of the Frame and the Drive Assembly components were designed using a total weight, including ballast, of 2220 N (500 lb) with 70% distributed to the front and 30 % to the rear. From the measured data given in Table 5.1, the actual total weight is 2090 N (470 lb). Calculations show the actual weight distribution is the same as the assumed distribution. Since the actual weight without ballast is

less than the weight used for design and is distributed as expected, the assumed weight and distribution sufficiently represent the actual system.

5.3 Useful Physical System Parameters

5.3.1 Dimensions

Positioning the robot and the Zebra ZERO manipulator end effector accurately within the workspace requires accurate knowledge of certain fundamental robot dimensions. All dimensions can be determined from the detail prints included in Appendix B; however, many of the most essential dimensions are summarized within this section.

5.3.1.1 Essential Drive Wheel and Manipulator Location Dimensions

Even the most basic dynamic and kinematic models of differentially steered Mobile Robots require the following dimensions: the wheel track (distance between Drive Tire midlines), the tire radius, the location of the Center of Gravity of the robot, and the location of external forces acting on the robot. When a manipulator arm is added to the robotic system, and the goal is to locate and maneuvering its end effector, additional dimensions are required to model the entire system. The most foreseeable of these are the location of the manipulator on the Mobile Robot, the dimensions of the various links of the manipulator, and dimensions to the Center of Gravity of the manipulator in various configurations. Most of the mass of the Zebra ZERO manipulator is concentrated so that regardless of the configuration the Center of Gravity is located near the J1 axis (Figure 2.3); therefore, the latter is minimally important for ARMMACS. Further details about the Zebra ZERO Center of Gravity are not presented in this report; however, approximations can be made using manufacturer data. Specific link dimensions are

also given in the manufacturer data. All other aforementioned dimensions are presented in this Chapter.

Section 5.1.1 presents the Center of Gravity location of the platform and this section lists dimensions that parameterize geometric features of the ARMMACS. Table 5.3 gives dimensions that describe the manipulator location on the mobile platform. Then other important platform dimensions are listed. Last, Table 5.5 correlates the color of the bearing preload shims with their thickness. This will be useful if friction torque adjustments become necessary.

Description	x cm (in)	y cm (in)	z cm (in)
Location of the Manipulator J1 Axis and Base Intersection wrt Reference Frame 1 (Figure 5.1) when Mounted Between Wheels	0	0	-5.72 (-2.25)
Location of Manipulator J1 Axis and Base Intersection wrt Reference Frame 1 (Figure 5.1) when Mounted Outboard the LH Wheel	0	76.78 (30.23)	-5.72 (-2.25)
Location of P1 (Figure 5.3) on Manipulator Homing Nest wrt the Intersection of the Zebra Platform and J1 Axis	41.02 (-16.15)	0	12.83 (5.05)

Table 5.3: Zebra ZERO Manipulator Locations

5.3.1.1.1 Miscellaneous Dimensions

Approximate Effective Press-on Tire Diameter: 25.4 cm (10.0 in)

Approximate Effective Pneumatic Tire Diameter: 25.4 cm (10.0 in)

Track Width (Same for Both Sets of Tires): 107.8 cm (42.4 in)

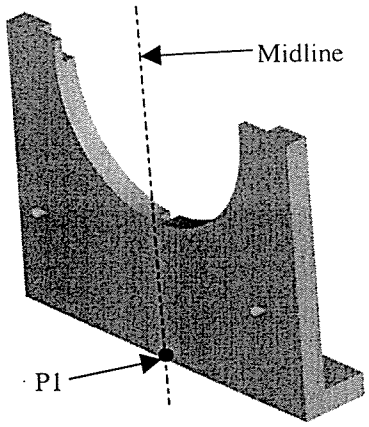

Figure 5.5: Homing Nest

5.3.1.2 Drive Assembly Shim Thickness

Several shims of various thickness form shim packs used in each Drive Assembly to set bearing preload. Using plastic shim stock not only simplified fabrication of the shims, but also simplifies determination of the shim pack thickness. The plastic shim stock used is colored according to its thickness as shown in Table 5.4.

Shim Color	Shim Thickness (mm)	Shim Thickness (in)
Amber	0.025	0.001
Red	0.051	0.002
Green	0.076	0.003
Tan	0.102	0.004
Blue	0.127	0.005
Brown	0.254	0.010

Table 5.4: Shim Stock Thickness Legend

5.3.2 Rotational Inertia

The rotational inertia about the vertical axis is a key dynamic characteristic of ground vehicles especially when torque control is utilized. For uniform objects with common shapes,

rotational inertia calculations are tedious but simple. However, most physical systems including the ARMMACS consist of several components with non-uniform mass distribution and awkward shapes. This makes accurate computation of the rotational inertia difficult. Therefore, a trifilar suspension system such as the one shown in Figure 5.2, will be used to calculate the rotational inertia of ARMMACS from dynamic measurements. ARMMACS will be placed on the suspension system disk with its Center of Gravity aligned with the Center of Gravity of the disk. Forcing the system into oscillation, measuring the period of oscillation, T and substituting into Equation 5.1 (Inman,1996) will determine the rotational inertia, I, of ARMMACS. In Equation 5.1, m represents the mass of the ARMMACS, m_o the mass of the disk, r_o the radius to the cable attachment points, l the length of the suspension wires, I_o the moment of inertia of the disk, T the period of oscillation, and g the acceleration due to gravity.

$$I = \frac{gT^2 r_o^2 (m_o + m)}{4\pi^2 l} - I_o \qquad (5.1)$$

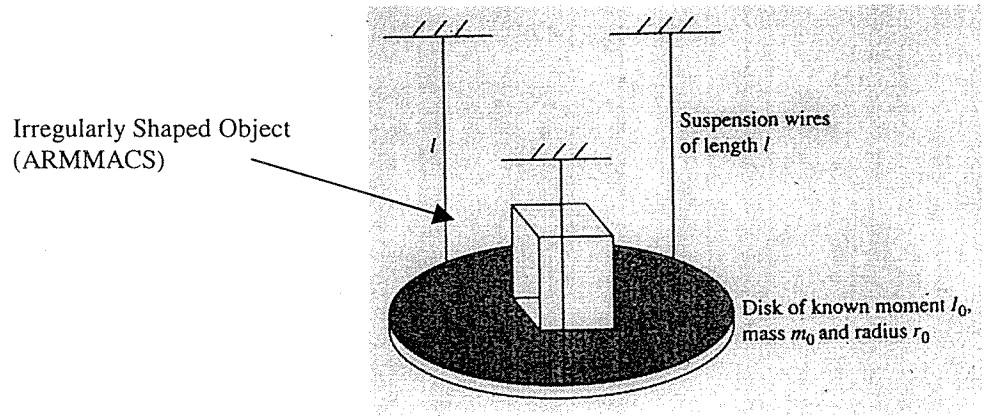

Figure 5.6: Trifilar Suspension System (Inman, 1996)

5.4 Summary

Verifying the accuracy of assumptions used in designing system components is an important part of any engineering project. Important assumptions used to design the ARMMACS robot revolved around its weight. Therefore, in this chapter, measurements of the actual weight and Center of Gravity location were presented and discussed.

In addition, to aid system users, some key dimensions and characteristics of the physical system are summarized within the chapter for easy reference. Dimensions include the track width, Zebra ZERO manipulator location, Homing Nest location, Drive Assembly Shim thickness, and tire dimensions. Additionally, measurement of the rotational inertia about the vertical axis was discussed.

Chapter 6

Conclusions and Recommendations of Section One

6.1 Conclusions

Specification, conception, and detailed design of an Autonomous Redundant Mobile Manipulator with Advanced Control Scheme (ARMMACS) comprise this report. The ARMMACS is a version of a Mobile Manipulator, a type of robot studied by researchers worldwide due to limitless potential applications. Eventually, the Advanced Highway Maintenance and Construction Technology (AHMCT) Research Center at the University of California-Davis intends to deploy a Mobile Manipulator to perform various assistive and automated highway maintenance and construction tasks. ARMMACS is an initial step towards this deployment, serving as a test bed for the advanced control algorithms required to perform these tasks. At least two different mechanical configurations will also be tested on ARMMACS to verify the results of analytical manipulability studies discussed in Gardner and Velinsky (1999).

Product Design Specifications, developed early in the design process, provided target goals that guided the conceptual and detailed design of the ARMMACS ensuring a successful product. Evaluating several conceptual designs for the Frame and Drive Train in light of these specifications resulted in an aluminum tubular Frame and a Drive Train that transmits torque to the Drive Wheels and fully supports all loads imposed on the wheels. Detailed design of these concepts resulted in a reliable robot with the versatility and accuracy necessary to perform the desired operations.

In preliminary testing, the combined Zebra manipulator and mobile platform system has performed well. Electromagnetic noise produced by the servomotors and power electronics has not effected manipulator encoder signals, indicating that the Electrical Box and conduits (frame tubes) provide sufficient shielding. Additionally, the backlash in the assembled Drive Train is limited to that within the gearhead. According to ORMEC, a manufacturer of servomotors, servomotors typically buzz if excessive backlash is present and ring a pure note when the coupling of the servo and load is not adequately stiff. Since the servos do not buzz, this minimal backlash appears acceptable. Furthermore, when the Press-on tires are used (the only tires used so far) the servomotors do not ring a pure note, indicating sufficient drive train torsional stiffness. Extensive testing is awaiting the integration of more advanced control schemes with the physical system. However, the design calculations and simple operations performed so far indicate that the robot functions well. The dynamic and kinematic performance requirements, as well as the strength and stiffness requirements, are satisfied. The frame joints are extremely stiff and the Frame deforms minimally when lifted from any single corner. Likewise, the Zebra Mount is very rigid and locates the manipulator in the primary locations discussed in Gardner and Velinsky (1999). Additionally, all available components were utilized as desired, and custom parts were made of stock materials using common machining operations. Furthermore, based on observation and stiffness data available, the selected tires meet the compliance requirements.

Product Design Specifications developed early in the design process represented the ideal machine. While the final design satisfies many of the design specifications exactly, carrying out the detailed design required compromises to overcome conflicting specifications. For instance, using the available stock components drove the maximum desired platform-to-manipulator

weight ratio beyond the desired value of 10. As built, the estimated Frame and Drive Train weight is approximately 781 N (176 lb) with the Press-on tires resulting in a total platform weight of 1970 N (444 lb) when the Press-on tires are used and 1790 N (402 lb) with the Pneumatic tires. This weight includes all components except the manipulator. From this, the stock components (servomotors , gearheads, motor drives, computer, and power supply and power and control electronics) weigh 1190 N (268 lb). Since the manipulator weights 120 N (27 lb) the weight of the stock components alone result in a weight ratio of 10. When the Zebra Mount is included in the total platform weight, the as built platform-to-manipulator weight ratio is 16 with the Press-on tires and 15 with the Pneumatic tires.

Designing the Drive Train also required a compromise. Employing tires with enough compliance to produce sufficient traction inherently reduces the natural frequency of the Drive Train below the specified 500Hz. Utilizing a coupling that allows misalignments decreases this value further yet. With the minimally compliant (Press-on) tires and the Zero-Max 6A37C Composite Disk coupling, the approximate natural frequency is 315 Hz, using tire stiffness data from the manufacturer included in Appendix C. Although the torsional stiffness of the Composite Disk Coupling is less than desired, it provides the highest stiffness of all couplings found that allow shaft misalignments and transmit sufficient torque with zero backlash.

Although the design functions well and meets the specification sufficiently, the platform footprint is quite large relative to the manipulator. While this does not hinder the mechanical functionality at the platform level, the maneuverability of the ARMMACS within a relatively small laboratory workspace is decreased. Besides, the mobile platform dwarfs the Zebra ZERO manipulator hampering the cosmetics of the robot. Simply analyzing the workspace during

product definition and specifying maximum platform dimensions could have prevented this problem.

6.2 Recommendations

To improve future designs, project efficiency, and engineering skills, the clarity of hindsight must be recognized and capitalized upon by reviewing the final project. In hindsight, design flaws and the roots of inefficiencies seem more trivial. Although the ARMMACS satisfies the design specifications sufficiently, several aspects of the design and design process leave room for improvement. This section discusses potential process and design refinements.

6.2.1 Possible Chassis Improvements for Future Designs

In retrospect, the ARMMACS Chassis ails most in two ways. First, it weighs more than desired. Second, as discussed in the conclusion, the Chassis is large with respect to the Zebra manipulator and the workspace. These characteristics can easily be improved in future designs; some ideas for improvements are presented in this section.

For the most part, the weight and size of the ARMMACS are correlated. Most likely, future Mobile Manipulators developed by the AHMCT Center will implement larger manipulators, and the size of the current platform may be appropriate or even too small. However, if more Mobile Manipulators are developed with similar size manipulators, reducing both the weight and the size of the platform may prove beneficial. Vast improvements of both characteristics simply require using servomotors, motor drives, and gearheads with sizes more compatible with the manipulator. Electro-Craft®, the manufacturer of the motors used on ARMMACS, offers a Micro Drive line of servomotor drives that are ¼ the size of the drives

used. Also, for robots of similar size, servomotors with less torque capability should provide sufficient performance. Selecting smaller electrical components such as relays and fuses will reduce the size of packaging and thus the Chassis weight. Additionally, while the Press-on tire and wheel assemblies provide superb stiffness, mounting capability and reliability compared to other options, they are also heavy. A more in depth exploration of available tires may result in a better solution for future designs. If not, machining material from the wheels or fabricating aluminum wheels will reduce the assembly weight somewhat. The components discussed above constitute the highest percentage of the ARMMACS weight, thus reducing their weights will have the highest impact on the total weight. Nevertheless, reducing the frame tube size will also decrease the weight slightly. However, the use of smaller frame tubes should be validated by more detailed deflection analysis.

6.2.2 Possible Drive Train Improvements

In retrospect, a timing belt with toothed sheaves may have worked well for coupling the Drive Shaft with the gearhead output shaft. Several manufacturers produce reinforced timing belts for use in precision applications. These belts are stiff enough for servomotor applications and, when used with appropriate sheaves, provide a backlash free coupling. Using timing belts increases the geometric layout possibilities allowing a more compact design. For instance, stacking the motor and gearhead assemblies of the ARMMACS above the area of the current Coupling Housing or moving them aft the Zebra ZERO manipulator would permit a narrower Frame. Moreover, using belts increases shaft misalignment tolerances, thus reducing the cost and complexity of the Drive Train. Therefore, transmitting torque to the drive wheels of future Mobile Robots with belts is recommended. However, careful engineering is necessary to ensure

sufficient belt stiffness. Along the same lines, stand alone gearheads should be considered when designing future mobile robots demanding compactness and high performance. Coupling these gearheads to both the wheels and to the motors with belts increases configuration options.

Equally important, for future mobile robots with similar or greater loads applied to the wheels, implementing a single Double Row Angular Contact Ball Bearing per wheel may provide a stiffer and smaller axle assembly. Proven by their use in several modern automobile hubs, these bearings accommodate high radial and moderate axial loads. However, these bearings cannot be axially preloaded so their use is limited accordingly. Complete hub assembly options available from bearing manufacturers such as SKF® should also be considered. If axial preload adjustment capability is desired, Single Row Angular Contact Ball Bearings work very well. When using these bearings, they should be arranged in a back-to-back configuration so that their pressure centers are further apart than the bearing midlines. This arrangement results in the smallest radial loads, thus providing the stiffest assembly and longest bearing life. The ARMMACS Axle Assembly could be modified for a back-to-back arrangement, but would require unjustified modifications to the Drive Shaft and Axle. A back-to-back arrangement was avoided initially because it requires slightly more complicated Axle geometry and an additional bearing retainer. Furthermore, it requires a transitional-fit for the rotating raceway, which is typically not recommended. Before finding the flaws in the life calculations, these complications were not justified.

6.2.3 Other Possible Improvements

The Cable Extension Transducer (CET) based position and heading sensor is a low cost and practical sensor capable of precise sensing within the laboratory environment. However, in

the future, a more robust sensor must be found or developed for unstructured highway maintenance operations in more harsh environments. CETs provide precise measurements; however, they are mechanical instruments easily damaged during robot operation. Cables are easily frayed or kinked when their motion is obstructed or when they are struck. Therefore, pulley mechanisms must be carefully designed to ensure the cables stay in their triangular configuration and operate smoothly. Furthermore, the tension in the cables and their stiffness are low and the cables may sag as the robot moves further from the CETs causing erroneous distance. Also, a long length of unsupported cable has a low natural frequency and may be excited by normal operations causing relatively large oscillations and noisy encoder signals.

6.2.4 Possible Testing

If the end effector force sensor readings are noisy and mechanical vibrations are suspected, the vibratory response of the Zebra Mount should be analyzed. Due to awkward geometry, accurate analytical modeling of the Zebra Mount stiffness and mass would be cumbersome. Consequently, if analysis becomes necessary, experimentally analyzing the vibratory response due to forced excitation using accelerometers is recommended.

Chapter 7

Kinematics of Mobile Manipulators and Implications for Design

A systematic, unified kinematic analysis for manipulator arms mounted to mobile platforms is presented. The differential kinematics for the composite system is used, along with an extended definition of manipulability, to generate a design tool for this class of systems. An example is presented in which a 3 DOF anthropomorphic manipulator is mounted on a platform powered by two independent drive wheels. Scaled manipulability ellipses are used to visualize the effect of manipulator mounting position on the overall mobility of the system. Given information about the intended tasks of the mobile manipulator, conclusions may be drawn as to the most appropriate mounting site. For the tasks which motivated this research, automated highway construction and maintenance, it was concluded that the manipulator base should be near the axles of the drive wheels and far from the centerline of the platform.

7.1 Introduction

Recent advances in the field of robotics, computer vision and production practices have made possible the automation of many tasks involved with highway construction and maintenance. Several of these are summarized in the literature (West et al., 1995). Automated devices have been developed for numerous highway tasks which include, for example, robotic crack sealing (Velinsky 1993; Mueller et al., 1996) and robotic pavement lettering and marking (Kockekali and Ravani 1994). At the Advanced Highway Maintenance and Construction Technology Research (AHMCT) Center at the University of California, Davis, researchers are developing a mobile robotic platform equipped with a robotic manipulator arm. This work

presents a unified kinematic analysis which allows for the systematic analysis of mobile manipulators. In particular, it will lead to design tools that will indicate the effects of geometric parameters on overall mobility.

It is envisioned that this robotic system can be used in conjunction with traditional maintenance vehicles to aid in timely completion of various tasks. It would be particularly attractive to perform tasks 'on the fly' thereby eliminating the need for troublesome static lane closures. To bring this about, the robotic system must be adequately quick and dexterous such that the robot arm can interact with the road surface at a given point while maintaining the platform down-lane velocity near a constant level. While there are several examples of mobile manipulators to be found in the literature, no one has considered applications which require this level of coupling between the manipulator arm and the mobile platform.

The kinematics and control of simple mobile platforms are well understood and have become part of the standard curriculum for students studying robotics (McKerrow 1991). Borenstein and Koren (1997) present an early application of a manipulator arm on a mobile base. In this work, they discuss control strategies but offer no unifying framework to deal with the kinematics of the arm and the mobile base. In another work (Alexander and Maddocks 1989), the authors model the kinematics of wheeled platforms common to mobile manipulator applications. In this work, the emphasis is on the avoidance of slipping.

In several works (Jagannathan et al., 1994; Seraji 1995; Pin et al., 1996; Yamamato and Yun 1994; Yamamato and Yun 1993) the authors investigate the relationship between base and manipulator kinematics. A Lagrangian-based dynamics approach applied to path planning and input-output feedback linearizationis presented (Jagannathan et al., 1994). In another work (Seraji 1995), the author looks at the problem of appropriate base placement for a given task. A

fundamental premise of this work is that the platform is to be brought to a certain location, then the manipulator performs the task, as opposed to a truly integrated approach. The issue of motion planning for mobile manipulators is presented in which the authors uses a unified kinematic treatment for path planning and redundancy resolution (Pin et al., 1996). Similar approaches are found which use a similar approach and focus on the control of the mobile manipulators (Yamamato and Yun 1993; 1994).

Unique applications also give rise to studies in the area of mobile manipulators. Egeland and Sagli (1993) discuss the issue of control of a manipulator mounted on an orbiting platform while other authors (Simon et al., 1997; Tarn and Yang 1997) discuss issues inherent in underwater manipulator systems. In both cases, the dynamics for specific configurations are presented, but little is concluded about design issues.

Another interesting application is described by Nagatani and Yuta (1996a; 1996b) in which the task of opening a door is solved using a mobile manipulator. This work makes use of hierarchical control and extensive sensor fusion to accomplish the task. The procedure is shown to work with little or no kinematics modeling.

Nassal (1996) presents a control scheme which utilizes the kinematics of the manipulator-platform system for decoupling of the control. Like most of the research done in this area, no attempt is made to apply the kinematic modeling to design issues in mobile manipulators.

Seraji (1993) presents the unified kinematics of mobile manipulators in terms of the Jacobian matrices of the individual units. The resulting redundant equations are solved using weighted pseudo-inverses and a geometry-based control scheme is presented. The author makes some important observations about the manipulability of the composite system compared to the

individual subsystems. Again, issues that effect design of the mobile manipulator system are not considered.

The issue of manipulability, as defined by Yoshikawa (1985a), is critical to mobile manipulators. These systems are nearly always kinematically redundant so some measure of manipulability is often used to resolve the redundancy. The concept of manipulability has been expanded in several ways, notably by Yoshikawa (1985b) in which dynamic manipulability is introduced and by Doty (1995) in which the authors point out certain shortcomings in the traditional manipulability measures and suggest alternatives based on screw theory. Finally, Matone (1998) considers actuator dynamics and other factors within the concept of manipulability.

In general, most of the literature dealing with mobile manipulators focuses on methods to decouple the control of the two subsystems. An underlying assumption throughout the literature is that the mobile platform is a means of transporting the otherwise stationary manipulator arm to the vicinity of the task. Once there, the operation proceeds as it would normally proceed with a stationary manipulator.

A unique aspect of this work is the consideration of a set of tasks which require that the manipulator operate while the platform is attempting to achieve an unrelated task (maintaining down-lane velocity). In this situation, the placement of the manipulator on the platform can have a large effect on the over-all performance. We will now present the description of the kinematics of mobile manipulators, followed by an extension of the concept of manipulability which is particularly useful for this class of robots. Finally, we will look at an example and investigate the effect of manipulator placement on the overall manipulability of the system.

7.2 Geometry and Kinematics of Mobile Manipulators

Figures 7.1 and 7.2 define the reference frames and vectors required to model the kinematics of a mobile manipulator. The global reference frame is **{G}** while the frame at the manipulator's end effector is **{E}**. The navigation vector, $\underline{P}$, represents the position of the mobile platform. We also define the coordinate frame **{O}** attached to the mobile platform at a point mid-way between the two drive wheels, with its x-axis oriented in the direction of forward motion. Finally, the frame **{B}** is located at the base of the manipulator. The vector $\underline{R}$ is defined as the location of **{B}** relative to **{O}**. Figures 7.1 and 7.2, **{O}** and **{B}** are coincident.

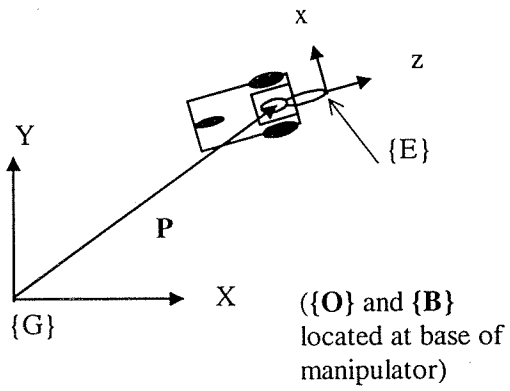

Figure 7.1: Top view of global reference frame {G} and a reference frame on the tool of the manipulator, {E}. The navigation vector, P, also includes orientation of the platform relative to {G}

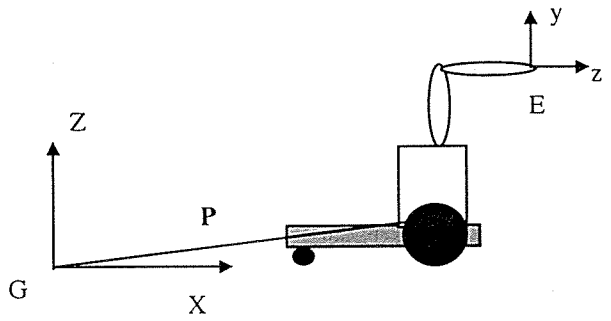

Figure 7.2: Side view of mobile manipulator with two reference frames indicated

For a stationary manipulator, the differential kinematics are well understood and often expressed in the following velocity transform

$$ {}^{B}\underline{v}_{E} = \mathbf{J}_{m}\dot{\underline{q}} \tag{7.1} $$

which computes the velocity of the end effector, relative to a reference frame for the manipulator **{B}**, usually taken at the base of the manipulator itself. When the manipulator is mounted on a moving platform, the motion of the end effector is also affected by the platform motion. The navigation vector, $\underline{P}$, describes the position of frame **{O}** and $\underline{\theta}$ its orientation.

$$ \underline{S} = \begin{bmatrix} \underline{P} \\ \underline{\theta} \end{bmatrix} = \begin{bmatrix} p_x \\ p_y \\ p_z \\ \theta_x \\ \theta_y \\ \theta_z \end{bmatrix} \tag{7.2} $$

The velocity of the mobile platform is simply the derivative of this vector. To find the velocity of the end effector of a manipulator on a moving platform, we combine the traditional Jacobian matrix formulation shown in (7.1) with the platform kinematics as shown:

$$ {}^{G}\begin{bmatrix} \underline{v} \\ \underline{\omega} \end{bmatrix}_{E} = \mathbf{J}_{m}\dot{\underline{q}} + \mathbf{J}_{mp}\begin{bmatrix} \dot{p}_x \\ \dot{p}_y \\ \dot{p}_z \\ \omega_x \\ \omega_y \\ \omega_z \end{bmatrix} \tag{7.3} $$

$$ \mathbf{J}_{mp} = \begin{bmatrix} \mathbf{I} & \mathbf{Q} \\ \mathbf{0} & \mathbf{I} \end{bmatrix} $$

where **I** is the 3x3 identity matrix and **Q** is the skew symmetric matrix of the following form:

$$\mathbf{Q} = \begin{bmatrix} 0 & \rho_z & -\rho_y \\ -\rho_z & 0 & \rho_x \\ \rho_y & -\rho_x & 0 \end{bmatrix} \tag{7.4}$$

The vector $\underline{\rho}$ is the vector from the origin of the platform frame **{O}** to the origin of the end effector frame **{E}**. This is the resultant of the end-effector position vector as defined by the manipulator geometry and the vector locating the manipulator in the platform frame, which we denote as $\underline{R}$. The latter vector is an important variable in the design of a mobile manipulator.

To bring together the kinematics and control of the mobile platform and the manipulator, we must relate the navigation vector to the motion of the platform wheels, which is represented as:

$$\underline{\dot{P}} = \mathbf{J}_p \underline{\dot{\psi}} \tag{7.5}$$

where $\mathbf{J}_p$ is the appropriate matrix for the platform and $\underline{\dot{\psi}}$ is the vector of wheel velocities for the platform. Combining Eqns. (7.5) and (7.3) yields the following expression for the differential kinematics of a mobile manipulator.

$${}^{G}\underline{v}_E = \left[\mathbf{J}_m \vdots \mathbf{J}_{mp}\mathbf{J}_p\right]\begin{bmatrix} \underline{\dot{q}} \\ \underline{\dot{\psi}} \end{bmatrix} \tag{7.6}$$

7.3 Manipulability: Some Definitions

Equation (7.6) shows the differential transformation for a general mobile manipulator based on the individual Jacobian matrices of the manipulator and the mobile platform. Since many manipulators have five or six Degrees of Freedom (DOF) and mobile platforms generally have at least two individually powered wheels, Eqn. (7.6) will often indicate that the mobile manipulator system is redundant in that it will have more than 6 independently controllable

DOF's. In addition, it should be noted that the Jacobian matrix in Eqn. (7.6) is dependent not only upon the manipulator configuration, but also on the placement of the manipulator on the mobile platform (given by the vector $\underline{R}$).

A common index of manipulability is based on the singular values, σ, of the Jacobian matrix (Yoshikawa 1985a), and is expressed as

$$\mu = \sigma_{\min}(\mathbf{J}) \tag{7.7}$$

where σ_{min} is the minimum singular value of the Jacobian matrix. The physical meaning of this index is rather straightforward. Given the set of all joint velocity vectors which have a geometric norm of 1 (defined by a unit sphere centered at the origin of the joint space), the singular values give the maximum velocity of the end effector which is achievable choosing joint velocity vectors from that set. Different singular values represent the maximum achievable velocities in the various orthogonal directions in the task space. While the minimum singular value (as shown in Eqn. (7.7)) is often used as a general index of manipulability, it is often better to assess manipulability of the system based on the task requirements, as will be shown later in this report.

A major difficulty with manipulability measures such as the one shown in Eqn.(7.7) is that it cannot take into account that the various actuators are, in general, capable of achieving very different maximum velocities. In an effort to improve this measure of manipulability, the maximum velocity of each actuator can be used to scale the joint velocities. A new Jacobian matrix is defined based on these new, normalized velocities. For example, the normalized velocities, $\underline{\hat{\dot{q}}}$, can be defined as follows:

$$\begin{bmatrix} \dot{q}_1 \\ \dot{q}_2 \\ \vdots \\ \dot{q}_n \end{bmatrix} = \begin{bmatrix} \omega_{1\max} & & & \\ & \omega_{2\max} & & \\ & & \ddots & \\ & & & \omega_{n\max} \end{bmatrix} \begin{bmatrix} \hat{\dot{q}}_1 \\ \hat{\dot{q}}_2 \\ \vdots \\ \hat{\dot{q}}_n \end{bmatrix} \tag{7.8}$$

The scaled joint rates, $\underline{\hat{\dot{q}}}$, are normalized and take on values between -1 and 1 and $\omega_{i\ max}$ is the maximum joint rate achievable by each joint actuator. Note that this concept works just as well for traditional manipulators with both revolute prismatic joints as it does for the powered wheels of mobile platforms. Therefore, substituting (7.8) into (7.6), we define the following scaled Jacobian Matrix, $\hat{\mathbf{J}}$, for mobile manipulators.

$${}^{G}\underline{v}_{E} = \left[\mathbf{J}_m \vdots \mathbf{J}_{mp}\mathbf{J}_p\right] \begin{bmatrix} \omega_{1x} & & & \\ & \omega_{2x} & & \\ & & \ddots & \\ & & & \omega_{nx} \end{bmatrix} \begin{bmatrix} \hat{\underline{\dot{q}}} \\ \hat{\underline{\dot{\psi}}} \end{bmatrix} = \hat{\mathbf{J}} \begin{bmatrix} \hat{\underline{\dot{q}}} \\ \hat{\underline{\dot{\psi}}} \end{bmatrix} \tag{7.9}$$

The singular values of $\hat{\mathbf{J}}$ will now be much better indicators of actual robot performance since they will predict the maximum end effector velocities possible within a unit sphere of the scaled joint velocities. In actuality, the allowable region for joint velocities is a unit hyper-cube centered at the origin, so this representation is somewhat conservative.

7.4 Geometric Representation of Manipulability

While there has been much written about the use of the singular values of the Jacobian as an index of performance, or perhaps to resolve redundancy, the concept is also very useful in the geometric design of manipulators for specific tasks. Consider, for example, the well known two link serial chain with two motion parameters, θ_1 and θ_2 and link lengths l_1 and l_2. It can easily be shown that the Jacobian relating the end-effector velocity to the joint rate is given by:

$$\begin{bmatrix} v_x \\ v_y \end{bmatrix} = \begin{bmatrix} -(l_1 S_1 + l_2 S_{12}) & -l_2 S_{12} \\ l_1 C_1 + l_2 C_{12} & l_2 C_{12} \end{bmatrix} \begin{bmatrix} \dot{\theta}_1 \\ \dot{\theta}_2 \end{bmatrix} \tag{7.10}$$

where $S_1 = \sin(\theta_1)$, $S_{12} = \sin(\theta_1+\theta_2)$, $C_1=\cos(\theta_1)$, and $C_{12}=\cos(\theta_1+\theta_2)$.

The singular value decomposition yields the eigenvalues and eigenvectors of this Jacobian. It is well known that these define an ellipse, the major axes of which are oriented in the directions of the eigenvectors and the magnitudes of which are the eigenvalues (Murray et al., 1994). This is often referred to as the manipulability ellipse. Since the matrix itself is configuration dependent (depends on θ_1 and θ_2), then we can expect the manipulability ellipse to also vary throughout the workspace of the manipulator.

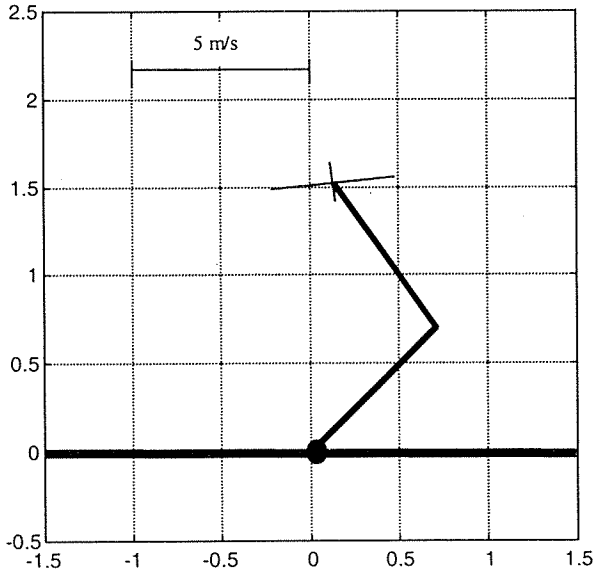

Figure 7.3: A two-link manipulator shown in the position of □1 = 45 and □2 = 80, with the manipulability ellipse indicated by its major axes.

Figure 7.3 is easy to interpret. The manipulability ellipse is represented by its major and minor axes centered at the end-effector. The lengths of these axes represent the maximum velocities achievable by the manipulator end effector for all possible combinations of joint rates

such that the norm of the joint rate vector is unity. For this particular situation, we see that the manipulator is most 'mobile' in a direction that is somewhat askew from the x-direction, and that it could move in that direction with a velocity near 3 m/s. In the direction orthogonal to that, it can only move approximately 1 m/s. A sampling of such ellipses throughout the manipulator workspace can be very illuminating for the motion capabilities of that manipulator.

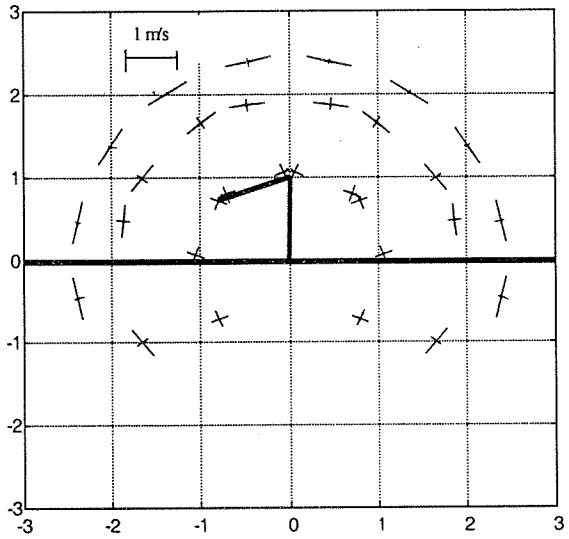

Figure 7.4: A sampling of manipulability ellipses for a the two-link manipulator.

Figure 7.4 shows an array of manipulability indices in the form of ellipse axes for the two-link manipulator over a range of motion throughout the workspace. Notice that the longest axes occur at the very edge of the workspace (giving both motors the longest moment arm) but that the minor axes vanish at these locations. This is consistent with the fact that those locations represent singularities of the manipulator and no velocity in the direction normal to the major axes is possible.

In the next section, these methods will be applied to a three DOF manipulator mounted on a mobile platform which is powered by two independently controllable wheels. The affect of manipulator mounting location on the over all manipulability will be considered.

7.5 Analysis of Manipulator Placement on the Platform

As noted earlier, at the Advanced Highway Maintenance and Construction Technology Research (AHMCT) Center at the University of California, Davis, researchers are developing a mobile robotic platform equipped with a robotic manipulator arm. The manipulator is the "Zebra ZERO" robot from Integrated Motions, Inc. of Berkeley, CA. It is a 6 DOF manipulator in an anthropomorphic configuration. The first three joints consist of a vertical axis ("waist") and two parallel horizontal axes ("shoulder" and "elbow"). The final three degrees of freedom occur with intersecting axes and form a wrist. In general, the gross motion of the manipulator occurs with the first three DOF of the manipulator while the fine motion and orientation are done by the 3 wrist motors. Figure 7.5 shows these first three DOF's and the geometric parameters which define the link lengths of the manipulator.

The platform design is similar to the tethered mobile robots previously designed at AHMCT 3. Mobility is provided by two individually powered wheels (geared to DC servomotors) and one or more passive casters. Navigation is accomplished through differential steering of the two motors. Figure 7.6 shows the layout and pertinent geometric parameters.

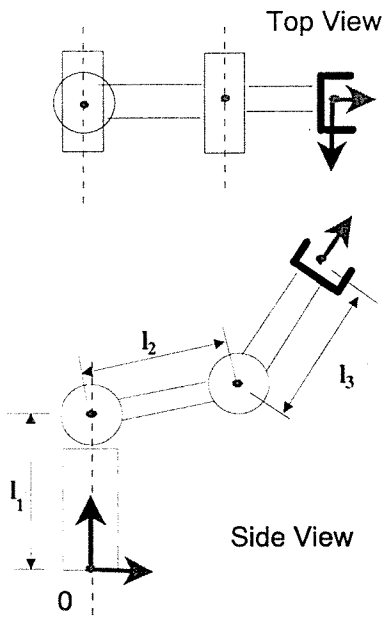

Figure 7.5: Schematic of the first 3 DOF of the Zebra ZERO Robot.

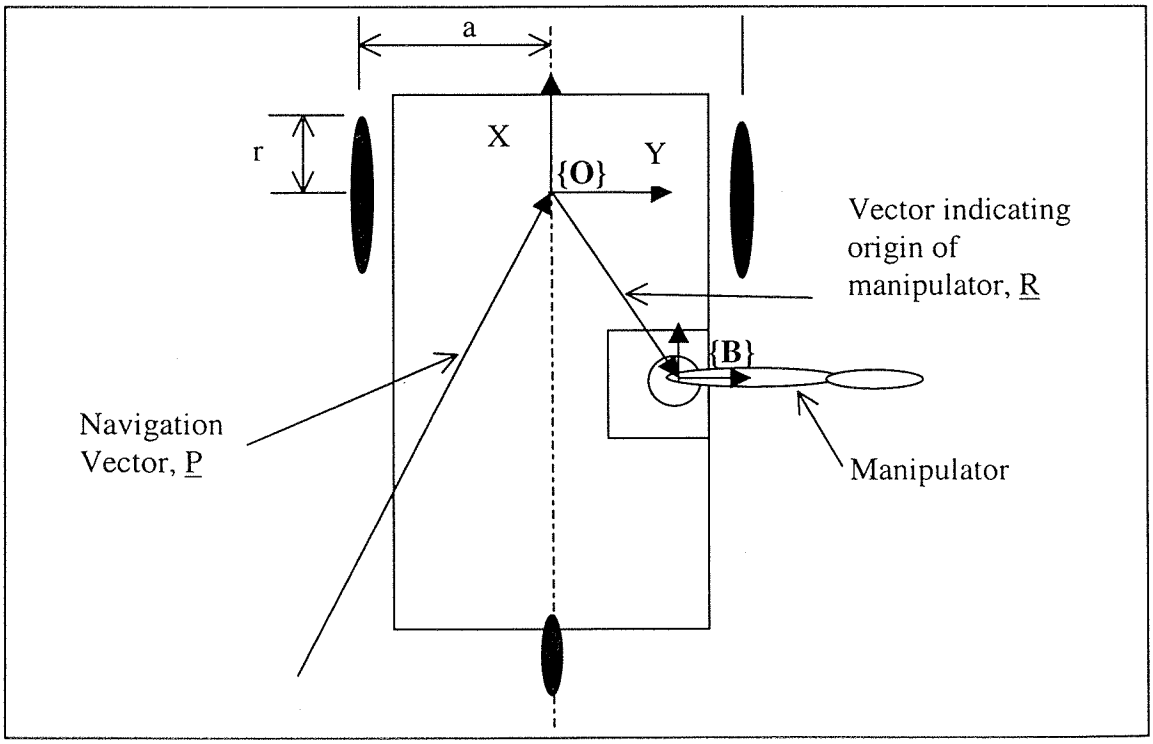

Figure 7.6: Layout of mobile manipulator system indicating the origin of the platform frame {O}(reference point for the navigation vector), origin of the manipulator frame, {B}, wheel base (2a) and drive wheel radius (r).

The manipulator itself is easily analyzed and the reader is referred to any one of a number of excellent texts on introductory robotics for details (Craig 1989; McKerrow 1991; Murry et al., 1994). For the purposes of this example, we will limit our attention to the first 3 DOF of the Zebra robot since these are responsible for the majority of the mobility. The homogenous transformation which relates the position and orientation of the end effector relative to the coordinate frame at the base of the robot is expressed as:

$$ {}^{B}_{E}\mathbf{T} = \begin{bmatrix} C_1C_{234} & S_1 & C_1S_{234} & l_cC_1 \\ S_1C_{234} & -C_1 & S_1S_{23} & l_cS_1 \\ S_{234} & 0 & -C_{234} & l_1 + l_s \\ 0 & 0 & 0 & 1 \end{bmatrix} \tag{7.11} $$

where:

$_c = l_2C_2 + l_3C_{23}$

$l_s = l_2S_2 + l_3S_{23}$

$S_{234} = \sin(\theta_2 + \theta_2 + \theta_4)$, etc.

The homogeneous transformation shown in (7.11) is just part of the entire transformation which relates the end effector frame **{E}** to the global frame **{G}**. The entire relationship can be represented as:

$$ {}^{G}_{E}\mathbf{T} = {}^{G}_{O}\mathbf{T}\ {}^{O}_{B}\mathbf{T}\ {}^{B}_{E}\mathbf{T}. \tag{7.12} $$

Without of loss of generality, we assume that the manipulator reference frame **{B}** shares the same orientation as the platform reference frame, **{O}**. Therefore, the relationship between the two frames is a simple translation given by:

$$ {}^{O}_{B}\mathbf{T} = \begin{bmatrix} 1 & 0 & 0 & r_x \\ 0 & 1 & 0 & r_y \\ 0 & 0 & 1 & r_z \\ 0 & 0 & 0 & 1 \end{bmatrix}. \tag{7.13} $$

This translation defines the placement of the manipulator on the mobile platform. Finally, the navigation vector combined with the heading angle, θ_0, relates the mobile platform frame **{O}** to the global frame as

$$ {}^{G}_{O}\mathbf{T} = \begin{bmatrix} C_0 & -S_0 & 0 & p_x \\ S_0 & C_0 & 0 & p_y \\ 0 & 0 & 1 & p_z \\ 0 & 0 & 0 & 1 \end{bmatrix}. \tag{7.14} $$

The heading angle, θ_0, is defined as the angle between the global x-axis and the x-axis of the platform frame, **{O}**.

Recall in the first portion of this report, the vector $\underline{\rho}$ was defined as the position vector from the origin of the platform frame **{O}** to the origin of the tool frame **{E}**. Multiplying (7.11) by (7.13), the resultant transformation will yield $\underline{\rho}$, that is

$$ {}^{O}_{E}\mathbf{T} = \begin{bmatrix} C_1C_{234} & S_1 & C_1S_{234} & r_x + l_cC_1 \\ S_1C_{234} & -C_1 & S_1S_{23} & r_y + l_cS_1 \\ S_{234} & 0 & -C_{234} & r_z + l_1 + l_s \\ 0 & 0 & 0 & 1 \end{bmatrix} \tag{7.15} $$

Finally, multiplying (7.13) by (7.14) yields a representation of the end effector frame relative to the global frame, **{G}** as

$$ {}^{G}\mathbf{A}_{E} = \begin{bmatrix} C_{01}C_{234} & S_{01} & C_{01}S_{234} & l_cC_{01} + r_xC_0 - r_yS_0 + p_x \\ S_{01}C_{234} & C_{01} & S_{01}S_{234} & l_cS_{01} + r_xS_0 + r_yC_0 + p_y \\ S_{234} & 0 & -C_{234} & l_1 - l_s + r_z + p_z \\ 0 & 0 & 0 & 1 \end{bmatrix}. \tag{7.16} $$

Following the derivation in the first portion of this report, the differential kinematics can also be derived. The 3x3 Jacobian matrix for the Zebra robot can be shown to be:

$$\begin{bmatrix} \dot{E}_x \\ \dot{E}_y \\ \dot{E}_z \end{bmatrix} = \begin{bmatrix} -l_c S_1 & -l_s C_1 & -l_3 C_1 S_{23} \\ l_s C_1 & -l_c S_1 & -l_3 S_1 C_{23} \\ 0 & -l_c & -l_3 C_{23} \end{bmatrix} \begin{bmatrix} \dot{\theta}_1 \\ \dot{\theta}_2 \\ \dot{\theta}_3 \end{bmatrix} \tag{7.17}$$

From (7.15), we can extract $\underline{\rho}$ and assemble the skew symmetric rotation matrix shown in (7.4) as

$$\mathbf{Q} = \begin{bmatrix} 0 & r_z + l_1 + l_s & -(r_y + l_c S_1) \\ -(r_z + l_1 + l_s) & 0 & r_x + l_c C_1 \\ r_y + l_c S_1 & -(r_x + l_c C_1) & 0 \end{bmatrix}. \tag{7.18}$$

Note that Eqn. (7.3) represents the differential kinematics for the most general case of three translational and three rotational degrees of freedom. This example is simplified by restricting our attention to the first 3 DOF of the manipulator and by ignoring the elevation of the mobile platform (p_z) and the rotations of the platform about x and y (pitch and roll). For most mobile manipulator problems they are negligible. Eqn. (7.3) becomes:

$$\begin{bmatrix} \dot{E}_x \\ \dot{E}_y \\ \dot{E}_z \end{bmatrix} = \begin{bmatrix} -l_c S_1 & -l_s C_1 & -l_3 C_1 S_{23} \\ l_s C_1 & -l_c S_1 & -l_3 S_1 C_{23} \\ 0 & -l_c & -l_3 C_{23} \end{bmatrix} \begin{bmatrix} \dot{\theta}_1 \\ \dot{\theta}_2 \\ \dot{\theta}_3 \end{bmatrix} + \begin{bmatrix} 1 & 0 & -(r_y + l_c S_1) \\ 0 & 1 & r_x + l_c C_1 \end{bmatrix} \begin{bmatrix} \dot{p}_x \\ \dot{p}_y \\ \dot{\theta}_0 \end{bmatrix}. \tag{7.19}$$

The last piece is provided by Eqn. (7.5), the relationship between the motion of the platform wheels and the navigation vector. For the platform shown in Figure 7.6, that relationship is:

$$\begin{bmatrix} \dot{p}_x \\ \dot{p}_y \\ \dot{\theta}_0 \end{bmatrix} = \begin{bmatrix} C_0 \frac{r}{2} & C_0 \frac{r}{2} \\ S_0 \frac{r}{2} & S_0 \frac{r}{2} \\ -\frac{r}{2a} & \frac{r}{2a} \end{bmatrix} \begin{bmatrix} \dot{\psi}_l \\ \dot{\psi}_r \end{bmatrix} \tag{7.20}$$

where ψ_l is the rotation of the left drive wheel and ψ_r is the rotation of the right drive wheel. Combining (7.19) with (7.20) yields the differential kinematic relationship for the manipulator-platform combination as

$$\begin{bmatrix} \dot{E}_x \\ \dot{E}_y \\ \dot{E}_z \end{bmatrix} = \begin{bmatrix} -l_c S_{01} & -l_s C_{01} & -l_3 C_{01} S_{23} & \frac{r}{2a}[l_c S_{01} + r_x S_0 + C_0(r_y + a)] & \frac{-r}{2a}[l_c S_{01} + r_x S_0 + C_0(r_y - a)] \\ l_s C_{01} & -l_c S_{01} & -l_3 S_{01} C_{23} & \frac{-r}{2a}[l_c C_{01} + r_x C_0 - S_0(r_y + a)] & \frac{r}{2a}[l_c C_{01} + r_x C_0 - S_0(r_y - a)] \\ 0 & -l_c & -l_3 C_{23} & 0 & 0 \end{bmatrix} \begin{bmatrix} \dot{\theta}_1 \\ \dot{\theta}_2 \\ \dot{\theta}_3 \\ \dot{\psi}_l \\ \dot{\psi}_r \end{bmatrix}. \tag{7.21}$$

Notice that the third equation in (7.21) deals with the movement of the end effector in the z-direction. Consistent with our earlier assumption that the vertical motion of the platform is negligible, the vertical motion of the end effector depends only on the joint rates of the manipulator itself. Note also that the Jacobian matrix depends upon the location of the manipulator on the mobile platform as described in the coordinates $[r_x, r_y]$. In the following section, the manipulability index as described previously will be used to assess various mounting positions of the manipulator in an effort to choose a preferred location.

7.6 Analysis of Various Mounting Positions in its Impact on Mobility

The Jacobian used to compute manipulability will be different from the one indicated in (7.21) in two respects. First, we will use only the first two rows of the Jacobian because the majority of the tasks envisioned for the system will require that the tool be interacting with the

road surface, making vertical motion a secondary goal. Second, we will perform the scaling described in (7.9) to account for varying motor sizes. Accordingly Eqn. (7.21) is re-written as

$$\hat{\mathbf{J}}=\begin{bmatrix} -l_e S_{01}\omega_{1\max} & -l_s C_{01}\omega_{2\max} & -l_3 C_{01}S_{23}\omega_{3\max} & \frac{r\psi_{l\max}}{2a}[l_e S_{01}+r_x S_0+C_0(r_y+a)] & \frac{-r\psi_{r\max}}{2a}[l_e S_{01}+r_x S_0+C_0(r_y-a)] \\ l_s C_{01}\omega_{1\max} & -l_e S_{01}\omega_{2\max} & -l_3 S_{01}C_{23}\omega_{3\max} & \frac{-r\psi_{l\max}}{2a}[l_e C_{01}+r_x C_0-S_0(r_y+a)] & \frac{r\psi_{r\max}}{2a}[l_e C_{01}+r_x C_0-S_0(r_y-a)] \end{bmatrix}. \quad (7.22)$$

Now, the singular values of $\hat{\mathbf{J}}$ and corresponding vectors can be used to examine the effects of manipulator configuration on the ability of the system to achieve various end-effector velocities. *Table 7.1* lists a series of parameters which are typical of this application. The only unspecified parameters at this point are r_x, r_y and r_z, which specify the position of the robot base on the mobile platform.

Parameter	Value	Units	Source
l_1	0.254 (6.10)	m (in)	MFG Specifications
l_2	0.274 (6.11)	m (in)	MFG Specifications
l_3	0.228 (6.9)	m (in)	MFG Specifications
r	0.127 (6.5)	m (in)	(assumes 0.254 m wheels)
a	0.381 (6.15)	m (in)	(assumes 0.732 m wheel base)
ω_{1x}	3.729	rad/s	MFG Specifications
ω_{2x},ω_{3x}	6.521	rad/s	MFG Specification
ψ_{lx},ψ_{rx}	20.94	rad/s	MFG Specifications

Table 7.1: Parameter values for mobile robot.

Now consider the case where the wrist is at ground level (E_z = 0). This effectively constrains θ_2 and θ_3 of the manipulator. While θ_0 appears in the Jacobian, it does so in a symmetric fashion and hence, has no impact on the manipulability. Which makes sense intuitively.

In Figure 7.7, the major axes of the manipulability ellipse are shown for various poses of the manipulator, relative to the mobile platform where the manipulator is placed at the origin of the **{O}**-frame (i.e. r_x=r_y = 0). The (0,0) coordinate on the plot corresponds to the origin of the

{B}-frame, the manipulator base. The global x-direction (forward direction of the platform) is oriented vertically in the plot. The velocity scale of the ellipse axes is shown.

Examining Figure 7.7, several trends can be determined. First, the robot behavior is more isotropic as the reach is extended (as seen by the symmetric crosses formed by the axes at locations distal to the origin). Second, as the reach is reduced, and the manipulator is straight out in front of the platform (θ_1=0), the robot is capable of much larger speeds in the direction parallel to forward motion than normal to it (about a factor of 2).

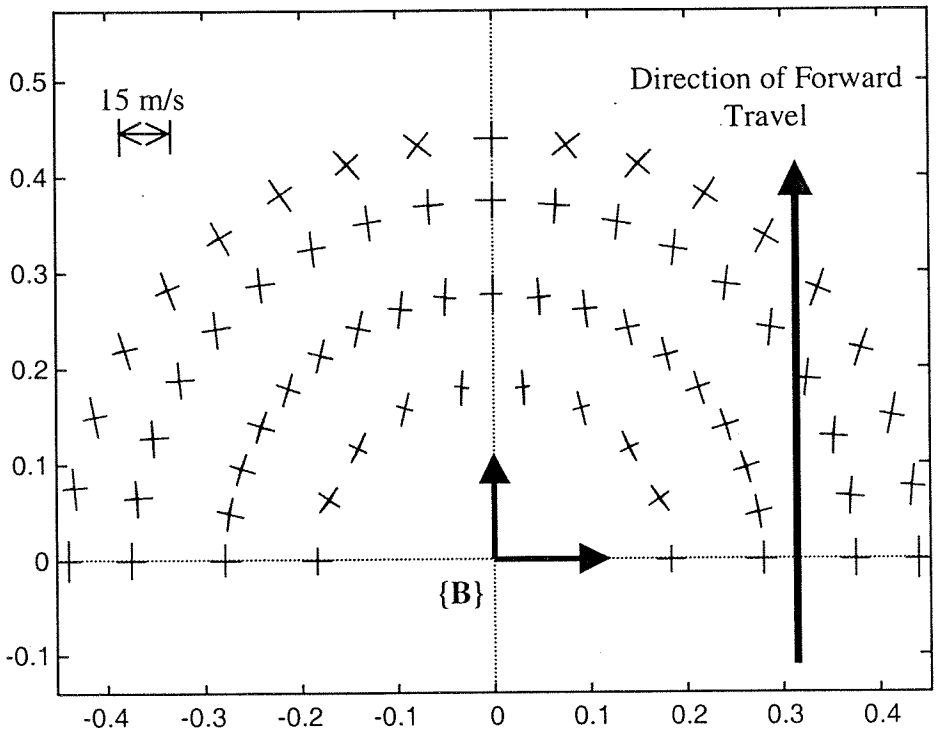

Figure 7.7: Manipulability plot for a 'slice' of the system workspace at z=0 and rx = ry = 0.

If the goal of this analysis is to chose a mounting position for the manipulator which maximizes the effectiveness of the robotic system to perform tasks on the highway surface, then the array of manipulability ellipses such as that shown in Figure 7.7 is an important visualization tool. In this case, we look for ellipses which have larger dimensions aligned with the down lane

velocity of the platform. This implies higher possible down-lane velocities. Figure 7.7 indicates, as one might expect, that mounting the manipulator on the front of the platform does not make best use of the robot's abilities.

Figure 7.8 is a composite of four plots of arrays of manipulability ellipses computed from the x-y plane Jacobian in Eqn (7.22). Figure 7.8a is the same as Figure 7.7, where the manipulator is mounted at the origin of the platform frame (at the midpoint on the axis of the driven wheels). Figures 7.8b-7.8d show how the manipulability changes as the manipulator is moved forward (along the local x-axis). The effect is most pronounced in Figure 7.8d where the manipulability ellipses are becoming elongated in the direction normal to the axis of motion. This is an undesirable characteristic since it does not allow use of the velocity capacity of the actuators in a way which increases potential down-lane velocity. The result is intuitively satisfying.

Figure 7.9 shows the manipulability arrays for four mounting locations on the side of the platform. Figure 7.9a represents the unlikely position of placing the manipulator very near the left-hand drive wheel. Figures 9b-9d show the arrays as the manipulator is moved forward by 0.12, 0.25 and 0.5 meters. Similarly, Figure 7.10 shows various locations on the side of the platform and to the rear of the drive wheel axis.

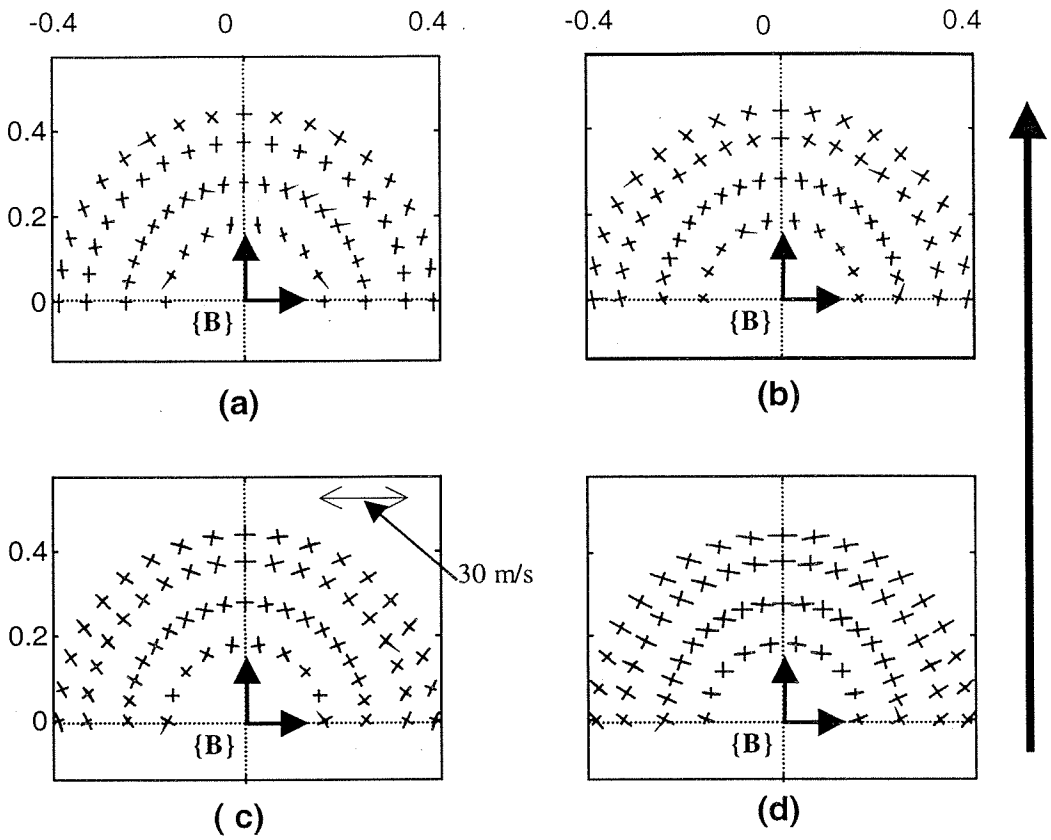

Figure 7.8: Manipulability Ellipse Array for the x-y plane of the manipulator platform combination for various mounting positions. Note the velocity scale for the ellipse axes. The arrow on the right indicates to direction of forward travel of the mobile platform. (a) $r_x = r_y = 0$; (b) $r_x = 0.12$ m, $r_y = 0$;(c) $r_x = 0.25$ m, $r_y = 0$; (d) $r_x = 0.5$ m, $r_y = 0$.

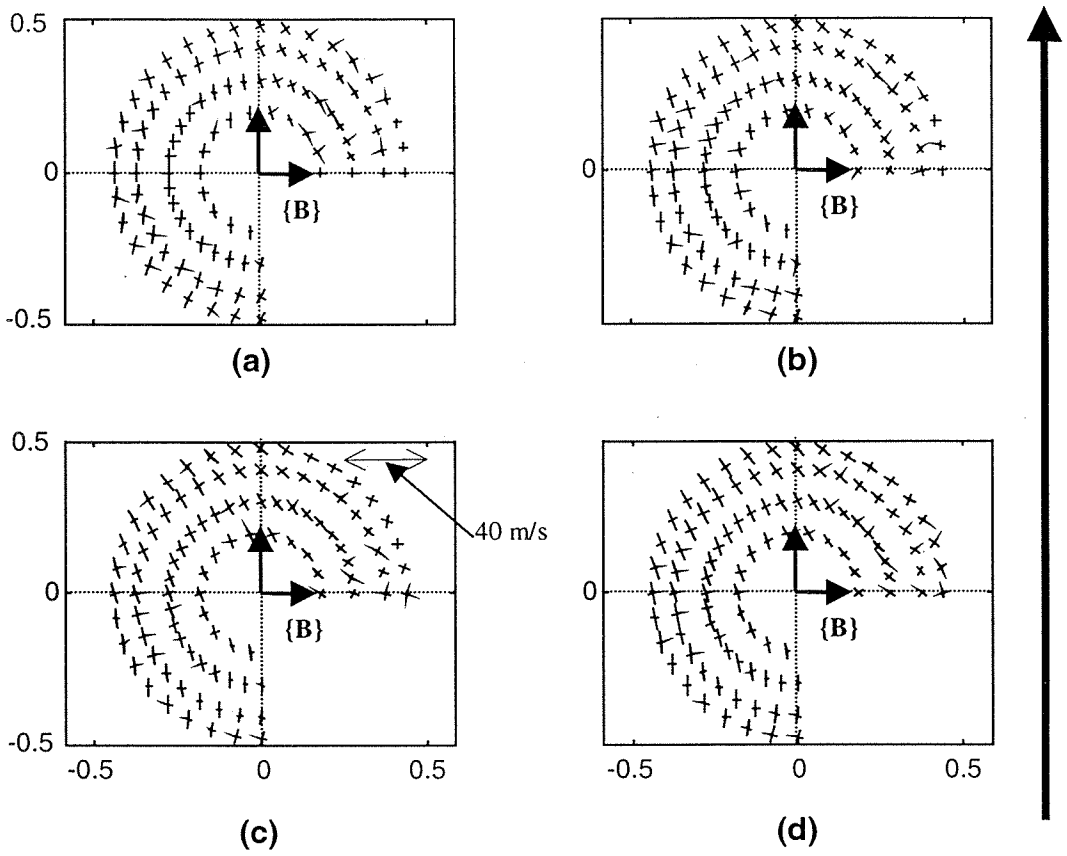

Figure 7.9: Manipulability Ellipse Array for the x-y plane of the manipulator platform combination for various mounting positions. Note the velocity scale for the ellipse axes. The arrow on the right indicates to direction of forward travel of the mobile platform. (a) rx =0, ry =0.5 m; (b) rx = 0.12 m, ry =0.5 m ;(c) rx =0.25 m, ry =0.5 m ; (d) rx = 0.5 m, ry =0.5 m .

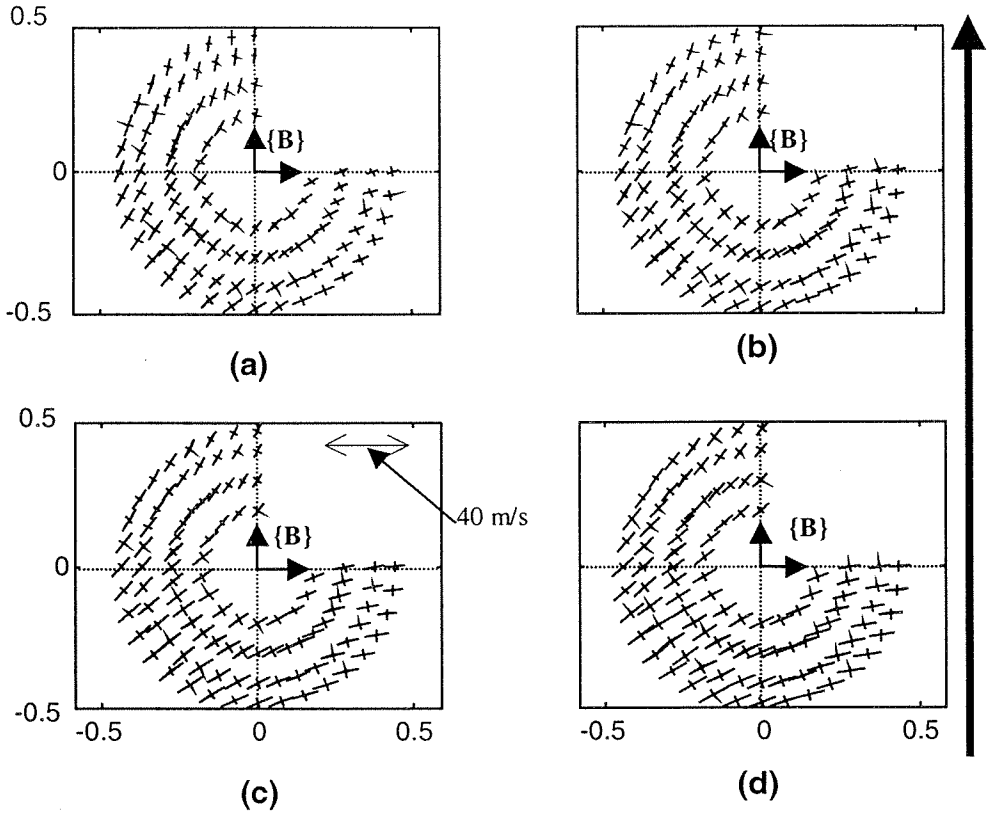

Figure 7.10: Manipulability Ellipse Array for the x-y plane of the manipulator platform combination for various mounting positions. Note the velocity scale for the ellipse axes. The arrow on the right indicates to direction of forward travel of the mobile platform. (a) rx =-0.5 m, ry =0.5 m; (b) rx = -0.65 m, ry =0.5 m;(c) rx = -0.85 m, ry =0.5 m ; (d) rx = - 2.0 m, ry=0.5 m.

7.7 Discussion of Results

The manipulability arrays shown in Figures 8-10 should be analyzed with an eye toward the intended task. If the mobile manipulator system is to be controlled in a coordinated fashion then it is important to have a high degree of mobility in the same direction as the down-lane velocity of the system. This will allow it to approach an intended target point on the roadway, place the tool there and keep the tool at the roadway while the platform maintains a nominal down-lane speed.

With this in mind, we should choose a mounting position which features an array of ellipses with long major axes oriented in the x-direction (which is vertical in Figures 7.8-7.10).

As discussed above, Figure 7.8 shows that placing the manipulator on the centerline of the platform is not very suitable. Note that the manipulability ranges from homogeneous when the manipulator lies on the axle (Figure 7.8a) to a situation which prefers motion orthogonal to the intended motion when the manipulator is extended out in front of the axle by 0.5 m (Figure 7.8d). The results are symmetric about the axle.

Figure 7.9 shows the most promising results. Ranging from a placement coincident with the left drive wheel (physically improbable) in Figure 7.9a to a point 0.5 m in front of the drive wheel in Figure 7.9d. Notice that the system shows preferable mobility in the down-lane direction for all of these positions, with the best location being the wheel position.

Figure 7.10 shows the arrays for a rear mounting position. Note that, while the major axes are considerably longer than those seen in previous figures, they are in the wrong direction.

In summary, we see the following trends:

- Mounting positions on the platform centerline lead to unsatisfactory results because the manipulator has either homogeneous mobility or preferable mobility in the direction orthogonal to the line of motion
- As we move further away from the axle along the centerline, the mobility along the down-lane direction gets worse.
- Placement of the manipulator along the axle, away from the centerline brings better mobility in the down-lane direction.
- These improved results are not as good as we move away from the axle.

The conclusion we reach is to place the manipulator as close as possible to the axle in the x-direction and as far as possible from the centerline in the y-direction. If we take the origin of **{O}** at the intersection of the centerline and the axle, then the manipulator base coordinates should be such that r_x is as small as possible and r_y is as large as possible.

7.8 Conclusions

This work presents a systematic, unified kinematic analysis for manipulator arms mounted on mobile platforms. The well known definition of manipulability is extended by scaling joint velocities by their maximum values. This unified approach to kinematics is essential for understanding the behavior of mobile robotic systems while performing highly coordinated tasks, such as those required of automated highway maintenance. Additionally, this approach offers tools that allow the designer more insight into the implications of geometric parameters. The method is illustrated by examining the effect of manipulator mounting position on the overall mobility of the system.

Chapter 8

Dynamic Modeling and Interaction Effects for Mobile Manipulators

8.1 Introduction

Mobile manipulators are comprised of robot manipulators mounted upon mobile platforms such as wheeled vehicles. Accordingly, mobile manipulators combine both high mobility and dexterous manipulation ability, and interest in the application of such manipulators is increasing significantly. Although considerable research and development has been performed in the area of motion control of mobile manipulators, most of the models developed in the previous work assume only planar motion and/or holonomic constraints in which the complexity of the modeling and control problem is often excessively simplified.

Recently Dugoff's pneumatic tire friction model (Dugoff et al., 1970) has been employed to describe the forces generated by the tires of wheeled mobile robots (Boyden and Velinsky 1994; Hong et al., 1999). In addition to experimentally verifying the dynamic model, it was shown that kinematic models are insufficient to capture the dynamics of such robots in high speed and/or high load applications. Accordingly, as the load and speed requirements for mobile manipulators increase to meet the demands of new applications, the efficacy of the existing models becomes questionable, and the need to include complex models arises to account for the wheeled platform's tire slip.

Secondly, much of the earlier work on mobile manipulators considers only kinematic coupling between the robotic manipulator and the platform which is sufficient for systems in which the platform is significantly more massive that the manipulator. However, this is not the general case. Joshi and Desrochers (1986) represented the motion due to the mobile platform by

an angular displacement (disturbance) to a two-linked arm. Their work took into account the effects of platform motion on the control of the robot arm relative to the platform. Liu and Lewis (1992) developed a robust controller for a mobile manipulator by considering the platform and the manipulator as two subsystems. Hootsmanns and Dubowsky (1991) developed the mobile manipulator jacobian transpose control algorithm which relies on vehicle motion sensing and the kinematic models of the system. Mobile manipulators with soft suspensions were shown to be stable with limited vehicle sensory data. Chung et al. (1998) developed the nonlinear interaction control algorithm for the redundant mobile manipulator subject to nonholonomic constraints to resolve the kinematic redundancy.

The motivation for much of other previous work, e.g., (Wiens 1989, Ghamsepoor and Sepehri 1995) stems from identifying the stability criteria so that the vehicle does not overturn. Most of the models described in the previous work (Joshi and Desrochers 1986, Liu and Lewis 1990, Hootsmanns and Dubowsky 1991, Chung et al., 1998) analyze the dynamic interaction in an explicit form. However, they have only planar motion and/or satisfy the assumption of nonholonomic motion which is far from realistic in practice.

In this work, we develop the equations of motion of a mobile manipulator system using a Newton-Euler formulation. This model incorporates a complex tire model which accounts for tire slip and is thus applicable to high speed and high load applications. The model is then systematically exercised to examine the dynamic interaction effects between the mobile platform and the robot manipulator, to illustrate the effects of wheel slip on system performance, and to help understand the efficacy of kinematically coupled models.

8.2 Analysis

Figure 1 shows a simple mobile manipulator that is used for the purposes of this work. This system is comprised of a differentially steered wheeled mobile robot as the mobile platform and a single link for the manipulator arm. The system is based on an actual mobile manipulator under development by the authors that actually has a six degree of freedom robotic manipulator. The single link arm is used herein to greatly simplify the modeling effort and to more simply illustrate the interaction effects. A complete dynamic model of the actual system is under development.

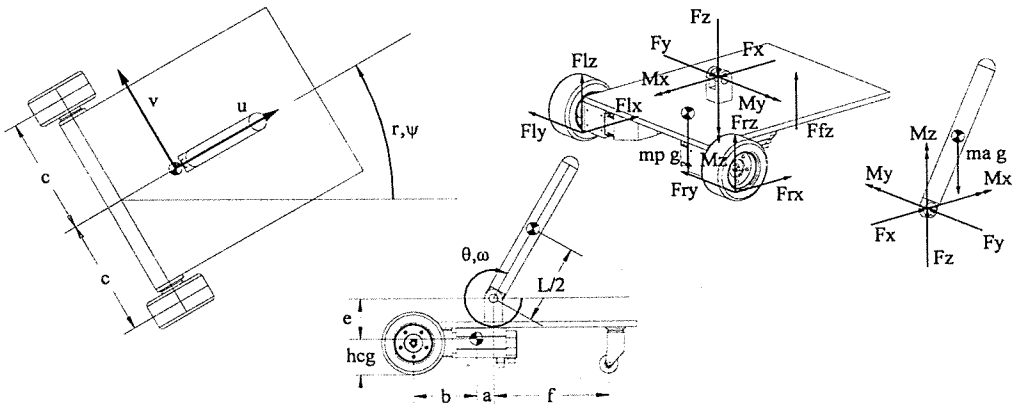

Figure 8.1: Schematic of the simple mobile manipulator system.

To analyze the mobile manipulator, it is separated into its two components, the arm and the platform. Several simplifying assumptions are then employed as follows. The platform is constrained against roll, pitch, and bounce although weight transfer is accounted for. The three degrees of freedom are displacement in the global X-Y plane and orientation. The platform is assumed symmetric about the x-z plane so that $I_{xy} = I_{yz} = I_{yx} = I_{zy} = 0$. Additionally, it is assumed that $I_{xz} = I_{zx}$ is adequately small to be neglected.

The general equations for rigid body motion of the system expressed in a body fixed coordinate system are written in the form

$$\sum \mathbf{F} = m\frac{d}{dt}\mathbf{v}\Big|_{xyz} + \boldsymbol{\Omega}_{xyz} \times m\mathbf{v} \tag{8.1}$$

and

$$\sum \mathbf{M} = \mathbf{I}\frac{d}{dt}\boldsymbol{\Omega}\Big|_{xyz} + \boldsymbol{\Omega}_{xyz} \times \mathbf{I}\boldsymbol{\Omega}_{xyz} \tag{8.2}$$

where F and M are the forces and moments acting on the body, m is the body mass; I is the inertia matrix; v and Ω are vectors expressing the total linear and angular velocities of the rigid body of interest and $\frac{d}{dt}\mathbf{v}\Big|_{xyz}$ and $\frac{d}{dt}\boldsymbol{\Omega}\Big|_{xyz}$ are the derivatives of these vectors with respect to the body centered coordinate system.

Utilizing the above assumptions, the body fixed coordinates align along the platform's principal axes, and summing the moments and forces for the platform yields:

$$\begin{bmatrix} h_{cg}\left(F_{ry}+F_{ly}\right)+c\left(F_{lz}-F_{rz}\right)+eF_y-M_y \\ b\left(F_{lz}+F_{rz}\right)-h_{cg}\left(F_{rx}+F_{lx}\right)-eF_x+aF_z+\left(a+f\right)F_{fz}-M_y \\ c\left(F_{rx}-F_{lx}\right)-b\left(F_{ry}+F_{ly}\right)-aF_y-M_z \end{bmatrix} = \begin{bmatrix} 0 \\ 0 \\ I_{P3}\dot{r} \end{bmatrix} \tag{8.3}$$

$$\text{and} \begin{bmatrix} -F_x+F_{rx}+F_{lx} \\ -F_y+F_{ry}+F_{ly} \\ -F_z+F_{rz}+F_{lz}+F_{fz}-m_Pg \end{bmatrix} = \begin{bmatrix} m_P\left(\dot{u}-rv\right) \\ m_P\left(\dot{v}+ru\right) \\ 0 \end{bmatrix} \tag{8.4}$$

where a, b, c, e, f, and h_{cg} are geometric terms as shown in Figure 1. I_{P3} and m_P are the platform's inertia about the vertical axis and its mass. F_x, F_y, F_z, M_x, and M_z are the pivot joint reactive forces and moments. F_{lz}, F_{rz}, and F_{fz} are the normal forces on the tires due to gravity and weight transfer for, respectively, the left wheel, right wheel and front caster. F_{lx} and F_{ly} are the tire generated forces for the left wheel in the x and y directions and similarly, the right wheel forces are F_{rx} and F_{ry}. The velocities and accelerations for the platform's center of mass are: u

and $\dot{u}$ for longitudinal motion and v and $\dot{v}$ for lateral motion. The angular velocity and acceleration of the platform are r and $\dot{r}$.

The single link manipulator is modeled as a slender rod whose moment of inertia about its longitudinal axis is zero. To derive the equations of motion for the arm, a kinematic constraint is imposed that forces the velocity of the pivot point to be the same for both subsystems. Additionally, it is noted that the total angular velocity of the arm is the sum of the angular velocity of the platform in the world frame and the angular velocity of the arm in the platform frame. Through the kinematic constraint, the velocities of the arm are expressed in terms of the three velocities of the platform, u, v, and r and the rotational velocity of the arm with respect to the platform, ω.

The arm's equations of motion expressed in the platform's body centered coordinates are:

$$\begin{bmatrix} F_x \\ F_y \\ F_z c - m_A g \end{bmatrix} = \begin{bmatrix} m_A\left(\dot{u} - \dot{\omega}\frac{1}{2}L\sin\theta - r^2\left(a + \frac{1}{2}L\cos\theta\right) - \omega^2\frac{1}{2}L\cos\theta - rv\right) \\ m_A\left(\dot{v} + \dot{r}\left(\frac{1}{2}L\cos\theta + a\right) + r\left(u - L\omega\sin\theta\right)\right) \\ m_A\frac{1}{2}\left(\omega^2 L\sin\theta - \dot{\omega}L\cos\theta\right) \end{bmatrix} \tag{8.5}$$

and

$$\begin{bmatrix} M_x\cos\theta - M_z\sin\theta \\ M_y + F_x\frac{1}{2}L\sin\theta + F_z\frac{1}{2}L\cos\theta \\ M_x\sin\theta + M_z\cos\theta - \frac{1}{2}LF_y \end{bmatrix} = \begin{bmatrix} 0 \\ I_A\left(\dot{\omega} + r^2\sin\theta\cos\theta\right) \\ I_A\left(\dot{r}\cos\theta - 2r\omega\sin\theta\right) \end{bmatrix} \tag{8.5}$$

where I_A is the arm moment of inertia about any axis that passes through its center of mass and is perpendicular to its longitudinal axis; m_A is the arm mass and L is it length. The angular displacement, velocity and acceleration of the arm with respect to the platform are denoted θ, ω, and $\dot{\omega}$.

Equations (3) – (6) provide 12 equations in 12 unknowns. The unknowns, in row vector, are: $\begin{pmatrix} F_x & F_y & F_z & M_x & M_z & \dot{u} & \dot{v} & \dot{r} & \dot{\omega} & F_{lz} & F_{rz} & F_{fz} \end{pmatrix}$. The solution provides the joint reactive forces, the weight transfer, and the equations of state.

8.3 Results and Discussion

To examine the dynamic interaction between the motion of an arm mass and a platform without a control law or feedback, the model was allowed to operate with the arm freely swinging beneath the platform as a pendulum. The tire model employed was Dugoff's. Numerous series of simulations were performed. Each series consisted of adjusting the arm mass properties from its total mass and its total moment of inertia, to one half, one fourth, one eighth, one sixteenth, and none of it total mass and total moment of inertia. To maintain a constant total for the mobile manipulator, the platform mass properties were increased by the same amounts as the reductions made in the arm. Each series started with the system at rest and the arm hanging at an initial position of 45° from vertical. For each series, the left and right wheels were given step inputs, at t=0, of differing magnitudes. Table 1 provides a list of system parameters employed.

a, CG to pivot point (x-direction)	0.064 [m]
b, CG to axle midpoint (x-direction)	1.10 [m]
c, one-half of the track width	0.464 [m]
e, CG to pivot point (z-direction)	0.113 [m]
f, pivot point to front axle (x-direction)	0.873 [m]
h_{cg}, ground to CG (z-direction)	0.165 [m]
L, arm length	0.648 [m]
m_a, Arm mass	32.7 [kg]
m_p, Platform mass	112 [kg]
I_A, Arm moment of inertia	1.19 [kg m^2]
I_{P3}, Platform yaw moment of inertia	18.3 [kg m^2]
C_x, Longitudinal tire stiffness	6000 [N/unit slip]
C_y, Lateral tire stiffness	6000 [N/rad]

Table 8.1: Parameter Values for Mobile Manipulator.

Figures 8.2 – 8.5 provide a sample of the results obtained through the simulation. These results are for the series in which the rotational velocities for the left and right wheels are 10.0 and 13.0 rad/s, respectively. Note that the term, full denotes arm inertial properties as listed in Table 8.1 whereas ¼, half, etc. denote properties adjusted to that fraction of the original.

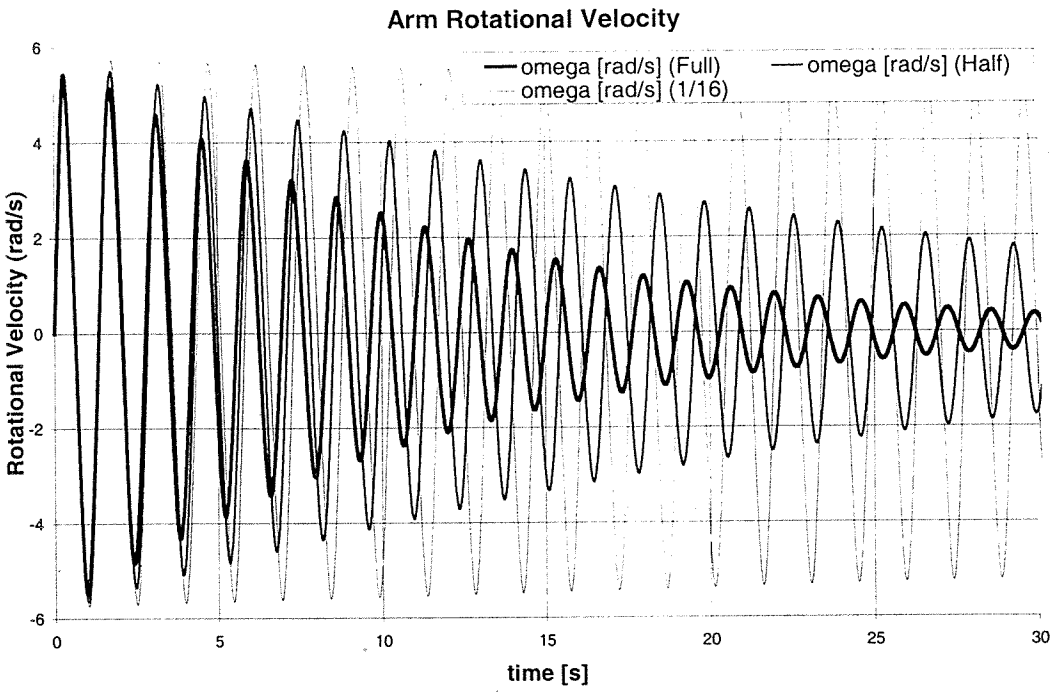

Figure 8.2: Arm Rotational Velocity

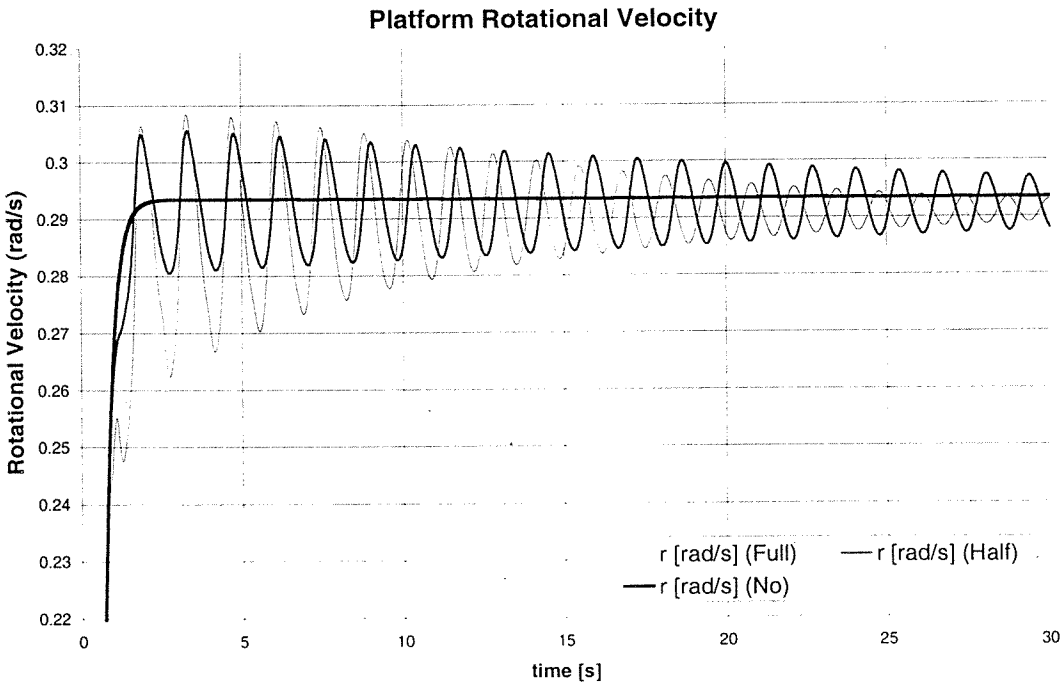

Figure 8.3: Platform Rotational Velocity

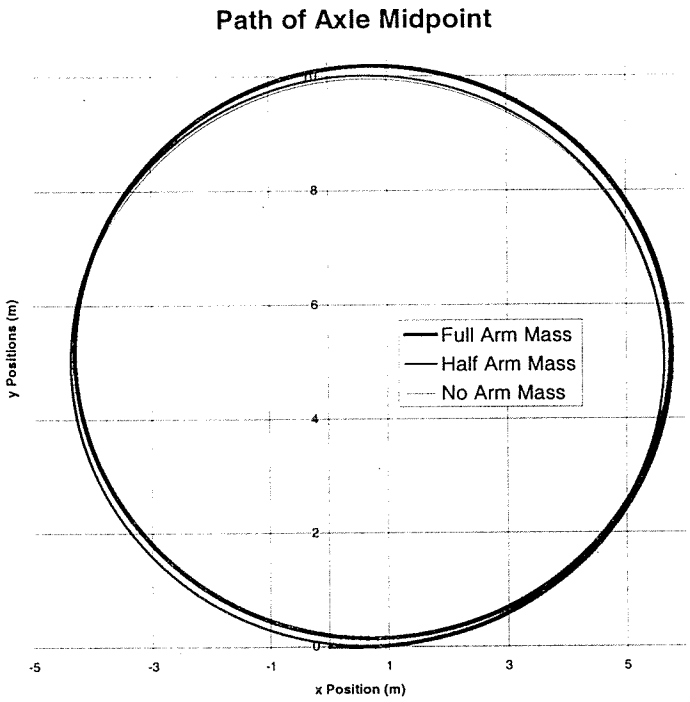

Figure 8.4: Path of Axle Midpoint

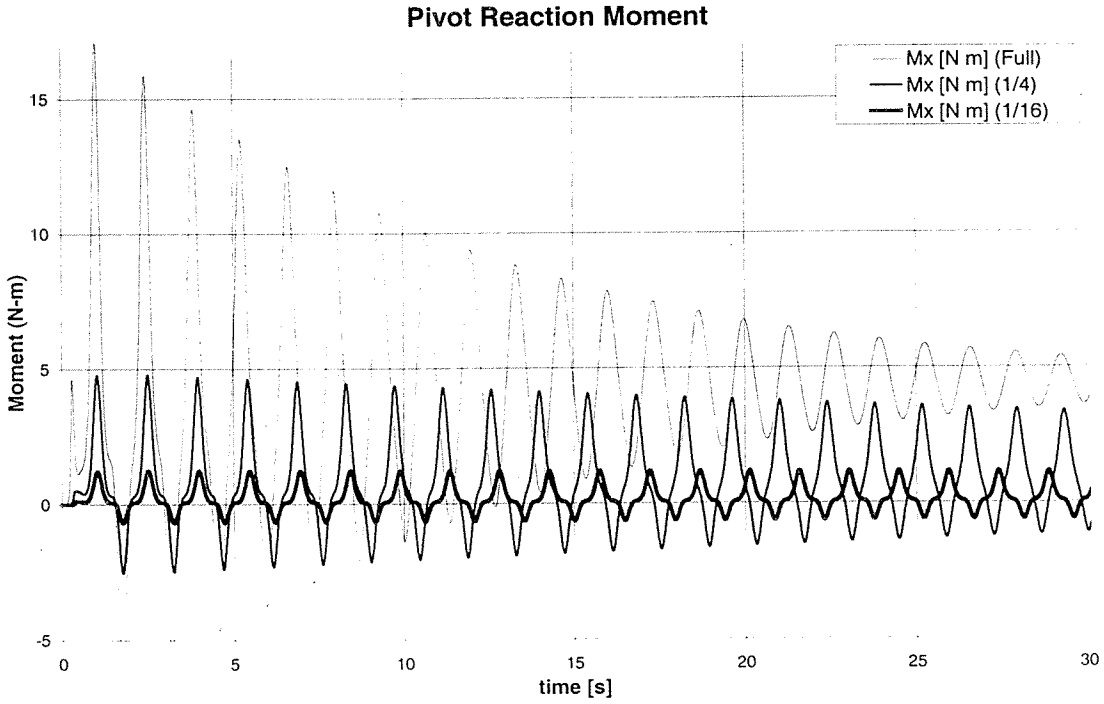

Figure 8.5: Pivot Reaction Moments

The figures clearly illustrate that the motion of the arm mass affects the behavior of the platform. Basically the motion of the arm causes the following: (1) weight transfer between the front caster and the drive wheels, (2) weight transfer between the drive wheels, (3) lateral, longitudinal, and vertical forces acting at the pivot point, and (4) yaw and roll moments acting at the pivot point. The roll moment variation at the pivot is illustrated in Figure 8.5. This moment, along with the dynamic interaction forces contribute to the weight transfer which results in variations of the tire normal forces. These variations greatly affect the driving and cornering forces developed by the tire. Furthermore, these pivot point reactive forces cause both platform forward speed variations and lateral speed changes. The principal frequency of these variations is the same as that of the arm oscillations, as shown in Figure 8.2, and diminishes as the rotational velocity of the arm decays. This oscillation also manifests itself in the yaw rate. Figure 8.3 shows the yaw rate for the platform varying arm mass. The orientation of the arm also causes a variation in the effective moment of inertia of the mobile manipulator about its center of mass as well as the location of its center of mass. Finally, the path is determined by the lateral, longitudinal, and rotation velocities of the platform. As these are so heavily affected by the motion of the arm mass, the path is likewise altered as is illustrated in Fig. 8.4.

8.4 Conclusions

In this work, the equations of motion for a simplified model of a mobile manipulator have been developed. The model is unique in its incorporation of a complex tire model to account for the tire-ground interface in a realistic manner. This allows for consideration of such important aspects as tire slip and weight transfer effects. Equations for the joint reactive forces and moments permit analysis of the coupling between the arm and the platform of the mobile

manipulator. The model has been systematically exercised and results presented. A simplified model has been used to avoid use of a control law and focus on dynamic interaction effects alone. The results clearly show the importance of considering dynamic interactions for manipulator arms with any significant inertia relative to the platform. Furthermore, the dissipative nature of tire slip is captured through the empirical tire model, and this is illustrated through the damped system response.

Chapter 9

Coordination Control of a Human/Manipulator System

9.1 Introduction

Many manipulation tasks cannot be performed using a single robot manipulator or the performance of the manipulation process can be improved by multiple robot manipulators. However, due to complexity of the coordination mechanisms and the current robot technology, multiple coordinated robot manipulators can only perform simple tasks in a well designed environment (Luh and Zheng, 1987; Zheng and Luh, 1985; Xi, et al., 1993). Therefore, a human/manipulator coordination is a new and attractive use of robot manipulators where two coordinated manipulators are necessary but lacking intelligent capability to perform given tasks.

Much research has been done on mechanical systems with human-robot interaction, such as Hardyman, a master-slave manipulator system, a robot for man-robot cooperation, an Extender, etc. Hirzinger and Landzettel (1985) proposed a direct teaching method of a manipulator using a force sensor mounted on a robot. Fukuda et al. (1990) have proposed a manipulator, which is designed for handling heavy objects in cooperation with a human operator (Fukuda, et al., 1990; Fukuda and Fujisawa, 1991). Kazerooni (1990) has proposed the extender or the manipulator system to extend the strength of the human arm; he has designed a control algorithm, so that the force augmentation ratio could be specified, based on the modeling of the system including the human operator and the environment.

In this chapter, two new types of coordination control called operator manipulator coordination control (OMCC) will be developed. One is based on compliance control and the other explicit force control. Therefore, implicit in the human assisted scheme is force feedback

and control. In either case, the primary goal is the development of technology to constitute a robotic human assist system to allow an individual worker to accomplish tasks with which the size of the workpiece is too large or heavy for an unassisted worker to handle. The implementation of force control allows the manipulator to operate effectively while the end effector, or an object that the end effector is holding, is in contact with the environment. Such feedback permits decisions to be made about lifting location and force, as might be used in human assisted operations. It also provides for the proper application of force during independent functions, such as grinding, cleaning, or assembling.

In OMCC, the human operator takes the lead of a task execution. The task trajectory can be applied arbitrarily by the operator. Therefore, the problem in the operator-manipulator coordination is how to make the robot understand the motion intention and planning of the human operator. In this scheme, H-infinity optimal controller will be integrated with classical impedance control or explicit force control to improve and robustify the closed-loop performance that might be degraded due to the disturbances applied by a human operator. A previously developed impedance model of the dynamics of the human arm (Dolan, et al., 1993) will be adopted to this work.

The operator arm will exert a force on the manipulator to initiate a task.. By using a compliant control, the manipulator will also then move. However, it is believed that the impedance of the human arm is not constant and the weight of an object may be unknown to the manipulator which create problems in the compliant motion control. One way to improve the coordination performance is to add an additional position feedback loop and design a robust controller that modifies the reference trajectory or the feedforward force. This control configuration makes implementation of OMCC feasible for many commercially available robots.

The proposed control systems consist of two controllers: one generates the compliant motion of the robotic manipulator based on the force applied to the system, and the other controls the interaction between the system and the human operator which is modeled as the time-varying environment. The developed algorithms are applied to a planar link mechanism with one degree of freedom. The simulation results illustrate the effectiveness of the proposed control algorithm.

9.2 Position-Based Control

An impedance control relies on accurate position control of the manipulator as a basis. The impedance control is added as an additional control loop around the position controlled manipulator (Lawrence, 1988). The detailed treatment of the simplified linear model employed in this work can be also found in Lawrence (1988).

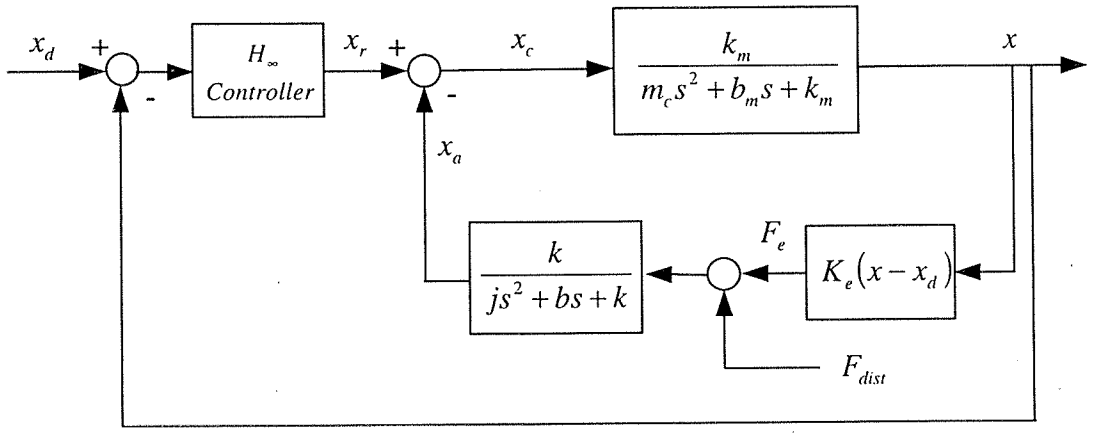

Figure 9.1: Robust position-based OMCC

In this approach, the manipulator is controlled to provide an impedance specification by treating the mechanism either as an actuator of position or an actuator of force and torque. For the position–based approach, forces and torques are sensed explicitly via a wrist force/torque sensor, and the position commands are issued to the inner loop controller. In particular, the position adjustment vector is created by filtering the measured interaction forces and torques F to satisfy

$$F = KX_a + B\dot{X}_a + J\ddot{X}_a \tag{9.1}$$

via

$$X_a(s) = \left[K + Bs + Js^2\right]^{-1} F(s) \tag{9.2}$$

With the simplification of diagonal K, B, and J, this reduces to a second order low pass filter for each component of F to generate the respective components of X_a. The adjustment X_a is added to the nominal trajectory command X_0 to generate the overall position command X_c:

$$X_c = X + X_a \tag{9.3}$$

In addition to the nominal impedance control, a H_∞- prefilter is designed to improve the control performance especially for the interaction with a human operator. As seen in Figure 9.1, the force disturbance applied by an operator is added in addition to the nominal force feedback loop.

Note that in this approach , it is assumed that there is a action planner which modifies the reference trajectory of the manipulator such a way that human intention can be integrated as in Xi and Tarn (1998). Similar approach will be pursued in the future utilizing classical impedance control combined with H_∞- prefilter.

9.3 Explicit Force-Based Control

Explicit force control involves the direct command and measurement of force values, with the goal of having the output follow the input as closely as possible. Two types of explicit force control have been proposed: force based, and inner position loop based. By far, the force based techniques usually employ some form of PID control, as well as various simple forms of filtering. Inner position loop controllers, as the name suggests, have an outer force control loop that provides position commands to an inner position based controller. However, it has been shown in a previous analysis that the inner position loop controllers can also be viewed as force based controller (Volpe and Khosla, 1992)..

Explicit force control describes a strategy that compares the reference and measured force signals, process them, and provides an actuation signal directly to the plant. The reference force may also be fedforward and added to the signal going to the plant. In general, an explicit force control system consists of a plant, a controller, and a feedforward transfer function, and a force feedback filter. Active damping, if present, is included in the plant. The controller is usually some subset of PID control.

It is assumed that the human operator moves at a reasonably slow speed such that the contact point with the object is always located within the workspace of the manipulator. It can be easily seen that position control is not a suitable choice for the current objective since any position error may result in a separation or cause a large contact force. Here we adopt a variation of the hybrid control control scheme proposed by Raibert and Craig (1981). In this approach that utilizes explicit forces, the exact geometry of the surface of the moving object is not required. The surface is only assumed to be smooth and convex.

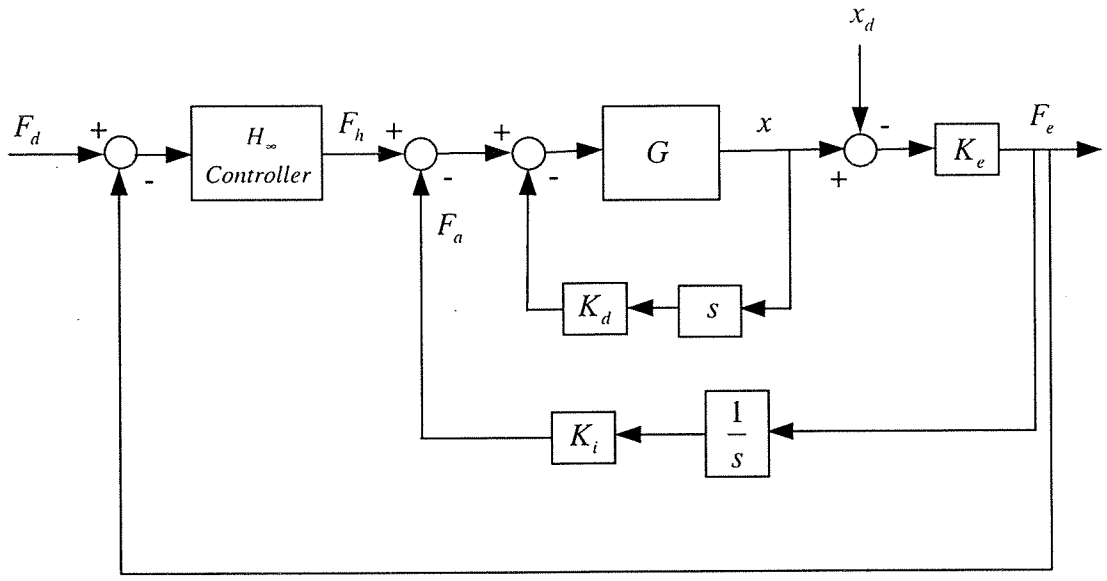

Figure 9.2: Robust explicit force-based OMCC

We apply the following explicit force control law.

$$m\ddot{x} = F_d - K_i \int F_e dt - K_d \dot{x} \tag{9.4}$$

The integral control was chosen due to its characteristics of a zero steady state error and a low-pass filter when a small gain is used (Volpe and Khosla, 1992). The active damping term is very effective to maintain stable contact and avoid bounces and (Khatib and Burdick, 1986). The force feedforward term or the desired contact force is set to zero. As seen in the Figure 9.2, H_∞ controller operates on the force error to modify the reference force trajectory based on the force error. Note that the trajectory applied by the human operator is injected to the loop to generate the contact force.

$$m\ddot{x} = \Im_{H_\infty}[F_d - F_e] + F_d - K_i \int F_e dt - K_d \dot{x} \tag{9.5}$$

9.4 H_∞ Controller Design

In this section the H_∞ controller design process is briefly described. The goal in robust control system design is to synthesize a controller which maintains system response and error signals within tolerances despite the effects of uncertainty on the system. Uncertainty, can take many forms, however, the most significant are noise/disturbances and modeling errors. Therefore, uncertainty is by far the most significant issue in controller design. H_∞ theory provides a direct reliable procedure for synthesizing a controller which optimally satisfies singular value specifications.

The H_∞ augmented plant is shown in Figure 9.3 with G_A described by

$$\dot{x} = Ax + B_1 w + B_2 u \tag{9.6}$$

$$z = C_1 x + D_{11} w + D_{12} u \tag{9.7}$$

$$y = C_2 x + D_{21} w + D_{22} u \tag{9.8}$$

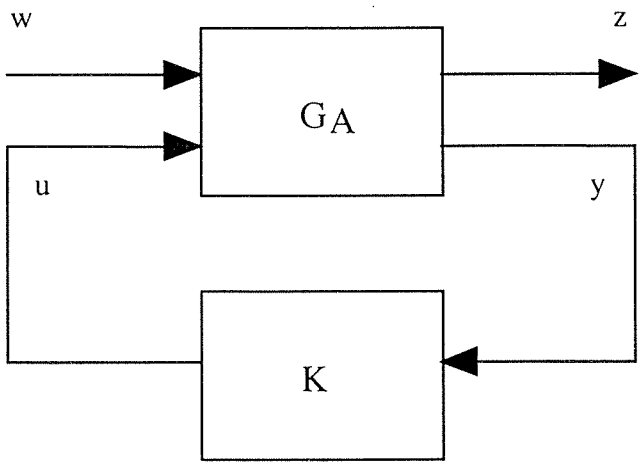

Figure 9.3: Augmented plant and controller for H_∞ design

The variable w represents process and sensor noise, z is the regulated variable and y is the input to the controller. G_A is called the coefficient matrix for the linear fractional transformation (LFT). The H_∞ design process will minimize the maximum norm of the H_∞ optimal control cost function T_{zw}, $\|T_{zw}\|_\infty$ by the appropriate choice of controller K, where

$$T_{zw} = \begin{bmatrix} W_1 S \\ W_2 KS \\ W_3 T \end{bmatrix} \tag{9.9}$$

The weighting functions W_1,W_2 and W_3 are chosen to reflect the design objectives. The original plant G_p is augmented with W_1,W_2 and W_3 to give G_A. The weighting functions are not completely arbitrary, as they are subject to some constraints. The H_∞ theory gives four conditions (constraints) for the existence of a solution to the standard H_∞ control problem and are stated as follows:

1. D_{11} small enough. There must exist a constant feedback control law F(s)= "constant matrix" such that the closed loop D matrix satisfies $\overline{\sigma}(D) < 1$,

2. Control Riccati $P \geq 0$. The H_∞ full-state feedback control Riccati equation must have real, positive semidefinite solution P,

3. Observer Riccati $S \geq 0$. The Riccati equation associated with the observer dual of the H_∞ full-state feedback control problem must have real, positive semidefinite solution S, and

4. $\lambda_{\max}(PS) < 1$. The greatest eigenvalue of the product of the two Riccati equation solutions must be less than one.

These four conditions must hold for there to exist a feedback control law which solves the standard H_∞ control problem.

The following weighting functions are selected in OMCC:

Position-based OMCC

$$W_1 = \frac{100(1+0.005s)^2}{(1+0.2s)(1+0.001s)}$$

$$W_3 = \frac{s^2}{50000}$$

Explicit force-based OMCC

$$W_1 = \frac{150(1+0.05s)^2}{(1+0.2s)(1+0.008s)}$$

$$W_3 = \frac{s^2}{40000}$$

9.5 Simulation –Position-Based OMCC

The developed method has been applied to a single link manipulator. The parameters used in the simulation are as follows:

$$I = 20Kg \bullet m^2,\ m = 20Kg,\ \text{and}\ L = 0.5m$$

where I, m, and L are the moment of, the mass and the length of the robot manipulator, respectively. In the simulation, the robot manipulator is commanded to track the following reference trajectories in task :

$$x_d = \begin{cases} -0.05\sin\left(\frac{\pi t}{5}\right), & 0 \le t < 5 \\ 0.0606 + 0.07\sin\left(\frac{\pi t}{3}\right), & 5 \le t < 15 \\ 0.0606 + 0.05\sin\left(\frac{\pi t}{5}\right), & t \ge 15 \end{cases}$$

The feedback gains for the nominal controller are $K_p = 50$ and $K_d = 10$.

The actual human/manipulator coordination is simulated by applying a discontinuous trajectory and adding the disturbance force applied by an operator. Practically, as seen in Figure 9.1, H_∞ controller acts as a prefilter operating on the position error, which, in turn, modifies the reference trajectory for the impedance control system in the inner closed loop.

Figures 9.5 - 9 show the tracking performance of classical impedance control under the influence of the external disturbance force. Figures 9.10 - 14 demonstrate the results of the developed robust position-based control simulation.

It is obvious that the robust controller outperforms the impedance controller by comparing Figure 9.5 and 9.6 with Figure 9.10 and 9.11. However, both controllers demonstrate similar performance in terms of the reaction force detected by the force sensor and the trajectory correction performed by the impedance controller.

9.6 Simulation – Explicit Force-Based OMCC

In the simulation, the human operator leads the manipulator to track the following reference trajectories in task space:

$$x_d = 0.1\sin\left(\frac{t}{10}\right).$$

As in position-based coordination, H_∞ controller operates on the force error to modify the feedforward.

Figures 9.15 – 18 depict the control performance of OMCC using the integral control. Figures 9.19 – 22 show the control performance of the robust force-based OMCC using H_∞ optimal control theory.

It is not difficult to see the superior tracking performance of the robust OMCC over the integral control by comparing Figure 9.15 and 9.19. In Figure 9.19, the actual trajectory is almost identical to the reference trajectory as opposed to the plots in Figure 9.15. Note that Figure 9.15 represents the tracking performance of the integral control with best tuned feedback gains. The feedback gains for the integral control are $K_i = 15$ and $K_d = 385$. Figure 9.17 and 21 deliver very important information about the coordination performance of the controllers. It is well understood in explicit force-based OMCC that a good controller should be able to regulate the reaction force close enough to zero between the human operator and the robotic manipulator. Figure 9.17 and 21 demonstrate the force regulation performance of the integral control and the robust force control, respectively. It is observed in Figure 9.21 that the reaction force is bounded to a very small value so that smooth coordination between the human operator and the manipulator can be achieved. In contrast, the integral controller is unable to maintain the

reaction force within an acceptable range. Also, it is evident from Figure 9.18 and 22 that the control effort of the robust controller is even smaller than that of the integral controller.

9.6 Conclusions

A new robust coordination control for a human\manipulator system was developed based on the integral control utilizing H_∞ optimal control theory and demonstrated in computer simulation. The simulation results showed excellent force regulation and tracking performance of the developed controller. Future work will focus on extending the technique to general multi-input multi-output systems and implementing the new control law.

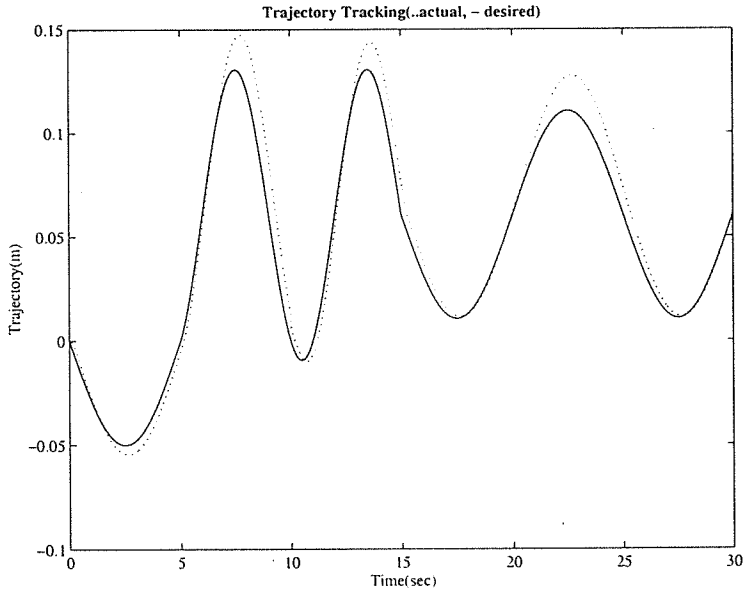

Figure 9.4: Position-based OMCC: trajectory tracking in task space

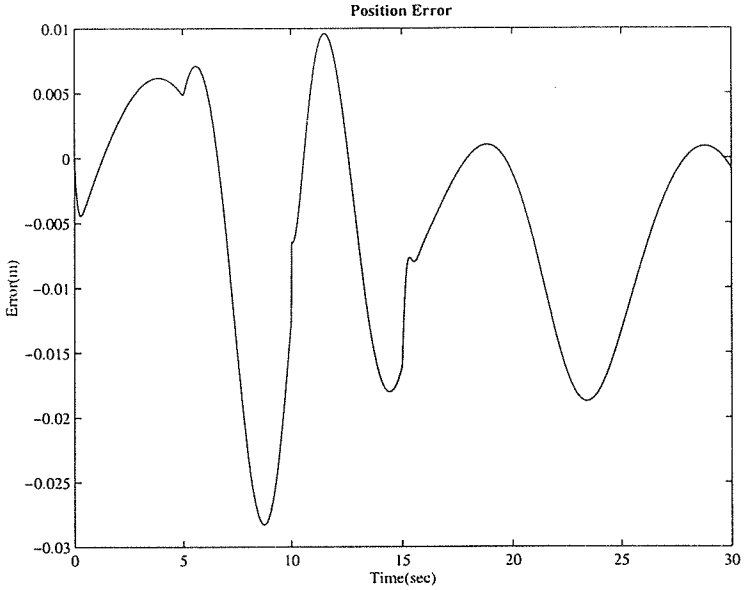

Figure 9.5: Position-based OMCC: position error

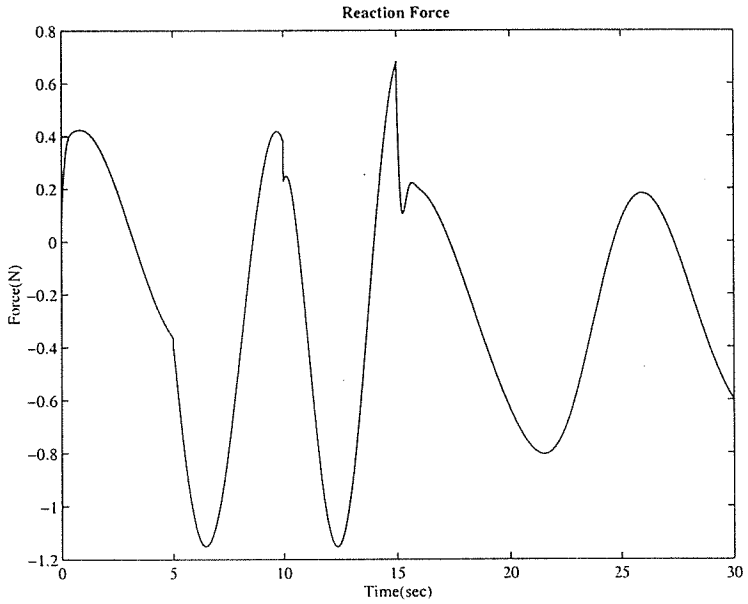

Figure 9.6: Position-based OMCC: reaction force

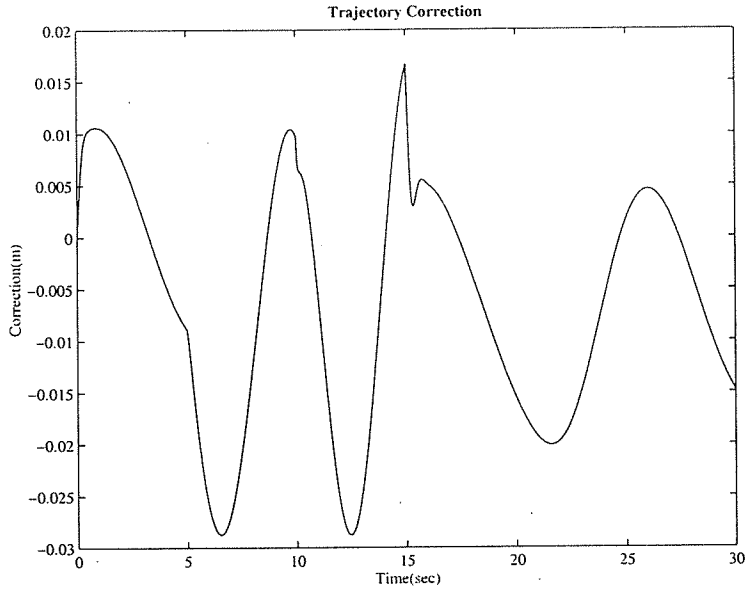

Figure 9.7: Position-based OMCC: trajectory correction

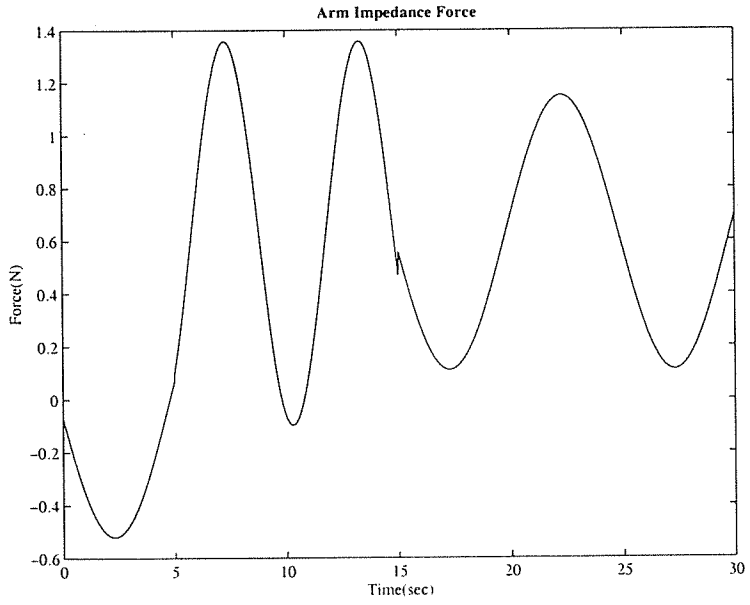

Figure 9.8: Position-based OMCC: arm impedance force

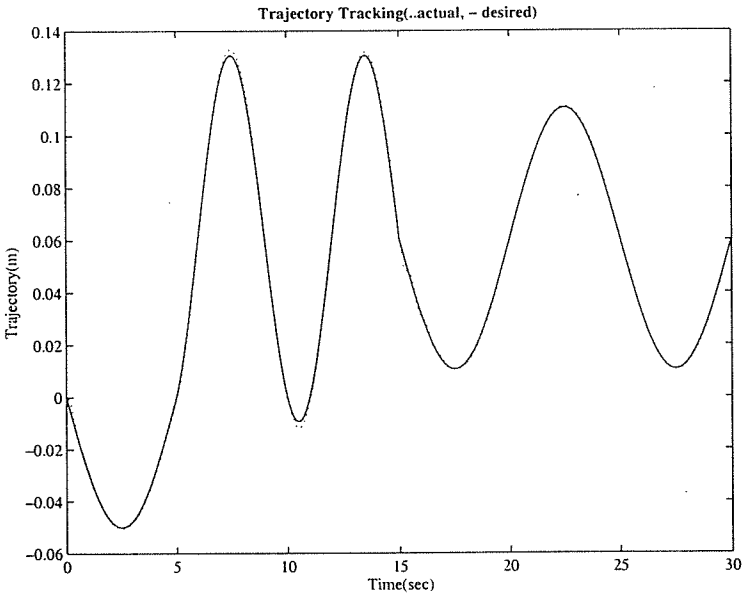

Figure 9.9: Robust position-based OMCC: trajectory tracking in task space

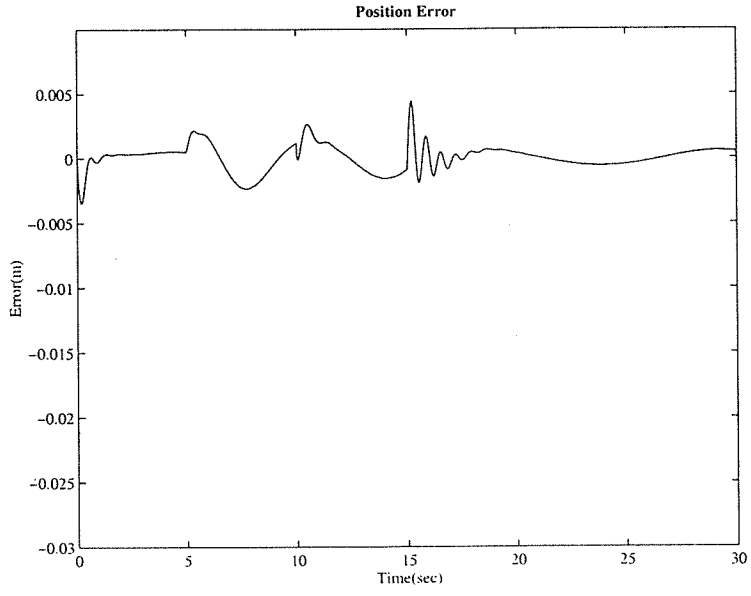

Figure 9.10: Robust position-based OMCC: position error

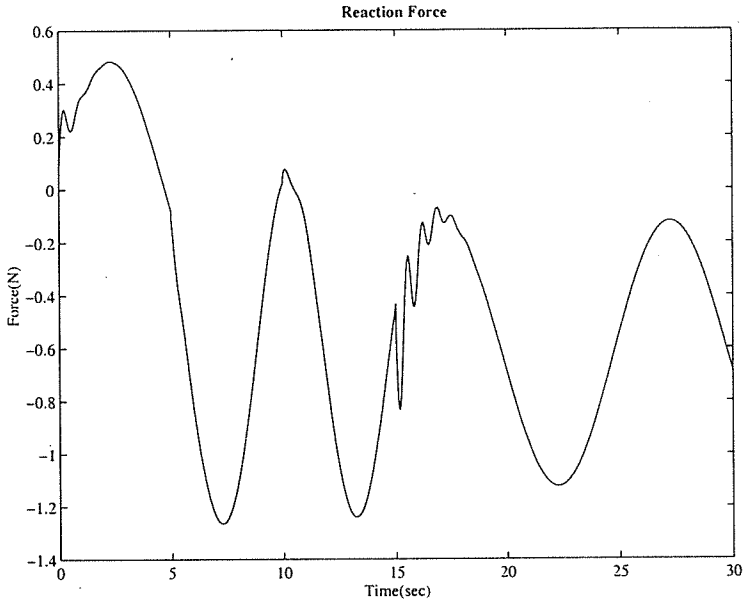

Figure 9.11: Robust position-based OMCC: reaction force

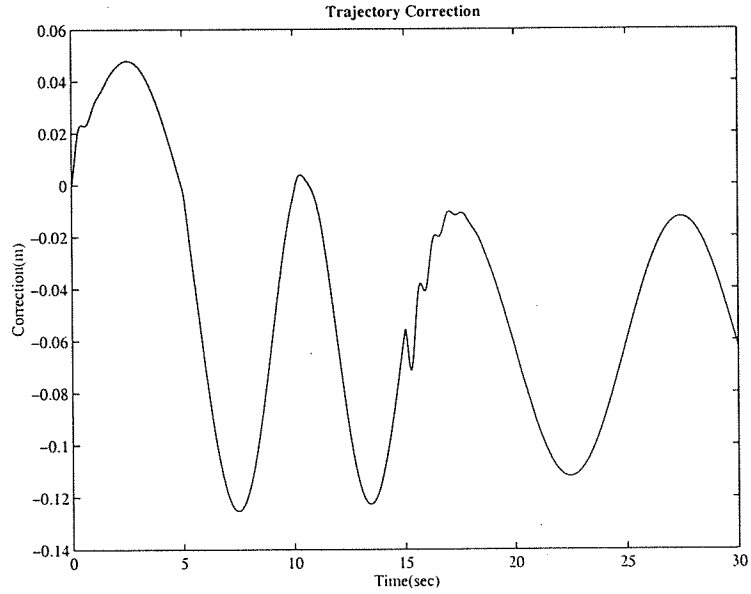

Figure 9.12: Robust position-based OMCC: trajectory correction

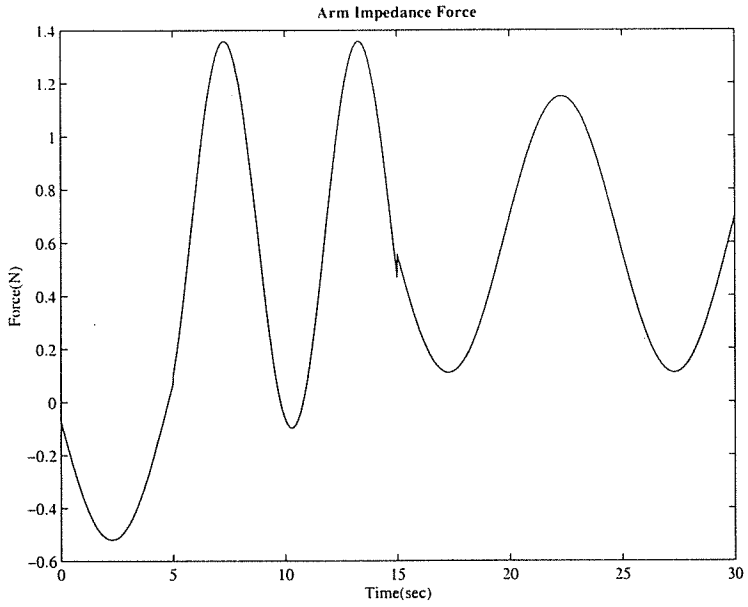

Figure 9.13: Robust position-based OMCC: arm impedance force

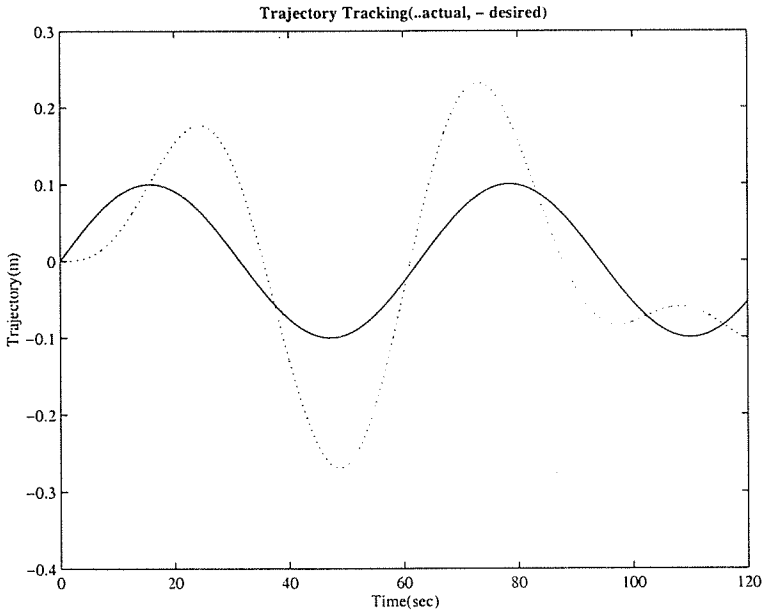

Figure 9.14: Explicit force-based OMCC: trajectory tracking

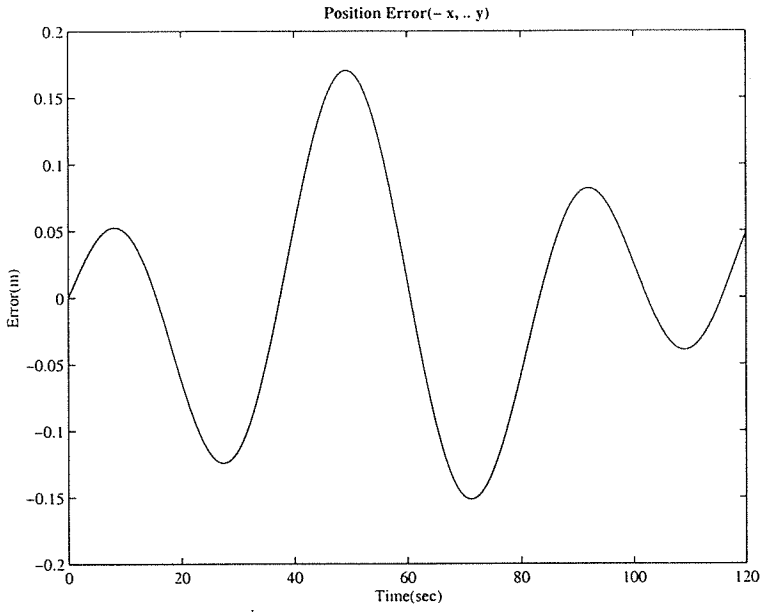

Figure 9.15: Explicit force-based OMCC: position error

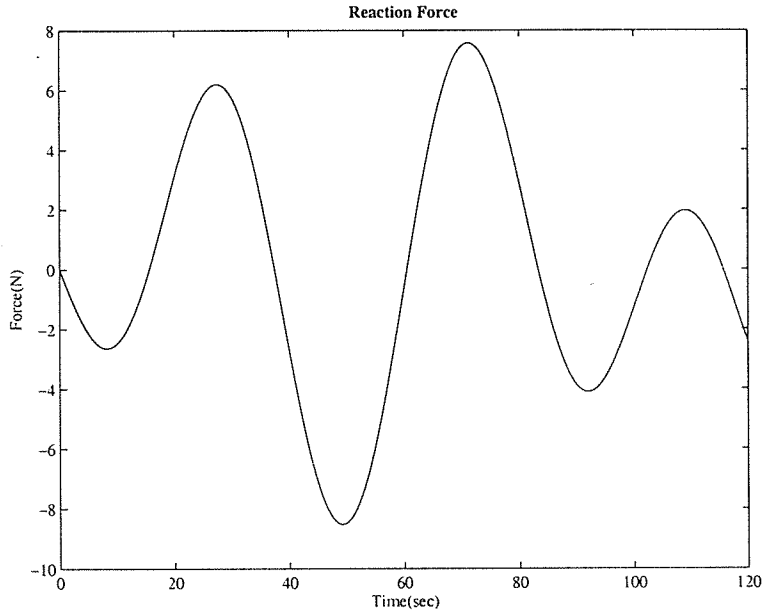

Figure 9.16: Explicit force-based OMCC: reaction force

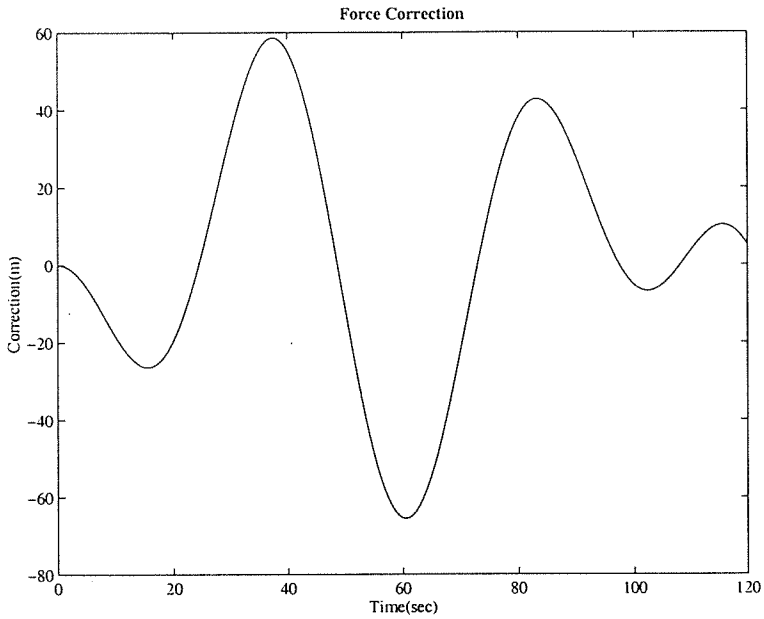

Figure 9.17: Explicit force-based OMCC: force correction

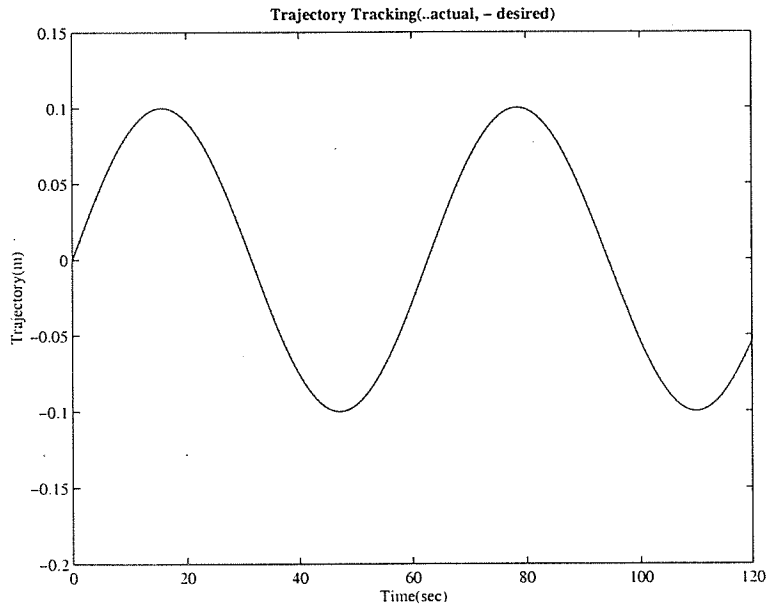

Figure 9.18: Robust explicit force-based OMCC: trajectory tracking

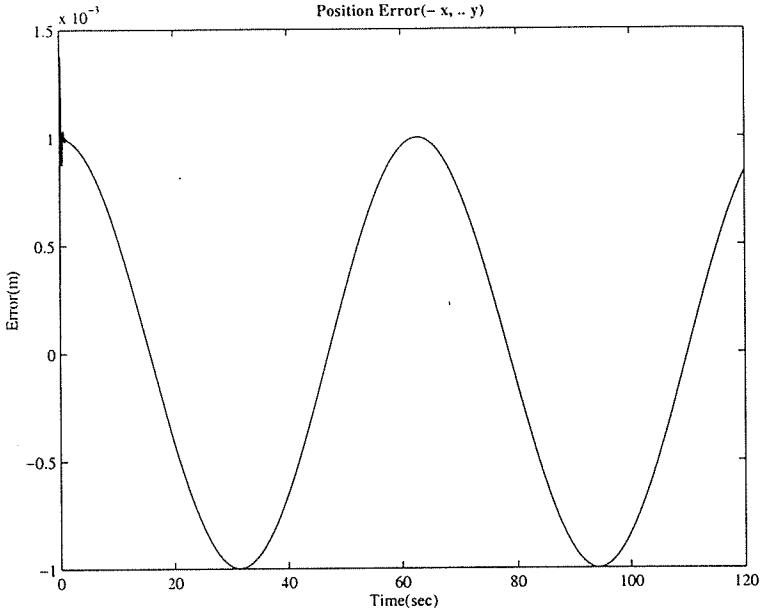

Figure 9.19: Robust explicit force-based OMCC: position error

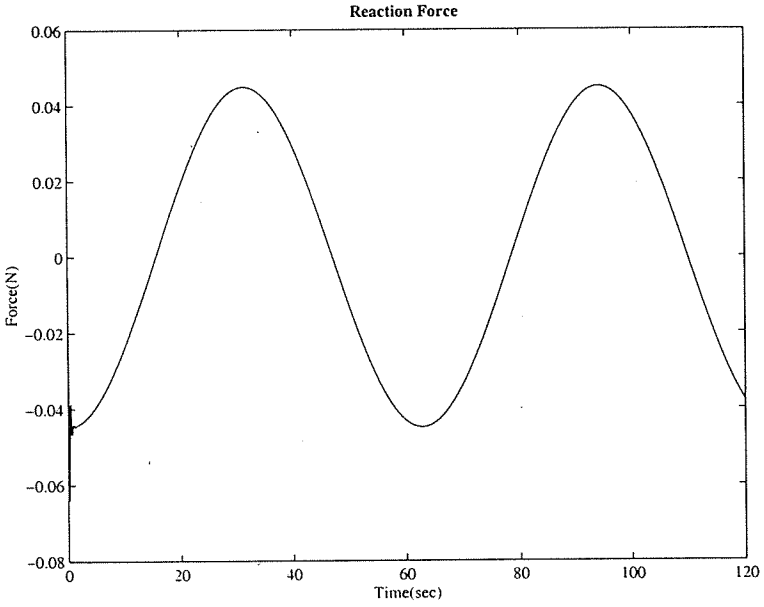

Figure 9.20: Robust explicit force-based OMCC: reaction force

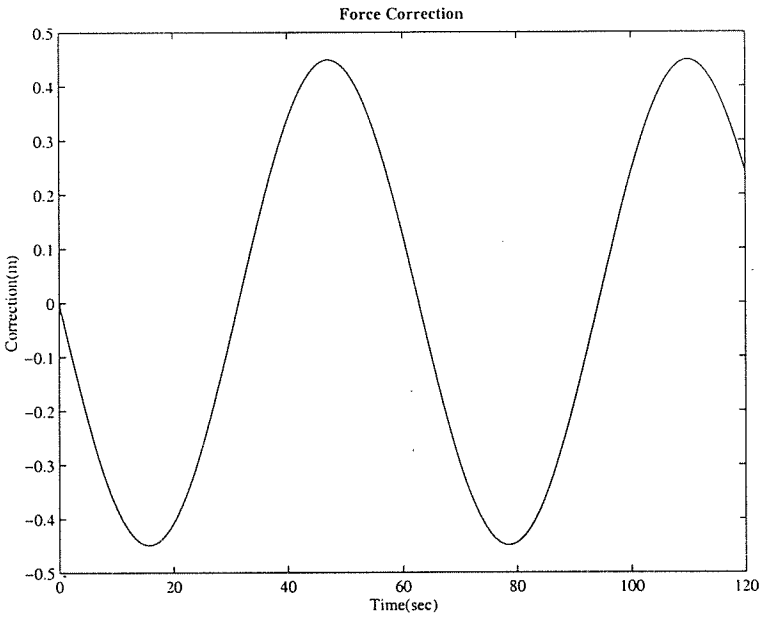

Figure 9.21: Robust explicit force-based OMCC: force correction

Chapter 10

Conclusion

The Autonomous Redundant Mobile Manipulator with Advanced Control Scheme (ARMMACS) has been developed at the Advanced Highway Maintenance and Construction Technology (AHMCT) Research Center at the University of California-Davis. ARMMACS is a differentially steered wheeled mobile manipulator, a type of robot studied by researchers worldwide due to limitless potential applications. The specifications, conception, and detailed design of ARMMACS comprise the first section, Chapters 1 through 6, of this report. The second section, Chapters 7 through 9, start with kinematic and dynamic modeling and analysis of ARMMACS and concludes with two control schemes. Eventually, AHMCT intends to deploy a Mobile Manipulator to perform various assistive and automated highway maintenance and construction tasks. ARMMACS is an initial step towards this deployment, serving as a test bed for the advanced control algorithms required to perform these tasks. At least two different mechanical configurations will also be tested on ARMMACS to verify the results of analytical manipulability studies presented in Chapter 7 and to validate the results of the dynamic modeling introduced in Chapter 9. A new robust coordination control for a human\manipulator system was developed based on the integral control utilizing H_∞ optimal control theory and demonstrated excellent control performance in computer simulation.

This document has concisely reviewed some of the important aspects of the ARMMACS system development. The interested reader is referred to the noted technical reports on documents for additional detail.

REFERENCES

Alexander, J.C. and J.H. Maddocks, On the Kinematics of Wheeled Mobile Robots. The International Journal of Robotics Research, 1989. 8(6.5): p. 15-27.

Arkin, R.C., Cervantes – Perez F., & Weitzenfeld A., (1997). Ecological robotics: a schema-theoretic approach. Intelligent Robots: Sensing, Modeling and Planning, eds. R.C. Bolles, H. Bunke and H. Noltemeier, 377-393. World Scientific.

Asakura, T., Minami, M., Yasufumi, N., Hatano, N., Horita, N. (1998). Position/orientation measurement of mobile manipulator on irregular terrain with solid mark-proposal of solving method by recursive computation and evaluations. Memoirs of the Faculty of Engineering, Fukui University. 46: 95-106.

Beer, F., & Jr. Johnston, E., ed. (1979). Mechanics of Materials. 2d ed. N.Y.: McGraw-Hill, Inc.

Borenstein, J. and Y. Koren, Motion Control Analysis of a Mobile Robot. Journal of Dynamic Systems, Measurement and Control, 1987. 109(6.2): p. 73-79.

Boyden, D., & Velinsky, S.A., (1993). Dynamic Modeling of Wheeled Mobil Robots. University of California, AHMCT Research Report UCD-ARR-93-10-05-01.

Boyden, F. D., Velinsky, S. A., Dynamic Modeling of Wheeled Mobile Robots for High Load Applications, Proc. of IEEE Int. Conf. on Robotics and Automation, 1994, pp. 3071-3078.

Chung, J. H., Velinsky, S. A., Hess, R. A., Interaction Control of a Redundant Mobile Manipulator, Int. Journal of Robotics Research, Vol. 17, No. 12, 1998, pp. 1302-1309.

Chung, J., & Velinsky, S.A., (1996). Modeling and Control of Mobil Manipulators. University of California, Doctoral Dissertation.

Craig, J.J., Introduction to Robotics: Mechanics and Control. 2nd ed. 1989, New York: Addison Wesley. 450.

Doty, K.L., et al., Robot Manipulability. IEEE Transactions on Robotics and Automation, 1995. 11(6.2): p. 462-468.

Dugoff, H., Fancher, P., Segal, L., An Analysis of Tire Traction Properties and Their Influence on Vehicle Dynamic Performance, SAE Transactions, 1970, pp. 1219-1243.

Dolan, J. M., Friedman, M. B. and Nagurka, M. L., "Dynamic and loaded impedance components in the maintenance of human arm posture," IEEE Transactions on Systems, Man, and Cybernetics, 1993, Vol. 23, No. 3, pp. 698-709.

Egeland, O. and J.R. Sagli, Coordination of motion in a spacecraft/manipulator systems. International Journal of Robotics Research, 1993. 12(6.4): p. 366-379.

Fukuda, T. and Fujisawa, Y., "A new manipulator in construction based on man-robot cooperation work," Proc. 8th Int. Symp. on Automation and Robotics in Construction, 1991, pp.239-245.

Fukuda, T., Fujisawa, Y. and Arai, F., "Man-robot cooperation work type of manipulator," Proc. 8th Ann. Conf. Of Robotics Society of Japan, 1990, pp. 655-656.

Ghamsepoor, A., Sepehri, N., A Measure of Machine Stability for Moving Base Manipulators, Proc. of IEEE Int. Conf. on Robotics and Automation, 1995, pp. 2249-2254.

Gardner, J.F. & Velinsky, S.A., (1999). Kinematics of mobile manipulators and implications for design. *Submitted to Journal.*

Hanebeck, U.D., Fischer, C., & Schimdt, G., (Sept.1997). ROMAN: A mobile robotic assistant for indoor service applications. IEEE/RSJ International Conference on Intelligent Robot and Systems. Innovative Robotics for Real-World Applications, 2: 518-25.

Hatano, M., Minami, M., Asakura, T., Takahashi, Y., & Ichimura, M., (1996). Adaptive control of mobile manipulators for traveling operations. Japan-USA Symposium on Flexible Automation, 1: 561-568.

Hirzinger, G. and Landzettel, K., "Sensory feedback structures for robots with supervised learning," Proc. IEEE ICRA, 1985, pp. 627-635.

Holenstein, A.A. & Badreddin, E., (1994). Mobile-robot position update using ultrasonic range measurements. International Journal of Robotics and Automation, 9(2): 72-

Hong, D., Velinsky, S. A., Feng, X., Verification of a Wheeled Mobile Robot Dynamic Model and Control Ramifications, ASME Journal of Dynamic Systems, Measurements, and Control, Vol. 121, No. 1, 1999, to appear.

Honda Motor Co. LTP. (1998). *Humanoid Robot.* **http://www.honda.co.jp/home/hpr/e_news/robot/concept1.htm** (28 Feb. 1999).

Hootsmanns, N. A. M., Dubowsky, S., The Motion Control of Manipulators on Mobile Vehicles, Proc. of IEEE Int. Conf. on Robotics and Automation, 1991, pp. 2336-2341.

Inman, D.J., (1996). Engineering Vibration. N.J.,: Prentice Hall.

Jagannathan, S., S.Q. Zhu, and F.L. Lewis, Path planning and control of a mobile base with nonholonomic constraints. Robtica, 1994. 12: p. 529-539.

Joshi, J., Desrochers, A. A., Modeling and Control of a Mobile Robot Subject to Disturbances, Proc. of IEEE Int. Conf. on Robotics and Automation, 1986, pp. 1508-1513.

Kazerooni, H., "Human robot interaction via the transfer of power and information signals," IEEE Transactions on System Cybernetics, Vol. 20, No 2, 1990.

Khatib, O. and Burdick, J., "Motion and force control of robot manipulators," Proc. ICRA, 1986, pp.1381-1386.

Khatib, O., Yokoi, K., Chang, K., Ruspini, D., Holmberg, R., Casal, A., & Baader, A., (1995). Force strategies for cooperative tasks in multiple mobile manipulation systems. Int. Symp. of Robotics Research, Munich.

Kockekali, H. and B. Ravani. A Feature Based Path Planning System for Robotic Stenciling of Roadway Markings. in ASCE Conference on Robotics for Challenging Environments. 1994.

Lawrence, D., "Impedance control stability properties in common implementations," IEEE ICRA, 1988, pp. 1185-1190.

Lim, D. & Seraji, H., (Oct. 1996). Configuration control of a mobile dexterous robot: real-time implementation and experimentation. International Journal of Robotics Research USA, 16 (5): 601-18.

Liu, K., Lewis, F. L., Decentralized Continuous Robust Controller for Mobile Robots, Proc. of IEEE Int. Conf. on Robotics and Automation, 1990, pp. 1822-1827.

Luh, J. and Zheng, Y. F., "Constrained relation between two coordinated industrial robots for motion control," International Journal of Robotics Research, Vol. 6, No. 3, pp. 60-70.

Matone, I cant remember the title right now, in Mechanical Engineering. 1998, Stanford: Palo Atlo.

McKerrow, P.J., Robotics. 1991, New York: Addison Wesley. 811.

Mueller, K.J., D. Hong, and S.A. Velinsky. A Wheeled Mobile Robot for Automated Crack Sealing. in ASCE Conference on Robotics for Challenging Environments. 1996.

Murry, R.M., Z. Li, and S.S. Sastry, A Mathematical Introduction to Robotic Manipulation. 1994: CRC Press.

Nagatani, K. and S. Yuta. Designing Strategy and Implementation of Mobile Manipulator Control System for Opening Door. in IEEE International Conference on Robotics and Automation. 1996. Minneapolis, MN.

Nagatani, K. and S. Yuta, Door-Opening Behavior of an Autonomous Mobile Manipulator by Sequence of Action Primitives. Journal of Robotic Systems, 1996. 13(6.11): p. 709-721.

Nassal, U.M., Motion Coordination and Reactive Control of Autonomous Multi-Manipulator Systems. Journal of Robotic Systems, 1996. 13(6.11): p. 737-754.

Oakley, M. (1998). Coupling High Performance Servo to Mechanical Loads. **www.ormec.com** (28 Feb. 1999).

Pin, F.G., et al., Motion Planning for Mobile Manipulators with a Non-Holonomic Constraint Using the FSP (Full Space Parameterization) Method. Journal of Robotic Systems, 1996. 13(6.11): p. 723-736.

Pin, F.G., Morgansen, K.A., Tulloch, F.A., Hacker, C.J. & Gower, K.B., (Nov. 1996). Motion planning for mobile manipulators with a non-holonomic constraint using the FSP (Full Space Parameterization) method. Journal of Robotic Systems USA, 13(11): 723-36.

Qiang Huang, Sugano, S., & Tanie, K., (1998). Motion planning for a mobile manipulator considering stability and task constraints. IEEE International Conference on Robotics and Automation, 3: 2192-8.

Raibert, M. H. and Craig, J. J., "Hybrid position/force control of manipulators," ASME Journal of Dynamic systems, Measurement, and Control, 1981, Vol. 103, No. 2, pp. 126-133.

Redzone Robics, Inc. (1998). Nuclear Product. **http://www.redzone.come/houdini.html** (28 Feb. 1999).

Redzone Robotics, Inc.(1998). Nuclear Product. **http://www.redzone.com/rosie.htm** (28 Feb. 1999).

Seraji, H., Reachability analysis for base placement n mobile manipulators. Jornal of Robotic Systems, 1995. 12(6.1): p. 29-43.

Seraji, H. An On-Line Approach to Coordiated Mobility and Manipulation. in IEEE International Conference on Robotics and Automation. 1993.

Shigley, J., & Mischke, C., ed. (1989). Mechanical Engineering Design. 5th ed. N.Y: McGraw – Hill, Inc.

Simon, D., K. Kapellos, and B. Espiau. Design and Control Procedures for a Free-Floating Udnerwater Manipulaation System. in IEEE International Conference on Robotics and Automation. 1997. Albuquerque, NM.

SKF General Catalog 4000 US, 2nd ed.(1997).

Sojourner ™, Mars Rover ™ and spacecraft design and images copyright © 1996-97, California Institute of Technology. All rights reserved. Further reproduction prohibited.

Sugar, T. & Kumar, V., (May 1998). Decentralized control of cooperating mobile manipulators. IEEE International Conference on Robotics and Automation, 4: 2916-21.

Tarn, T.J. and S.P. Yang. Modeling and Control for Underwater Robotic Manipulators - An Example. in IEEE International Conference on Robotics and Automation. 1997. Albuquerque, NM.

Velinsky, S.A., Heavy Vehicle System for Aytomated Pavement Crack Sealing. Heavy Vehicle Systems- Special Issue of the International Journal of Vehicle Design, 1993. 1(6.1): p. 114-128.

Volpe, R. and Khosla, P., "An experimental evaluation and comparison of explicit force control strategies for robotic manipulators," Proc. 1992 American Control Conference, pp. 758-764.

Volpe, R. [maint] (1998). *Ground Emergency Response Vehicle.* **http://telerobotics.jpl.nasa.gov/tasks/hazbot** (28 Feb. 1999).

Volpe, R. [maint] (1998). *Multifunction Automated Crawling Systems.* **http://telerobics.jpl.nasa.gov/tasks/macs/homepage.htr**.(28 Feb. 1999)

Weins, G. J., Effect of Dynamic Coupling in Mobile Robotic Systems, Proc. of SME Robotic Research World Conference, 1989, pp. 43-57.

West, T.H., S.A. Velinsky, and B. Ravani, Advanced Highway Maintenance and Construction Technolgy Applications - The Future Generation of Highway Machinery. TR News, Transportation Research Board, 1995. 176: p. 17-23.

Winters, S.E. (1992). Development of a Tethered Mobil Robot. University of California, Masters Thesis.

Xi, N. and Tarn, T. J., "Heterogeneous function-based human/robot cooperations," IEEE ICRA, 1998, pp. 1296-1301.

Xi, N., Tarn, T. J., and Bejczy, A. K., "Event-based planning and control for multi-robot control," Proc. IEEE ICRA, 1993, pp. I-2561-I-258.

Yamamoto, Y. and X. Yun, Coordinating locomotion and manipulation of a mobile manipulator, in Recent Trends in Mobile Manipulators, Y.F. Zheng, Editor. 1993, World Scientific: New Jersey. p. 157-182.

Yamamoto, Y. and X. Yun, Coordinating Locomotion and Manipulation of a Mobile Manipulator. IEEE Transactions on Automatic Control, 1994. 39(6.6): p. 1326-1332.

Yamamoto, Y. and Y. Xiaopong. (Oct. 1996). Effect of the Dynamic Interaction on Coordinated Control of Mobile Manipulators. *IEEE Transcations on Robotics and Automation USA*, 12(5): 816-24.

Yamamoto, Y., H. Eda and Yun Xiaoping. (April 1996). Coordinated Task Execution of a Human and a Mobile Manipulator. *IEEE International Conference on Robotics and Automation*, 2: 1006-11.York: McGraw-Hill, Inc.

Yoshikawa, T., Manipulability of Robotic Mechanisms. International Journal of Robotics Research, 1985. 4(6.2): p. 3-9.

Yoshikawa, T., Dynamic Manipulability of Robot Moanipulators. Journal of Robotic Systems, 1985. 2(6.1): p. 113-124.

Zheng, Y. F. and Luh, J., "Control of two coordinated robots in motion," Proc. IEEE 24th CDC, 1985, pp. 1761-1765.

Appendix A – Calculations

Preface to Appendix A

Dimensions:

Effective Tire Radius, $r := 12.7 \cdot cm$ (5.00 in)

Material Properties

Material	Yield Strength, S_y MPa (ksi)	Modulus of Elasticity, E GPa (Mpsi)
6061-T651	275.8 (40)	71.0 (10.3)
6063-T52	172.4 (25)	71.0 (10.3)
Socket Head Cap Screws	1241 (180)	207.0 (30.0)
AISI 1144 Stressproof	689.5 (100) 912.2 (132) mean	207.0 (30.0)
A500B	317.2 (46)	207.0 (30.0)

Load Cases Used for Design

Maximum Static Load State

Condition	Value
Maximum Drive Tire Tractive Force (longitudinal), F_t	547 N (123 lb)
Maximum Transmitted Torque (Limited by Tractive Force)	69.3 N-m (613 lb-in)
Maximum Platform Weight	2224 N (500 lb)
Weight Distribution	70 % Front, 30 % Rear uniformly to each wheel
Maximum Lateral Acceleration, a_l	One g
Angular Velocity of Wheel, n_s	200 RPM

Fatigue Load State

Condition	Value
Maximum Transmitted Torque (Limited by Tractive Force), F_t	2.3 N-m (20 lb-in) to 60 N-m (631 lb-in)
Maximum Platform Weight	2224 N (500 lb)
Weight Distribution	70 % Front, 30 % Rear uniformly to each wheel
Maximum Lateral Force, F_{af}	125 N (28.1 lb)
Angular Velocity of Wheel, n_f	4.8 rad/s (46 RPM)

Appendix A – Calculations

Preliminary Weight Estimate

Given: Approximate weights of available components, the tubular chassis concept presented in Chapter 3 made of aluminum, and approximate frame dimensions of 48 in long X 27 in wide

Find: An estimate of the ARMMACS weight and weight distribution

Solution: Shown in spreadsheets below

Platform Weight Estimate						
Platform Component	**Qty**	**Length** (cm)	**Width** (cm)	**Volume** (cm^3)	**Unit Weight**** (N)	**Item Weight** (N)
Main Rail*	2	121.9		1332.0	36.5	73.0
Cross-members*	3	68.6		749.3	20.5	61.6
Support/Align plate	1	20.3	86.4	2228.6	61.1	61.1
Electric box	2	45.7	61.0	886.9	24.3	48.6
Caster support	6	15.2	12.7	245.8	6.7	40.4
Couping housing	2				28.9	57.8
Joint plates	8	10.8	12.7	174.2	4.8	38.2
				Total Weight (N) = 380.6		

** AL Density (N/cm^3) = 0.027

* Main Rails and Cross-members made of 5.1 X 12.7 X .318 cm (2 X 5 X .125 in) 6063-T52 Al

ARMMACS Weight Estimate						
Item	**Qty**	**Unit Weight** (N)	**Item Weight** (N)	**Approx. Location**	**Xcg From Front** (cm)	**Xcg From Front Axle** (cm)
Robot	1	222.4	222.4	F	7.6	0.0
Robot Power	1	66.7	66.7	R	68.6	61.0
Motor	2	137.9	275.8	F	31.8	24.1
Gear Head	2	89.0	177.9	F	8.9	1.3
Computer	1	89.0	89.0	M	61.0	53.3
Motor Drive	2	44.5	89.0	R	101.6	94.0
Electrical Components	1	111.2	111.2	M	86.4	78.7
Platform	1	380.6	380.6	M	55.9	48.3
Cabling	1	89.0	89.0	M	61.0	53.3
Encoder Assy.	1	44.5	44.5	F	7.6	0.0

Total ARMMACS Weight (N) = 1546
Weight w/o Manipulator (N) = 1324

Appendix A – Calculations

Estimating Weight Distribution:

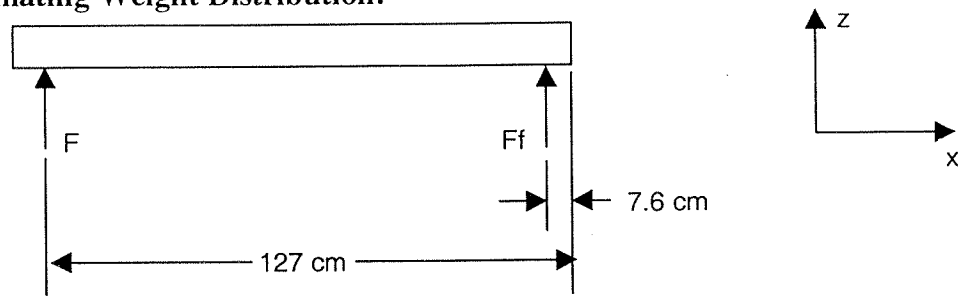

Sum moments about the front wheel axis (Ff application point):	
Item Creating Moment	Moment (N-cm)
Robot	0.0
Robot Power	4067.3
Motor	6654.6
Gear Head	226.0
Computer	4745.1
Motor Drive	8360.5
Electrical Components	8755.9
Platform	18369.7
Cabling	4745.1
Encoder Assy.	0.0
Fr	-119.4Fr

Fr (N) = 468.4

Sum Forces in z Direction

Ff (N) = 1078

Approx. weight distrbution:

Front (Drive Wheels): 70 %

Rear (Casters): 30 %

Appendix A – Calculations

Tire Diameter Calculation

Given:

$v_p := 2.29 \cdot \frac{m}{s}$ $\quad J_m := 0.0021 \cdot kg \cdot m^2$ $\quad m_l := 226.7 \cdot kg$

$\omega_m := 133.3 \cdot \pi \cdot \frac{rad}{s}$ $\quad J_g := 5 \cdot 10^{-5} \cdot kg \cdot m^2$ $\quad t_a := 0.5 \cdot sec$

$N_r := 20$ $\quad J_w := 0.077 \cdot kg \cdot m^2$ $\quad T_m := 6.9 \cdot N \cdot m$

where:

v_p = Desired maximum linear velocity of platform

ω_m = Maximum continuous motor speed

N_r = Gearhead Reduction Ratio

J_m = Mass moment of inertia of F4050 servomotor

J_g = Mass moment of inertia of RA115 gearhead

J_w = Estimated Press-on tire and wheel assy. inertia (modeled as a rubber cylinder, a steel cylinder, and a steel disk)

m_l = max. mass of platform

t_a = Desired minimum acceleration time to max. velocity

T_m = F4050 servomotor continuous stall torque

Find: The minimum and maximum tire diameters that will provide the desired kinematic and dynamic perfomance

Assumptions:

- Minimum tire diameter constrained soley by desired kinematics
- Maximum tire diameter constrained by desired dynamics
- Error and variation in estimated tire and wheel inertia is negligible compared to the platform inertia
- Constant acceleration
- Gearhead inertia is specified as seen by input pinion
- Neglect friction and inertia of custom drive train components

Solution:

Minimum effective tire diameter

$\omega_s := \frac{\omega_m}{N_r}$ $\quad r_{min} := \frac{v_p}{\omega_s}$

$d_{min} := 2 \cdot r_{min}$

$d_{min} = 0.219 \cdot m$

Appendix A – Calculations

Maximum effective tire diameter

FBD 1

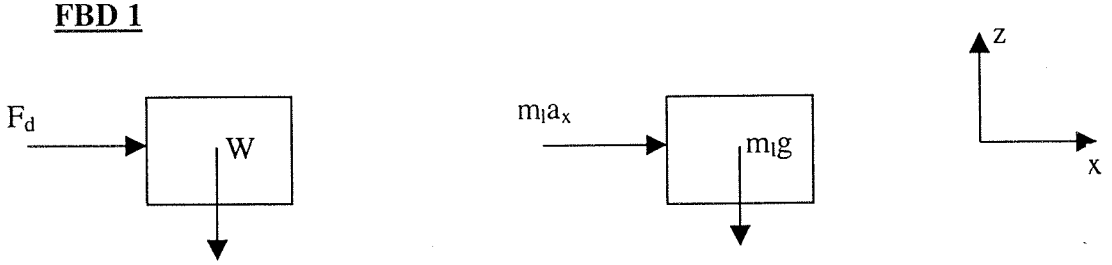

FBD 2

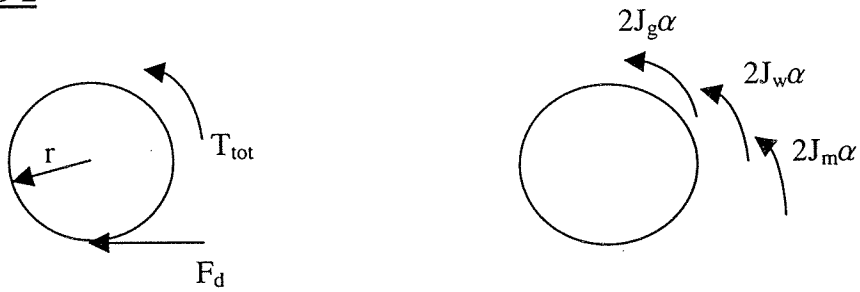

$$\sum_{\text{forces}} F_x = m_l \cdot a_x$$

$$a_x := \frac{v_p}{t_a} \qquad F_d := m_l \cdot a_x$$

$$\sum_{\text{torques}} T = J \frac{d^2}{d\theta^2} \theta$$

$$T_{tot} := 2 \cdot T_m \cdot N_r \qquad a_x = r_{max} \cdot \alpha$$

$$T_{tot} - F_d \cdot r_{max} = \left(2 \cdot J_{meq} + 2 \cdot J_w + 2 \cdot J_g\right) \cdot \alpha$$

$$T_{tot} = \left(2 \cdot J_{meq} + 2 \cdot J_w + 2 \cdot J_g + 2 \cdot J_{leq}\right) \cdot \alpha$$

$$J_{leq} = m_l \cdot r_{max}^2$$

$$T_{tot} = \left(2 \cdot J_{meq} + 2 \cdot J_w + 2 \cdot J_g + m_l \cdot r_{max}^2\right) \cdot \frac{a_x}{r_{max}}$$

$J_{meq} := J_m \cdot N_r^2$

$$r_{max} := \frac{-1}{\left[2 \cdot \left(a_x \cdot m_l\right)\right]} \cdot \left(-T_{tot} - \sqrt{T_{tot}^2 - 8 \cdot a_x^2 \cdot m_l \cdot J_{meq} - 8 \cdot a_x^2 \cdot m_l \cdot J_w - 8 \cdot a_x^2 \cdot m_l \cdot J_g}\right)$$

$r_{max} = 0.231 \cdot m$

$d_{max} := 2 \cdot r_{max}$ $\quad d_{max} = 0.462 \cdot m$

Using these bounds the selected tire diameter, d is:

$d := 0.254\ m$

Maximum Transmittable Drive Torque

Given:

- Maximum Static Load State in Appendix Preface

$W := 2224 \cdot N$ $\quad N_r = 20$

$d = 0.254 \cdot m$ $\quad T_{mmax} := 13.6 \cdot N \cdot m$

$\mu_s := 0.7$ (Assumed)

Find:

a) Whether transmittable torque is limited by motors or tractive force
b) Maximum torque drive train will transmit

Solution:

Maximum torque at gearhead output

$T_{gmax} := T_{mmax} \cdot 20$ $\quad T_{gmax} = 272 \cdot N \cdot m$

Maximum torque as limited by tractive force

$F_t := 0.35 \cdot W \cdot \mu_s$ $\quad T_{tmax} := F_t \cdot \frac{d}{2}$

$T_{tmax} = 69.2 \cdot N \cdot m$

Therefore, $T_t := T_{tmax}$

$T_t = 69.2 \cdot N \cdot m$

Appendix A – Calculations

Coupling Housing Bolt and Thread Strength Analysis

Given:

- Maximum Static Load State in Appendix Preface
- 5/16 in -18 Socket Head Cap Screws attach axle to coupling housing and Coupling Housing to Frame
- Coupling Housing Material: 6061-T651 AL

Find:

a) Min. thread engagement length that ensures bolts yield before internal threads

b) Factor of Safety against yielding for bolts attaching Axle to Coupling Housing

Assumptions:

- Alignment Boss supports shear, bolts subject to axial force only
- x-direction reaction forces btwn axle & coupling housing act at bolts

Solution:

a) Min. thread engagement length

- Using theory for thread strength given in Machinery's Handbook, 24 Ed.

For 5/16 in -18 Socket Head Cap Screws:

$E_{smin} := 0.6888 \cdot cm$ $\quad D_{smin} := 0.7686 \cdot cm$ $\quad S_e := 1241 \cdot 10^6 \cdot Pa$

$K_{nmax} := 0.6731 \cdot cm$ $\quad E_{nmax} := 0.7155 \cdot cm$ $\quad S_i := 275.8 \cdot 10^6 \cdot Pa$

$A_t := 0.3381 \cdot cm^2$ $\quad n := 7.09 \cdot \frac{1}{cm}$

$$L_e := \frac{2 \cdot A_t}{\pi \cdot K_{nmax} \cdot \left[\frac{1}{2} + 0.57735 \cdot n \cdot \left(E_{smin} - K_{nmax}\right)\right]} \qquad L_e = 5.667 \cdot 10^{-3} \cdot m$$

$$A_s := \pi \cdot n \cdot L_e \cdot K_{nmax} \cdot \left[\frac{1}{2 \cdot n} + 0.57735 \left(E_{smin} - K_{nmax}\right)\right]$$

$$A_n := \pi \cdot n \cdot L_e \cdot D_{smin} \cdot \left[\frac{1}{2 \cdot n} + 0.57735 \left(D_{smin} - E_{nmax}\right)\right]$$

Appendix A – Calculations

a) (cont'd)

$$J := \frac{A_s \cdot S_e}{A_n \cdot S_i} \qquad J = 3.1$$

For J > 1,

$$Q := J \cdot L_e$$

$$Q = 0.018\ m$$

where:

E_{smin} = min. pitch diameter of external thread
K_{nmax} = max. minor diameter of internal thread
A_t = tensile stress area of screw thread
D_{smin} = min. major diameter of external thread
E_{nmax} = max. pitch diameter of internal thread
n = number of threads per cm
S_e = tensile strength of external thread material
S_i = tensile strength of internal thread material
Q = required length of engagement

b) Factor of Safety of Axle to Coupling Housing bolts

FBD A

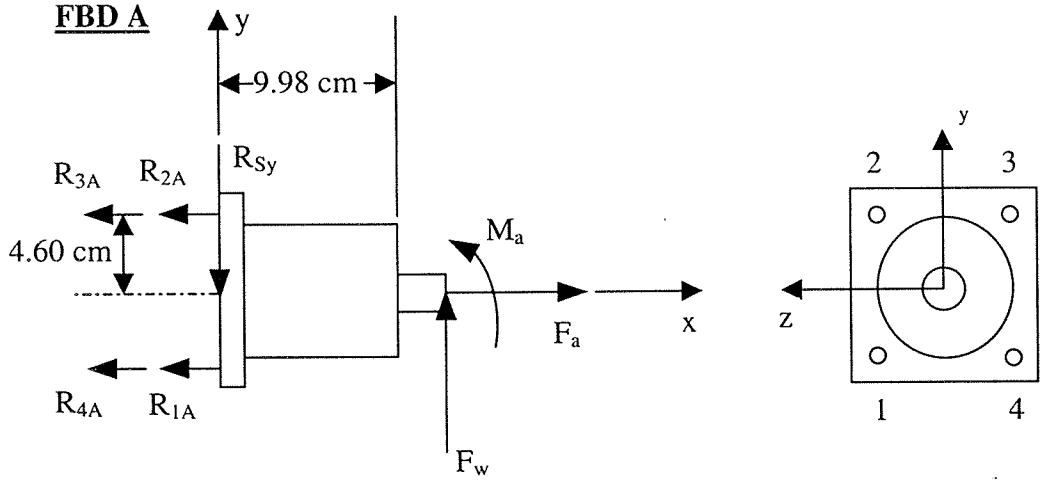

FBD B

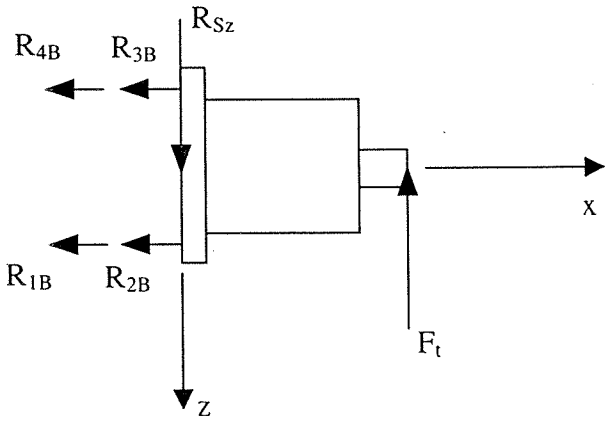

b) (cont'd)

From FBD A

$$\sum_{\text{forces}} F_x = 0 \qquad -R_{1A} - R_{4A} - R_{2A} - R_{3A} + F_a = 0$$

$$\sum_{\text{moments}} M_1 = 0 \qquad M_a - F_a \cdot (4.60 \cdot \text{cm}) + R_{2A} \cdot (9.19 \cdot \text{cm}) + R_{3A} \cdot (9.19 \cdot \text{cm}) + F_w \cdot (9.98 \cdot \text{cm}) = 0$$

Assume that $R_{1A} = R_{4A}$ and $R_{2A} = R_{3A}$

$$M_a - F_a \cdot (4.60 \cdot \text{cm}) + R_{2A} \cdot (18.38 \cdot \text{cm}) + F_w \cdot (9.98 \cdot \text{cm}) = 0$$

$F_a := 1112 \cdot N$ one g lateral acceleration, distributed equally to each wheel

$M_a := r \cdot F_a$

$F_w := 778.4 \cdot N$ 35 % of maximum weight

$$R_{2A} := \left[-.0544 \cdot \frac{\left(M_a - 4.6 \cdot F_a \cdot \text{cm} + 9.98 \cdot F_w \cdot \text{cm} \right)}{\text{cm}} \right] \qquad R_{2A} = -913 \cdot N$$

$R_{2A} = R_{3A} = -913 \cdot N$

$R_{1A} = R_{4A} = 1469 \cdot N$

From FBD B

$$\sum_{\text{forces}} F_x = 0 \qquad -R_{1B} - R_{2B} - R_{3B} - R_{4B} = 0$$

$$\sum_{\text{moments}} M_1 = 0 \qquad R_{3B} \cdot (9.19 \cdot \text{cm}) + R_{4B} \cdot (9.19 \cdot \text{cm}) + F_t \cdot (9.98 \cdot \text{cm}) = 0$$

Assume that $R_{1B} = R_{2B}$ and $R_{3B} = R_{4B}$

$R_{1B} = -R_{3B}$

$$R_{3B} := \frac{-F_t \cdot (9.98 \cdot \text{cm})}{18.38 \cdot \text{cm}} \qquad R_{3B} = -296 \cdot N$$

$R_{3B} = R_{4B} = -296 \cdot N$

$R_{1B} = R_{2B} = 296 \cdot N$

b) (cont'd)

$R_1 = R_{1A} + R_{1B}$, $R_2 = R_{2A} + R_{2B}$, etc.

$R_1 := 1765 \cdot N$ $R_2 := -617 \cdot N$ $R_3 := -1209 \cdot N$ $R_4 := 1173 \cdot N$

Now the Factor of Safety

$F_i := 26746 \cdot N$ Bolt preload (Shigley, 1989 eqn. 8-25)

$F_{tot} := F_i + R_1$ $\sigma := \frac{F_{tot}}{A_t}$ $\sigma = 8.433 \cdot 10^8$ •Pa

$S_y := 1241 \cdot 10^6 \cdot Pa$ $N_{bolta} := \frac{S_y}{\sigma}$ $N_{bolta} = 1.5$

Appendix A – Calculations

Pneumatic Tire Flange Stress Analysis

Given:

- Dimensions shown in figure
- Material: 6061-T651 AL, $S := 275.8 \cdot 10^6 \cdot Pa$
- Equations for hub diameter provided by Trantorque(R)manufacturer Fenner Drives (TM)

$$D_h = \left[\frac{H_p \cdot D}{S - \frac{H_p}{2}} + D \right]$$

For hubs width less than the full length of the trantorque interference section:

$$H_{pa} = H_p \cdot \left(\frac{l}{l_t} \right)$$

where:

D_h = Minimum outside hub diameter

D = Bore diameter, $D := 3.81 \cdot cm$

S = Yield strength of hub material

H_p = Hub pressure at specified nut torque for full length hub, $H_p := 75.8 \cdot 10^6 \cdot Pa$

H_{pa} = Hub pressure at specified nut torque for partial length hub

l = Actual length of hub

l_t = Full length of Trantorque interference region, $l_t := 1.91 \cdot cm$

Find: Factor of Safety against yield for flange

Assumptions:

- Stress due to torque transmission are negligle compared to those from radial hub pressure
- Neglect wheel stud holes
- Small and large diameter sections are separate

Appendix A – Calculations

Figure:

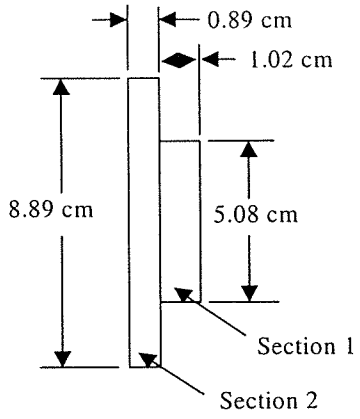

Solution:

Assume sections 1 and 2 are separate and solve for Factor of Safety in each

Section 1

$D_{h1} := 5.08 \cdot cm$ $\quad l_1 := 1.02 \cdot cm$

$H_{pall1} := \frac{2 \cdot S \cdot (D_{h1} - D)}{D_{h1} + D}$ $\quad H_{pall1} = 7.88 \cdot 10^7$ Pa

$H_{pa1} := H_p \cdot \left(\frac{l_1}{l_t}\right)$ $\quad H_{pa1} = 4.048 \cdot 10^7$ Pa

$N_{flange1} := \frac{H_{pall1}}{H_{pa1}}$ $\quad N_{flange1} = 1.9$

Section 2

$D_{h2} := 8.89 \cdot cm$ $\quad l_2 := 0.89 \cdot cm$

$H_{pall2} := \frac{2 \cdot S \cdot (D_{h2} - D)}{D_{h2} + D}$ $\quad H_{pall2} = 2.206 \cdot 10^8$ Pa

$H_{pa2} := H_p \cdot \left(\frac{l_2}{l_t}\right)$ $\quad H_{pa1} = 4.048 \cdot 10^7$ Pa

$N_{flange2} := \frac{H_{pall2}}{H_{pa2}}$ $\quad N_{flange2} = 6.2$

Section 1 is actually bounded where it connects to section 2, which will result in smaller deflections and less stress than predicted within section 1. Therefore the factor of safety is greater than 2